Tunable Filters and Interference Rejection System for Interferer Suppression at RF and Microwave Bands

Laya Mohammadi

Dissertation submitted to the faculty of the Virginia Polytechnic Institute and State University in partial fulfillment of the requirements for the degree of

Doctor of Philosophy

In

Electrical Engineering

Kwang J. Koh

Sanjay Raman

Dong S. Ha

Jeffrey H. Reed

Guo Q. Lu

August 9, 2016

Blacksburg, Virginia

Keywords: RF and microwave frequencies, band-pass filter, band-stop filter, interference rejection system

Tunable Filters and Interference Rejection System for Interferer Suppression at RF and Microwave Bands

Laya Mohammadi

ABSTRACT

Contemporary wireless systems have advanced toward smart and multifunctional radios such as software-defined or cognitive radios which access a wideband or multiband spectrum dynamically. It is desirable for the wireless systems to have high frequency selectivity early in the receiver chain at RF to relax the dynamic range requirements of subsequent stages. However, integration of high selectivity RF band-pass filters (BPF), or band-stop filters (BSF) is challenging because of limited quality factor (Q) of passive components in integrated circuit (IC) technology [1].

This proposed research achieves the followings:

1. Developing, and demonstrating innovative integrated band-pass filter that relaxes the performance tradeoffs in conventional LC filters to maximally increase filter reconfigurability in frequency tuning range (2-18 GHz), selectivity (Q=5~100) with superior dynamic range (DR>100 dB) at RF to microwave frequency range [2].

2. Implementing active notch filter system comprised of a Q-enhancement band-pass filter (BPF) and an all-pass amplifier. The notch response is synthesized by subtracting the BPF output from the all-pass output. In the proposed synthetic notch filters, the BPF is responsible for defining selectivity while stop-band attenuation is primarily dependent on the gain matching between the BPF and all-pass amplifier. Therefore, notch attenuation is controllable independently from the bandwidth tuning, providing more operational flexibility. Further, the filter dynamic range is optimized in the all-pass amplifier independently from the selectivity control in the BPF, resolving entrenched tradeoff between selectivity and dynamic range in active filters [3].

3. Demonstrating the mode reconfigurable LC filter that works in either BPF or BSF for a flexible blocker filtering adaptive to the dynamic blocker environments.

4. Implementing a novel feedback-based interference rejection system to improving the linearity of the BPF for high Q cases, in which the BPF Q is set to a specific value and further increase in Q is achieved using feedback gain. And finally, the second LC tank is added to increase the out of band rejection in band-pass characteristics.

Tunable Filters and Interference Rejection System for Interferer Suppression at RF and Microwave Bands

Laya Mohammadi

GENERAL AUDIENCE ABSTRACT

As many radios coexist and interference environment becomes more hostile and dynamic, it is critical to establish high frequency selectivity at the earliest possible stage in a receiver chain to avoid desensitization with a minimal power penalty. Historically, band-pass filters and band-stop filters have been used to avoid the receiver desensitization, however, the design of band-pass/band-stop filters are more challenging at radio frequencies (RF).

There are different type of RF filters including Q-enhanced LC filters and N-path filters. Q-enhanced LC filters have been widely investigated for filtering blockers, but only with limited system applications due to a narrow dynamic range (DR). While, recently N-path filters are gaining growing attention, a high selectivity comes at the cost of system complexity and power penalty thereof: due to the inherent array architecture driven by multiphase clocks, the dynamic power dissipation in the N-path filter will be proportional to the increase of the filter center frequency (fc), claiming > 100's mW when the fc is projected over 10GHz for instance. Therefore, designing on-chip RF filters are still challenging due to the strong tradeoff among selectivity, dynamic range, and power consumption.

The main goal of this research is to realize a high performance on-chip filter which is capable of mode switching between bandpass (BPF) and bandstop (BSF) for a flexible blocker filtering adaptive to the dynamic blocker environments.

To

My father

Ardeshir Mohammadi

My mother

Farideh Mohammadi

and my love

Samet Zihir

Acknowledgment

I would like to express my sincere appreciation to my advisor, Dr. Kwang-Jin Koh, for his great help during my PhD studies. I learned circuit design as well as being professional from him. Thank you very much for the opportunity you gave me to get my PhD and also training me for both future career and life.

I want to thank my committee members for their great comments and help, also my lab mates, Yahya Mortazavi, Sadia Afroz, Mohammad Reza Zargarzadeh, Dongseok Shin, Farooq Amin, Hyunchul Kim, Shinwoong Park, Keyvan Ramezanpour, and Hedieh Elyasi for all technical dissections and supports.

I am always so indebted to my parents Dr. Ardeshir Mohammadi and Farideh Mohammadi who have always provided support and encourage during my life. Without my father high expectation and my mother prayers I could not reach this point. I would also like to thank my brother Hossain and my sister Hanieh.

Last but not least, my husband and my love, Samet Zihir, thank you for being my love, best friend, colleague, and supporter.

Table of Contents

Table of Figures

Chapter 1 : Introduction

As many radios coexist and interference environment becomes more hostile and dynamic, it is critical to establish high frequency selectivity at the earliest possible stage in a receiver chain to avoid desensitization with a minimal power penalty [4]-[6]. Figure 1.1 shows the block diagram of the receiver in presence of the strong blocker. It should be mentioned that in wideband wireless receivers the off-chip band-pass filter (BPF) which comes after the antenna may not have enough attenuation for strong blockers (blocker power as high as 0 dBm) due to limited tunability. This strong unwanted signal may saturate or desensitize the receiver due to either the nonlinearity of subsequent blocks or intermodulation products.

1.1 Receiver interference problem

The possible approach to overcome the interference problem is to use either band pass filter (BPF) with high selectivity to keep the desired signal and reject the unwanted ones or band stop filter (BSF) to reject the blocker. In either approach the receiver front-end should have enough attenuation for strong in band or out of band blockers to prevent the receiver from being saturated and relax the following blocks.

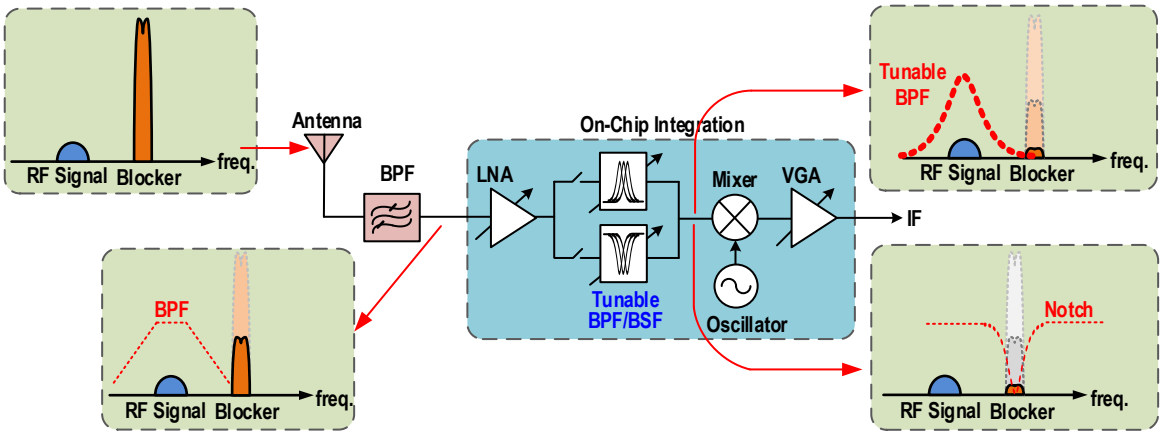

Figure 1.1: Block diagram of receiver in presence of strong blocker.

Although many researches have been done on different receiver blocks to improve the performance of RF blocks, the use of RF filters is still limited due to their poor performance [7]-[11]. The required on-chip band-pass or band-stop filters should meet the system requirements such as wideband frequency tuning, bandwidth tuning independent from frequency tuning, high input compression point and therefore high dynamic range. In addition, it is necessary to have variable gain and robustness to large interfere.

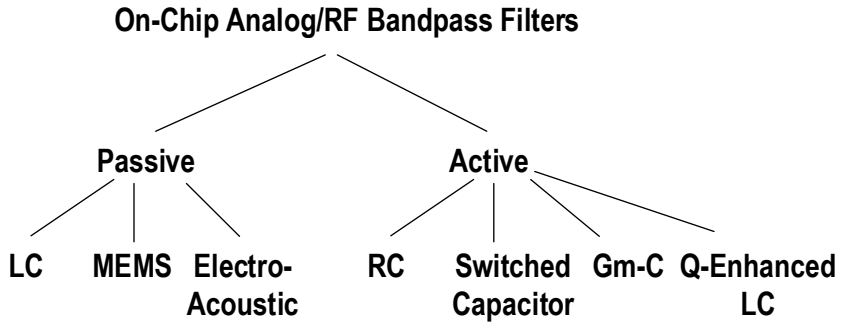

Figure 1.2: RF and analog band pass filters alternatives [12].

Figure 1.2 shows common structures for RF and analog filters. All passive filters in either microstrip or MEMS suffer from tradeoffs amongst selectivity, loss, and volume: the higher selectivity, the more passband losses, and the larger volume [12]. Therefore, passive filters are not a suitable option when high selectivity and variable gain is required. However, active filters are more feasible with RF requirements. The main active filter categories are as follows.

1.2 Active Filters

Usually the RF active filters suffer from trade-off between selectivity and dynamic range: the filter noise and linearity performances tend to be degraded when increasing the filter Q due to higher noise and nonlinearity by the transistors in the active filters. Active filters utilizing active-RC or Gm-C filters are low frequency approaches. Although, Gm-C filters can operate in higher frequencies than active-RC filters, still their operation frequencies are mostly MHz or low GHz range. Also, they have poor performance in terms of dynamic range [13]. The main problem with on chip LC filters is the limited quality factor of on chip inductor and capacitors. In order to achieve a high Q inductor, active inductor techniques have been widely used [13]-[15].

1.3 Q-Enhanced LC Filters

Historically, Q-enhanced LC filters have been widely investigated for filtering blockers, but only with limited system applications due to a narrow dynamic range (DR) [16]-[21]. The filter noise and linearity performances tend to degrade as filter Q increases due to transistors creating higher noise and nonlinearity . It is shown in [12] that the dynamic range (DR) of the gm-C filters depends on $1/Q^2$ while the DR of the Q-enhanced LC filters depends on Q_0/Q^2, where Q_0 is the quality factor of on-chip inductors. Therefore, in general Q-enhanced LC filters have higher dynamic range than gm-C filters. Also, Q-enhanced LC filters are better choices for high frequency applications since as frequency increases, their size decreases.

1.4 N-Path Filters

Recently, N-path filters are gaining growing attention and can achieve a high selectivity (Q>50) with relaxed compromise of dynamic range [22]-[27]. However, the high performance comes at the cost of system complexity and power penalty thereof: the N-path filters require #N mixer array and multi-phased LO driving circuitry dissipating dynamic power proportional to the increase of filter center frequency. For instance in [24], the power dissipation grows from 3.6 mW at 100 MHz to 43.2 mW at 1.2 GHz. The projected power dissipation at microwave range (e.g. >10 GHz) could be prohibitive for mobile terminals, let alone the difficulty in creating precision multi-phased LO signals at such high frequencies, likely limiting the application space below ~1's GHz range. Further, any mismatch in the N-path array will create LO spurs, hesitating its application to spur-sensitive defense systems. Also, it will be a challenging task to add the function of BPF-to-BSF mode reconfigurability in the N-path filters. Therefore, there is still a compelling research need to resolve the intrinsic problem of performance tradeoffs in active filters and thus to provide more power-efficient, hardware-economic, and robust filtering solution in addition to filter-mode reconfigurability adaptive to blockers environment.

Based on the brief review on active filters, Q-enhanced LC filters have higher DR than gm-C filters and lower power consumption than N-path filters at RF and microwave frequencies. Therefore, Q-enhanced LC filters are the best candidate for high frequency realization; however, as mentioned in section 1.3 the strong tradeoff between selectivity and dynamic range is the main issue for this type of filters. Chapter 2, will analyses Q-enhanced LC filter in more details and the proposed techniques which improve the DR of the BPF significantly will be discussed.

Chapter 2 : Q-Enhancement Tunable LC Band-Pass Filters

This chapter introduces a new Q-enhanced LC filter topology which adopts both current- and voltage-mode drivers for more operational flexibility in the linearity-noise tradeoff space. By applying a linear varactor control scheme in addition to a gain peaking technique enabled by a dynamic negative resistance cell, the proposed LC filter achieves one of the best dynamic range performances, compared with prior state of the art works.

2.1 Current-Driven BPF vs Voltage-Driven BPF

Figure 2.1 shows two types of LC-resonator based Q-enhanced BPF topologies. For both cases, a negative resistance ($-R_P$) is added to compensate a finite frequency-dependent LC-tank loss (R_P) so that the overall filter Q is not limited by the R_P but is controllable by R_c. Each filter topology has its unique opportunity in the RF design space. The current-driven BPF in Figure 2.1(a) can achieve larger signal gain with lower noise figure (NF) than the voltage-mode BPF at the cost of linearity degradation that will be particularly severe when the filter Q or R_c increases. Whereas, in the voltage-driven BPF in Figure 2.1(b) maximum signal gain is limited to unity regardless of the filter Q as long as the $-R_p$ compensates the tank loss completely. Therefore, with little or no suffering from the gain-dependent nonlinearity, linearity performance of the voltage-driven BPF will be less sensitive to the increase of Q. However, output noise power by the LC tank and the active negative resistance will be proportional to the increase of R_c, resulting in a suboptimal NF performance compared with the

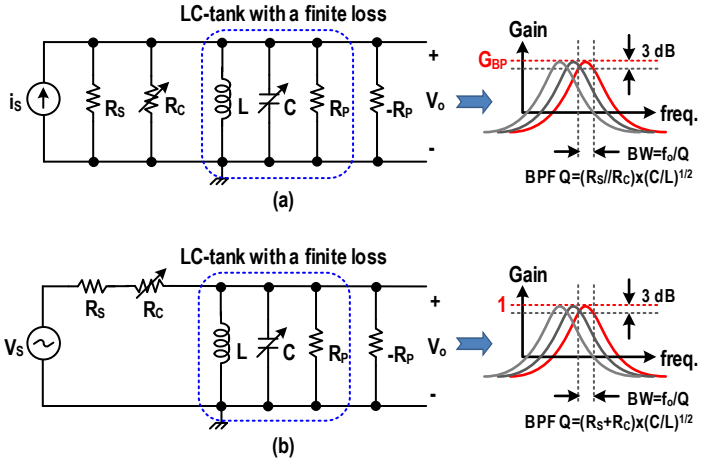

Figure 2.1: LC-resonator based 2nd-order bandpass filter (BPF) topologies: (a) current-driven BPF and (b) voltage-driven BPF. R_s represents finite driving source resistance in each case.

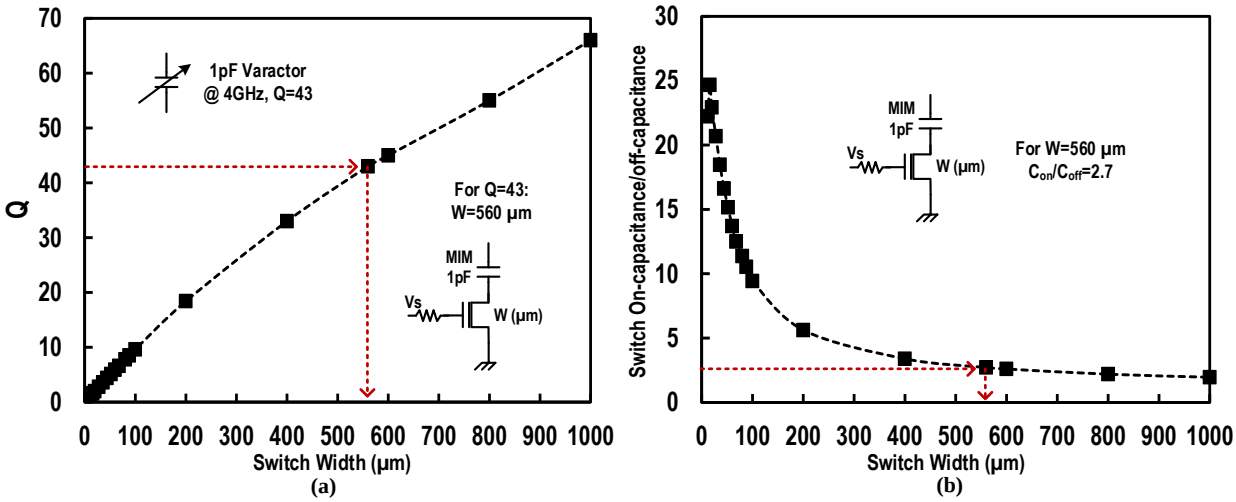

Figure 2.2: Switch-capacitor trade-off between Q and tuning range, (a) Q of the switch-capacitor versus switch width, (b) Tuning ratio (C_{on}/C_{off}) versus switch width.

current-mode BPF. In terms of selectivity, the source resistance, R_s, in the voltage-mode BPF is added incrementally to the filter resistance, not limiting the filter Q. But the R_s in the current-mode BPF will load the LC filter, potentially limiting the filter Q. In practice, however, by increasing the strength of the negative resistance, the limitation of the R_s on the filter Q can be eliminated. The proposed BPF shown in Figure 2.9 utilizes both current- and voltage-driven structures so as to optimally leverage the distinctive merits of each topology depending on system applications and requirements.

2.2 Varactor or Switch-Capacitor to Achieve 2:1 Frequency Tuning

To achieve 2:1 frequency tuning range, the capacitance ratio should be at least 4:1. In addition to the tuning ratio, quality factor of the capacitor is also important because lower Q needs more negative resistance to compensate limited Q of the capacitor and therefore power dissipation, noise and, nonlinearity increase.

The first and simplest approach for frequency tuning is a switch-capacitor network [28]. However, switch parasitic will limit the tuning range. Figure 2.2 compares a varactor with a switch-capacitor in terms of Q and tuning ratio for the same capacitance value. NMOS varactor with 1 pF at 4 GHz which has more than 4:1 capacitance ratio, can achieve Q of 43; to obtain same Q using switch cap, switch width should increase (switch on-resistance is inversely proportional to the MOSFET width). As the switch width increases, Q increases at the cost of higher parasitic which limits the tuning range. Figure 2.2 (a) shows that the switch width for Q=43 should be at least 560 µm. By setting W=560 µm, the capacitance ratio when the switch is on to the off state would be 2.7 (Figure 2.2 (b)), therefore 4:1 capacitance tuning is not possible

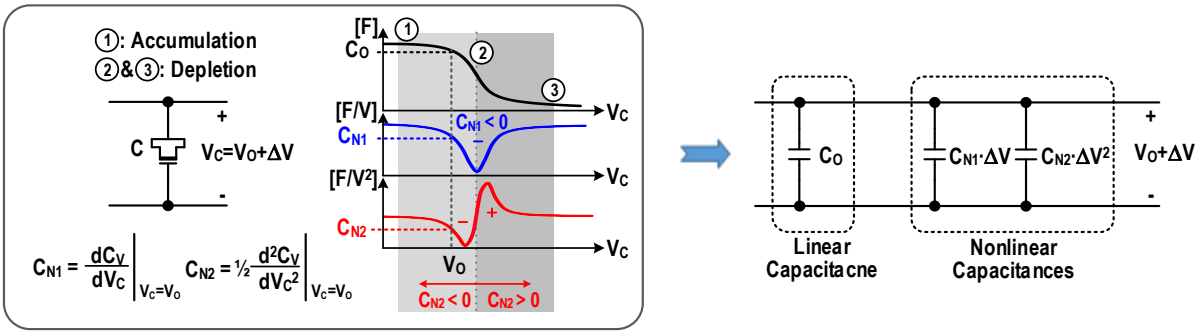

Figure 2.3: Nonlinear varactance of accumulation mode varactor and its modeling using truncated power series. C_O: linear fixed capacitance at DC (V_C=V_O), C_{N1}·ΔV: nonlinear capacitance proportional to ΔV, and C_{N2}·ΔV^2: nonlinear capacitance proportional to ΔV^2. ΔV:

using switch-capacitor network. The second option to obtain frequency tuning is varactor, in which large capacitor tuning with high Q is possible. However, when NMOS varactor experiences sharp transition from accumulation to saturation (Figure 2.3) it generates nonlinearity, which is of the main nonlinear elements in filter design and limits the dynamic range [29]. In section 2.3, varactor nonlinearity is explained and the proposed varactor control technique to overcome the dynamic range problem of Q-enhanced LC filters is discussed.

2.3 LC-Tank Nonlinearity

Varactor and negative resistance cells are two dominant nonlinear sources in the Q-enhanced LC tank. In this section, first, the nonlinearity of a varactor is modeled with a truncated power series. Then, a nonlinear passive feedback model has been developed to formalize the nonlinear coefficients of the LC tank with the varactor and thereby to develop a closed form expression for 1-dB gain compression point (P_{-1dB}). Finally, the nonlinear feedback and mathematical models are expanded by incorporating the nonlinear effect of the negative resistance to fully address the Q-enhanced LC tank nonlinearity.

2.3.1 Nonlinearity in the Varactor

In general accumulation mode MOS varactors (Figure 2.3), when the control voltage of the varactors passes the accumulation mode (①), the varactor experiences a sharp nonlinear transition in the depletion mode (②), causing a severe nonlinearity until the varactance saturates to its low limit (③) [29]. To explore the nonlinearity of the MOS varactor, its nonlinear varactance (C_V) has been modelled with a truncated power series around the DC quiescent point ($V_C|_{DC}$=V_O), which is expressed as:

$$C_V(V_C) = C_V(V_O + \Delta V) = C_o + C_{N1} \cdot \Delta V + C_{N2} \cdot \Delta V^2$$

, where

$$V_C = V_O + \Delta V \quad (1)$$

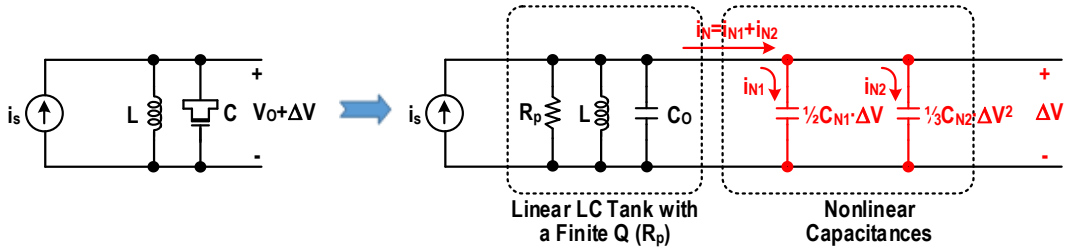

Figure 2.4: Nonlinear modeling of LC tank comprised of an inductor and nonlinear MOS varactor. The MOS varactor is replaced with the nonlinear varactance model developed in Figure 2.3 around the output DC operating point (VDC=VO). The LC tank loss contributed by the finite losses from the inductor and varactor is collectively represented by R_p.

where ΔV is the AC component of the varactor output. The C_o is a fixed linear capacitance dependent on the DC operating point. The C_{N1} [F/V] and C_{N2} [F/V^2] are first- and second-order nonlinear capacitive coefficients that can be extracted by taking first- and second-order derivatives of the varactance with respect to the applied DC control voltage as shown in Figure 2.3. The C_{N1} has always negative value addressing monotonic decrease of capacitance versus the incremental voltage variation of ΔV, whereas C_{N2} experiences its polarity change in the middle of the varactance excursion accounting for the quadratic capacitance variations before and after the middle point in Figure 2.3. The incremental charge across the nonlinear capacitance can be given as

$$dQ_V(V_C) = C_V(V_C) \cdot dV_C. \qquad (2)$$

Consequently, the time varying current across the capacitance can be expressed as

$$\begin{aligned} i_V(V_c) &= \frac{dQ_V(V_C)}{dt} = C_V(V_c) \cdot \frac{dV_C}{dt} \\ &= C_o \cdot \frac{d}{dt}\Delta V + \frac{C_{N1}}{2} \cdot \frac{d}{dt}\Delta V^2 + \frac{C_{N2}}{3} \cdot \frac{d}{dt}\Delta V^3 \\ &= j\omega \left(C_o + \frac{C_{N1}}{2} \cdot \Delta V + \frac{C_{N2}}{3} \cdot \Delta V^2 \right) \Delta V. \end{aligned} \qquad (3)$$

Thus, in AC-wise the C_{N1} becomes half and C_{N2} becomes a third of its original value.

2.3.2 Nonlinearity in the LC Tank

In the LC tank comprised of an inductor and nonlinear MOS varactor in Figure 2.4, the nonlinear MOS varactance around its output DC is replaced with the nonlinear model developed in (1). In the equivalent circuit driven by a linear current source, in Figure 2.5, i_{N1} and i_{N2} represent the 2nd and 3rd order nonlinear currents, corresponding to the second and third terms inside the parenthesis in (3), respectively. In a small signal approximation or weak nonlinearity, the C_o,

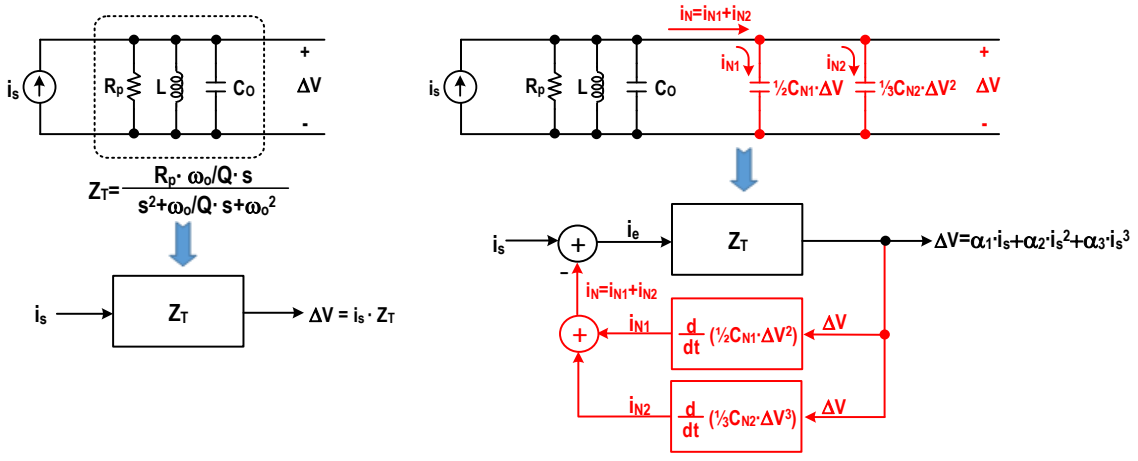

(a) (b)

Figure 2.5: Nonlinear feedback model of the LC tank: (a) transimpedance network model of the linear portion of the current driven LC tank, and (b) nonlinear current feedback model of the nonlinear capacitances in the LC tank.

C_{N1} and C_{N2} would not change with a small enough disturbance of ΔV. In such a case, by configuring a differential circuit, the 2nd order nonlinearity in (3) would be negligible and the linear current can be approximated to $\Delta V/R_p$ at center frequency. Therefore, the peak voltage magnitude that causes 1 dB compression at the resonance frequency can be found as

$$\Delta V_{P,IP3}{}^2 \cong \frac{4}{3} \cdot \frac{1/R_p}{\omega_o |C_{N2}|/3} = \frac{4}{Q} \cdot \frac{C_o}{|C_{N2}|}$$

, where $$\omega_o = 1/\sqrt{LC_o} \text{ and } Q = \omega_o R_p C_o. \quad (4)$$

This is valid when the varactor is biased in the flat regions ① and ③ in Figure 2.3. It is noteworthy that $\Delta V_{P,IP3}{}^2$ is inversely proportional to the Q, addressing the ingrained tradeoff between selectivity and linearity in varactor-tuned integrated LC filters. In the heavily nonlinear region (region ② in Figure 2.3), however, a small variation of ΔV could cause substantial changes of the coefficients of C_o, C_{N1} and C_{N2}, invalidating the small signal approximation. In this strong nonlinear circumstance, the C_{N1} cancellation effect becomes less prominant and the 2nd order nonlinearity can affect the 3rd order nonlinear distortion.

$$\Delta V = \alpha_1 \cdot i_s + \alpha_2 \cdot i_s{}^2 + \alpha_3 \cdot i_s{}^3. \quad (5)$$

In the feedback model, ΔV can also be given as

$$\Delta V = i_e \cdot Z_T(\omega) = (i_s - i_{N1} - i_{N2}) \cdot Z_T(\omega)$$

$$= \left(i_s - \frac{j\omega C_{N1}}{2}\Delta V^2 - \frac{j\omega C_{N2}}{3}\Delta V^3\right) \cdot Z_T(\omega). \quad (6)$$

In (6), $Z_T(\omega)$ can be approximated to (7) for each different current.

$$Z_T(\omega) = \frac{j\omega \frac{\omega_o}{Q} \cdot R_p}{{\omega_o}^2 - \omega^2 + j\omega \frac{\omega_o}{Q}}$$

$$= \begin{cases} Z_T(\omega_o) = R_p, & for\ i_s\ at\ \omega = \omega_o \\ Z_T(2\omega_o) \cong -j\frac{2}{3}\frac{R_p}{Q}, & for\ i_{N1}\ at\ \omega = 2\omega_o. \\ Z_T(3\omega_o) \cong R_p, & for\ i_{N2}\ at\ \omega = 3\omega_o \end{cases} \quad (7)$$

It should be mentioned that only the fundamental component of the 3rd order IMD products will be of concern. Thus, the tank impedance is approximated to R_p for i_{N2} in (7). At resonance, applying (7) to (6) results in

$$\Delta V = i_s R_p - \frac{\omega_o C_{N1} R_p}{3Q}\Delta V^2 - \frac{j\omega_o C_{N2} R_p}{3}\Delta V^3. \quad (8)$$

By substituting the ΔV in (6) with the power series in (5), the nonlinear coefficients, α_1, α_2, and α_3 under the feedback can be found and the results are given in (9)-(11) (see APPENDIX A for more details).

$$\alpha_1 = R_p. \quad (9)$$

$$\alpha_2 = -\frac{\omega_o C_{N1} {R_p}^3}{3Q}. \quad (10)$$

$$\alpha_3 = -j\frac{\omega_o C_{N2} {R_p}^4}{3}\left(1 - \frac{2{C_{N1}}^2}{C_o C_{N2}}\right) \quad (11).$$

In order to find $\Delta V_{P,IP3}$ (5) needs to be transformed to its Thevenin equivalent form which can be done by replacing the i_s with v_s/R_p, resulting in

$$\Delta V = \alpha_1 \cdot \frac{v_s}{R_p} + \alpha_2 \cdot \left(\frac{v_s}{R_p}\right)^2 + \alpha_3 \cdot \left(\frac{v_s}{R_p}\right)^3. \quad (12)$$

Consequently, the $\Delta V_{P,1dB}$ will be found to be

$${\Delta V_{P,1dB}}^2 \cong 0.145 \cdot \frac{\alpha_1}{|\alpha_3|} \cdot {R_p}^2 = \frac{0.435}{Q} \cdot \frac{C_o}{|C_{N2}|} \cdot \left|1 - \frac{2{C_{N1}}^2}{3C_o C_{N2}}\right|^{-1}. (13)$$

Apparently, (13) will be reduced to (4) when $C_{N1} = 0$. It is also noteworthy that even if $C_{N2} = 0$ $\Delta V_{P,IP3}$will be limited to $\sqrt{2/Q} \cdot |C_o/C_{N1}|$, still being affected by the 2nd order nonlinearity and being traded with the filter Q. The sweet spot where peak $\Delta V_{P,IP3}$ will happen is around the bias

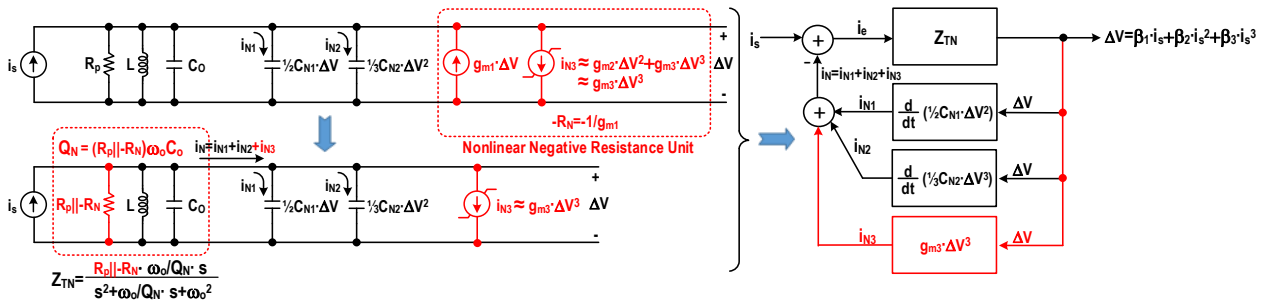

Figure 2.6: Nonlinear feedback model of the Q-enhanced LC tank. It is assumed that unlike the varactor, the negative resistance circuit would maintain a weak nonlinearity, preserving a small signal approximation. This allows rejection of the second order nonlinearity using a differential circuit.

point where $C_o = 2{C_{N1}}^2/C_{N2}$. The verification of the mathematical model through CADENCE simulations will be provided after completing the discussion by including the nonlinearity of a negative resistance unit in the following section.

2.3.2 Nonlinearity in the Q-Enhanced LC Tank

Figure 2.6 shows the nonlinear feedback model of the LC tank of which loss is partially compensated by a negative transconductor circuit to enhance the Q of the LC tank. The nonlinearity of the negative transconductance is modelled using a three-term power series: $-g_{m1}$ ($-1/g_m=-R_N$) represents a linear transconductance supplying current proportional to ΔV to the LC tank, and g_{m2} and g_{m3} are the 2nd and 3rd order nonlinear coefficients accounting for the distortion of the replenishing current. It is assumed that the transconductor would suffer from a weak nonlinearity preserving small signal approximation over the course of ΔV swing, allowing rejection of the even mode distortion by utilizing a differential circuit. Unlike varactor, this should be a valid assumption for typical differential active circuits under small signal perturbation. Thereby, in general differential Q-enhanced LC tanks, the nonlinearity of the negative transconductor will be dominated by the 3rd order nonlinear current which can be modelled in parallel with the varactor nonlinearity in the feedback system in Figure 2.6.

The net effect of the nonlinearity of the negative transconductor is the modification of the 3rd order nonlinear coefficient in the feedback model. Thus, all the mathematic expressions made in the previous section will hold by replacing these parameters,

$$R_p \rightarrow R_{pN} = R_p \parallel -R_N, where\ R_N = \frac{1}{g_{m1}} \quad (14)$$

$$Q \rightarrow Q_N = \omega_o R_{pN} C_o, \quad (15)$$

$$j\frac{\omega_o C_{N2}}{3} \rightarrow j\frac{\omega_o C_{N2}}{3} + g_{m3}. \quad (16)$$

If we introduce a new power series to describe the nonlinearity of the feedback system in Figure 2.6 as

$$\Delta V = \beta_1 \cdot i_s + \beta_2 \cdot {i_s}^2 + \beta_3 \cdot {i_s}^3 \qquad (17)$$

Then,

$$\beta_1 = R_{pN}, \qquad (18)$$

$$\beta_2 = -\frac{\omega_o C_{N1} {R_{pN}}^3}{3Q_N}, \qquad (19)$$

$$\beta_3 = -{R_{pN}}^4 \left\{ j\frac{\omega_o C_{N2}}{3}\left(1 - \frac{2{C_{N1}}^2}{C_o C_{N2}}\right) + g_{m3} \right\}. \qquad (20)$$

Therefore, complete $\Delta V_{P,1dB}$ including the nonlinearity of the negative resistance circuit will be given as

$${\Delta V_{P,1dB}}^2 \cong 0.145 \cdot \frac{\beta_1}{|\beta_3|} \cdot {R_{pN}}^2$$

$$= \frac{0.435}{Q_N} \cdot \frac{C_o}{|C_{N2}|} \cdot \left\{ \left(1 - \frac{2{C_{N1}}^2}{3C_o C_{N2}}\right)^2 + \left(\frac{3g_{m3}}{\omega_o C_{N2}}\right)^2 \right\}^{-1}. \qquad (21)$$

2.3.3 Verification of the Nonlinear Models

The simulation schematic to verify the nonlinear mathematic models of (13) is illustrated in Figure 2.7. For plotting input 1dB compression point (IP_{-1dB}) based on the theoretical equation, the nonlinear coefficients of the varactor need to be obtained from simulation. Therefore, the effective capacitance versus the voltage across the varactor is plotted using Cadence and the required coefficients are extracted by taking the first and second derivatives of the capacitance with respect to its voltage. IP_{-1dB} is then plotted by plugging the numbers from capacitance characterization into equation (13). The value of Q is calculated by assuming 350 Ω and 325 pH for the effective resistance and inductance of the tank, respectively. As can be observed from Figure 2.7, the nonlinear modelling of the varactor is validated for 4-8 GHz, which is one of the target frequency bands of this work. It is noteworthy to mention the frequency in which IP_{-1dB} reaches its maximum is very sensitive to the value of C_{N1} and C_{N2} and depends on how accurately the coefficients are modelled; the frequency of perfect coefficient cancellation varies. However, the overall nonlinear behavior of the capacitance remains unchanged regardless of characterization resolution.

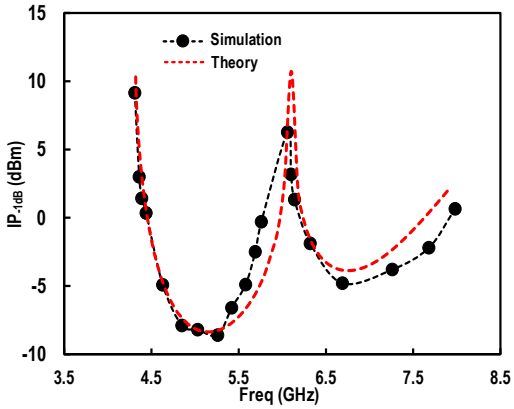

Figure 2.7: IP_{-1dB} versus frequency using cadence and eq. (13).

2.4 Q-Enhanced LC tank noise model

Figure 2.8 (a) shows the main noise sources in the Q-enhanced LC filter. To relax the linearity-noise trade off space, Q_1 and Q_2 are deriving the LC tank as a voltage mode and current mode, respectively. Negative resistance is the main source of noise in Q-enhanced LC tank; as the Q increase, the negative resistance strength increases, thus noise increases. The Q-enhanced filter NF can be expressed as

$$NF \approx 1 + \frac{4KT\left(\frac{1}{R_p} + \frac{1+k}{R_c} + G_{m2} + \frac{r_{b2}}{(re_2 + R_E)^2} + \gamma(g_{m3} + g_{ds3})\right)}{4KT \cdot 50} \cdot \frac{4R_c^2}{(1 + G_{m2}R_c)^2}. \qquad (22)$$

In which $k=r_{e1}/2R_c$, $r_{e2}=1/g_{m2}$, $G_{m2}=1/(r_{e2}+R_E)$, and $\gamma(g_{m3}+g_{ds3})$ is the noise of the triode NMOS in parallel with a resistor that controls the negative resistance. In (22) the first term is due to the matching resistor and the second term is due to the LC tank and drivers. In the proposed filter, noise due to R_p and R_c are negligible, therefore $1/R_p$ and $(1+k)/R_c$ are much smaller than other terms and will not be considered further for analysis. Current driver and variable resistor in negative gm cell are dominant noise sources. To write (22) based on the gain and quality factor of the filter:

$$A_v = (1 + G_{m2}R_c) \cdot \frac{R_{eq}}{R_c + R_{eq}} \cdot \frac{1}{2} \qquad (23)$$

In which $R_{eq}=R_p||R_{-gm}$, and 1/2 is due to 50Ω matching.

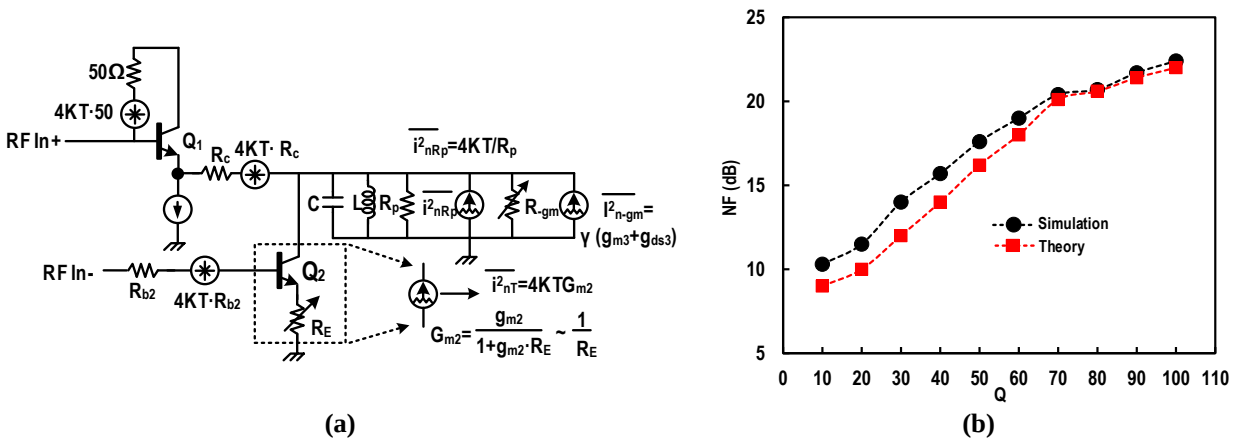

Figure 2.8: (a) Q-Enhanced LC tank noise model including voltage driver (Q_1) and current driver (Q_2). (b) NF versus Q of the filter for constant gain of 10 dB for simulation and eq. (26).

$$Q = R_{eq}/\sqrt{L/C} \qquad (23)$$

$$A_v = \frac{G_{m2}}{2} \cdot Q\sqrt{L/C} \qquad (24)$$

$$G_{m2} = \frac{2A_v}{Q\sqrt{L/C}} \cdot \qquad (25)$$

Therefore, NF based on the gain and Q of the filter is

$$NF \approx 1 + \frac{4KT \cdot 50}{4KT.R_s}$$

$$+(0.08).\left(\frac{Q\sqrt{L/C}}{2A_v} + r_{b2} + \frac{\gamma(g_{m3}+g_{ds3})}{4A_v^2} \cdot Q^2 \cdot \frac{L}{C}\right) \qquad (26)$$

Figure 2.8 (b) shows the NF versus Q in simulation using CADENCE with 0.13 µm BiCMOS IBM H8P model as well as the model of (26). For noise analysis, the total gain of the filter is considered as 10 dB for all Q cases. Therefore, as Q increases, the total tank resistance increases so the R_E should increase to decrease the gain of the current mode driver and keep the total gain of the filter constant. This generates more noise since by increasing Q, current driver path is turning off gradually to keep the total gain of the filter constant. As Figure 2.8 (b) shows, in lower Q case simulation and (26) have ~1 dB difference due to NF approximation, but as Q increases, negative resistance noise contribution is much higher than the terms which are neglected so, theory matches the simulation very well. NF derivation details for (22) and (26) are shown in APPENDIX B.

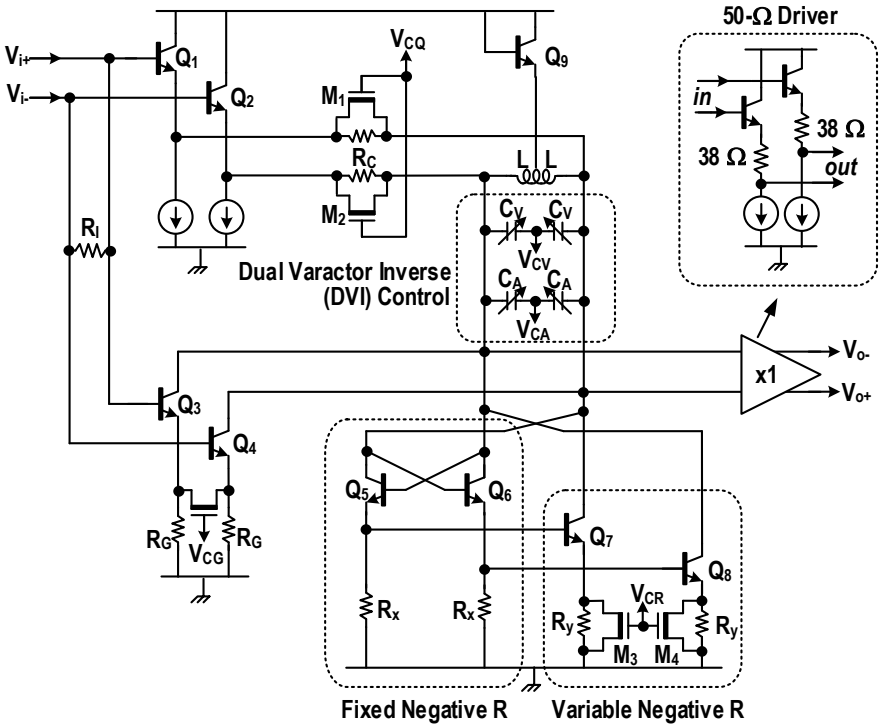

Figure 2.9: The complete schematic of the proposed Q-enhance LC band-pass filter.

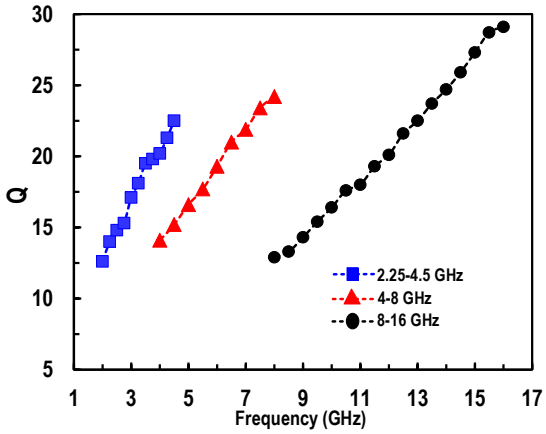

Table I. LC Tank Parameters

Frequency	L (pH)	C (pF)	The Intrinsic LC Tank Q
2-4 GHz	832	1.3~6.1	14~20
4-8 GHz	325	1~4.2	14~24
8-16 GHz	125	0.7~3	13~29

Figure 2.10: Intrinsic LC tank Q for 2.25-4.5 GHz, 4-8 GHz and 8-16 GHz designs.

2.5 Bandpass Filter Design

In Figure 2.9, $Q_{1,2}$ drives the LC filter tank in voltage mode with ~15 Ω driving impedance (Ibias=1.5 mA/path) while the degenerated variable gain transconductor composed of $Q_{3,4}$ and R_G drives the passive filter network in current-mode (I_{bias}=1 mA/path). The range of varistance by R_G and triode NMOS is 10~450 Ω. Decreasing R_G makes the current mode stronger, resulting in better NF. The R_G, however, can be set to its maximum when linearity is of primary concern. Input matching is established with a resistor termination by R_I (100 Ω), mainly for interface with

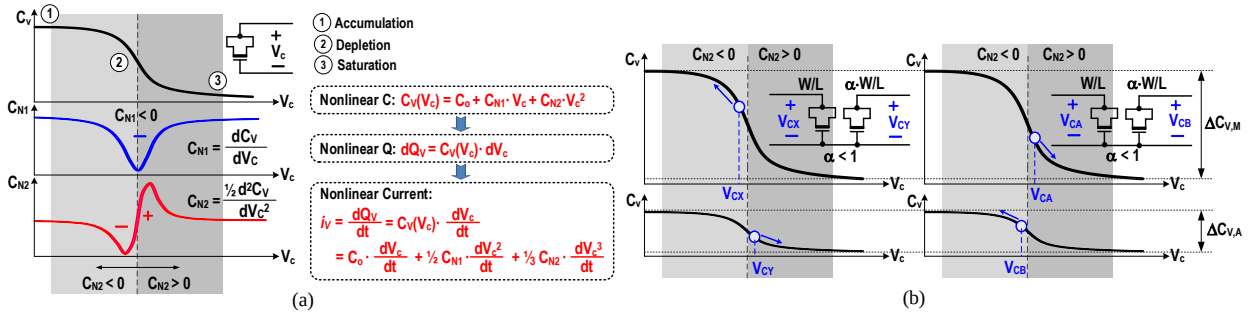

Figure 2.11: Dual varactor inverse (DVI) control: (a) nonlinearity in typical single varactor control and (b) DVI control to improve linearity of the varactor. The varactor is "NFET in n-well" structure.

measurement equipment. The 50-Ω driver buffers filter output with minimal loading effect on the LC tank. In the proposed circuit, L and two varactors C_V and C_A comprise the frequency tunable LC tank. Table I shows the LC tank parameters for three different designs, 4-8 GHz, and 8-16 GHz tunable frequency when including layout parasitics. Figure 2.10 shows the intrinsic LC tank Q versus frequency which is 14-20, 14-24, and 13-29 over the frequency tuning range of 2.25-4.5 GHz, 4-8 GHz, and 8-16 GHz. The base of $Q_{1,2}$ is biased at V_{CC} and therefore the diode Q_9 sets an equal bias voltage across $M_{1,2}$, driving the $M_{1,2}$ into deep triode region. Thus, a lower filter Q than the intrinsic LC tank Q can be obtained by controlling the MOS triode resistance in parallel with the R_C (350 Ω). The Q_9 also provides bias current for the negative transconductor.

2.5.1 Dual Varactor Inverse (DVI) Control

The varactor nonlinearity is a major nonlinear source in the LC tank. As shown in Figure 2.11(a), when the control voltage of an accumulation-mode MOS varactor passes the accumulation mode (①), the varactor experiences a sharp nonlinear transition in the depletion mode (②), causing a severe nonlinearity until the varactance saturates to its low limit (③). The expression of the nonlinear varactance in Figure 2.11 (a) is an approximation using a truncated power series around the operating point: C_o is a linear capacitance where charge (Q_V) accumulates linearly, creating a linear time varying current ($=C_o\cdot dV_c/dt$) for a given control voltage (V_c). C_{N1} and C_{N2} represent nonlinear capacitance coefficients dependent on the first and second order of applied control voltage and therefore generate 2nd and 3rd-order nonlinear currents, respectively.

For differential LC tank, the nonlinearity caused by C_{N1} will be negligible and it is critical to suppress C_{N2} to linearize the LC tank. To achieve this, a dual varactor inverse (DVI) control scheme is proposed as shown in Figure 2.11 (b). The polarity of C_{N2} changes approximately in the middle of the varactance range. In the DVI control, when main varactor voltage deviates from the middle point, the control voltage of the auxiliary varactor, C_A, moves in the opposite direction so that C_{N2} of the two varactors can be cancelled out in the heavily nonlinear region.

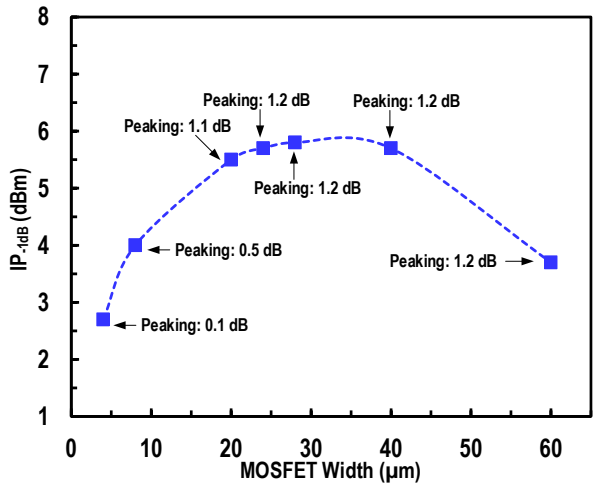

Figure 2.12: IP_{-1dB} improvement with dynamic resistance by MOSFET size optimization.

The main varactor size (or varactance range of $\Delta C_{V,M}$ in Figure 2.11 (b)) needs to be larger than the auxiliary varactor size (or varactance range of $\Delta C_{V,A}$ in Figure 2.11 (b)) to achieve the target tuning range. In this design, a 3:1 size ratio (α=1/3 in Figure 2.11 (b)) is used for the main and auxiliary varactors. Furthermore, by optimizing the control voltages IP_{-1dB} can be improved by more than 10 dB at 3 GHz in simulation.

2.5.2 LC-Resonator with Dynamic Negative Resistance

The negative resistance needs to be variable to get Q tunability. However, the direct control of R_x will induce different loading capacitance to the LC resonator, causing frequency drift depending on the R_x change. This Q-dependent frequency error can be minimized by isolating the Q-tuning element from the LC tank. In Figure 2.9, $Q_{5,6}$ and R_x (200 Ω) produce a fixed negative resistance and isolates the variable negative resistance cell composed of $Q_{7,8}$, R_y (400 Ω) and $M_{3,4}$ from the LC tank.

When the LC resonator output swing is large enough the $Q_{7,8}$ will drive $M_{3,4}$ toward deep triode region and the MOS resistance is no longer a small-signal static resistance but a large-signal dynamic resistance which depends on the output signal swing. Figure 2.12 shows that by optimizing the size of $M_{3,4}$ and R_y, it is possible to change the dynamic resistance and increase gain peaking to achieve higher compression point. Size of NMOS is chosen 20 μm to obtain ~ 1dB of gain peaking. Figure 2.13 (a) shows the change in negative resistance as the output swing increases. When the negative resistance increases, the total tank resistance will increase, therefore, output gain increases and the resulting gain peaking improves power handling of the filter (Figure 2.13 (b)).

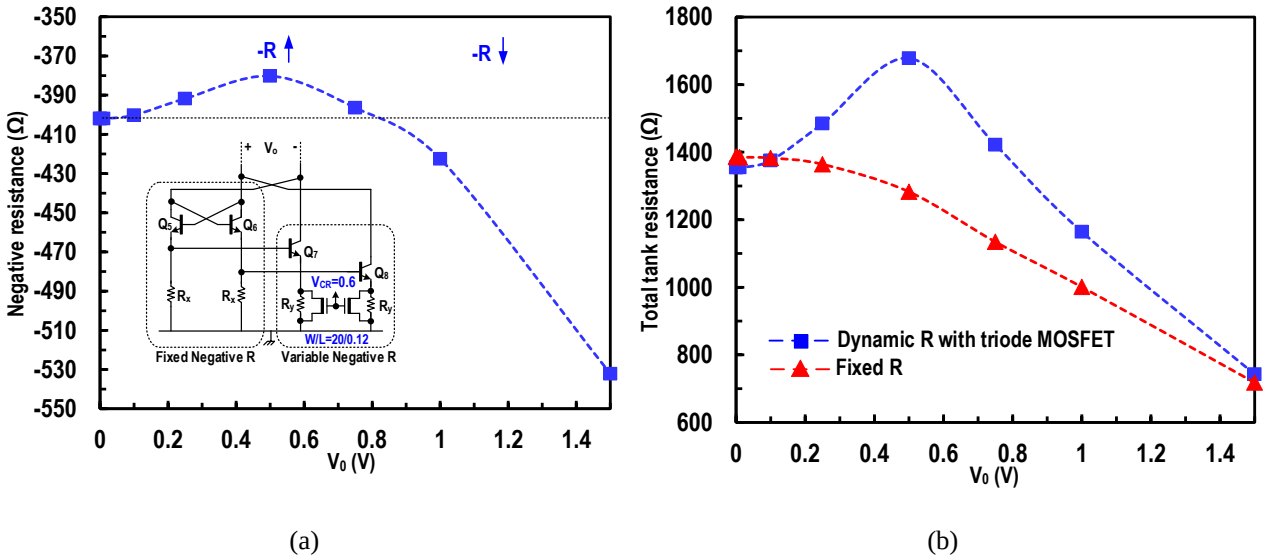

(a) (b)

Figure 2.13: (a) Dynamic negative resistance versus output voltage swing (b) Total tank resistance versus output voltage swing.

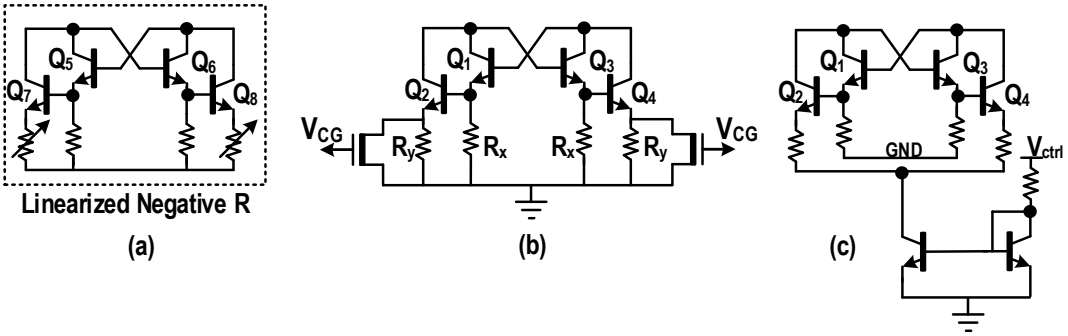

Figure 2.14: (a) Linearized variable negative gm cell. (b) Variable negative resistance using triode NMOS in parallel with a resistor. (c) Variable negative resistance using current source.

After the compression point, $Q_{5,6}$ and $Q_{7,8}$ start to deviate from the forward-active region, decreasing the dynamic resistance (Figure 2.13 (b)). The composite negative transconductor together with the variable RC enables 3 to >100 of Q control range over the entire target frequency band with stable circuit operation in simulation. The fixed negative resistance unit consumes 2 mA and the variable negative transconductor takes 2-5 mA per path from 3.3 V supply depending on the Q control.

2.5.3 NF-Linearity Tradeoff in Q-Enhanced LC Tank

As mentioned in section 2.5.2, to achieve higher Q than intrinsic LC tank Q, variable negative resistance is required. Figure 2.14 shows two ways to change negative resistance; in (b) the negative resistance changes using a triode NMOS in parallel with R_y. As described in LC

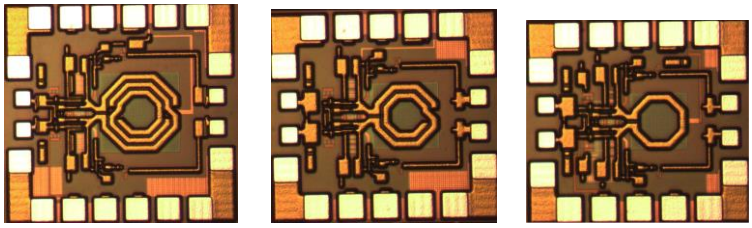

Figure 2.15: Chip photograph, (a) 2.25-4.5 GHz size 0.7×0.68 mm^2 (b) 4-8 GHz 0.7×0.68 mm^2 (c) 8-16 GHz 0.6×0.58 mm^2, including pads.

resonator with dynamic resistance, by appropriate sizing of NMOS, the dynamic negative resistance is obtained which improves IP_{-1dB} by 2-3 dB with introducing gain peaking. In terms of noise, Eq. (22) shows the noise contribution from triode NMOS which is $\gamma(g_{m3}+g_{ds3})$, is considerable and increases the NF by 2-3 dB. However, if the negative resistance is changed using a current source, there is no peaking and therefore IP_{-1dB} would degrade by 2-3 dB, while NF will improve by the same factor. This design is optimized for maximum linearity, so the triode NMOS in parallel with a resistor is utilized to improve linearity in linearized negative g_m cell.

2.6 Experimental Results

The proposed band-pass filter is designed and implemented at three different frequency bands using 0.13 μm SiGe BiCMOS technology (1P7M, f_T/f_{max}=180/220 GHz). Since the filters are pseudo-differential circuits, highly symmetric layouts are striven for differential matching. The chip photographs for S-band, C-band, and X-Ku band designs are shown in Figure 2.15. The silicon chips are measured after differential SOLT calibration with GSSG probes (calibration step: ~3 MHz). 180-degree hybrid couplers are used at the input and output, for single-ended interface with measurement equipment. The BPF measurements confirm that the filter Q can be increased from less than 5 up to 100 over the entire frequency bands by controlling the R_C and R_Y in Figure 2.9, with stable circuit operation (K-factor > 1). For 2-4 GHz design, the measured DC current ranges 13-20 mA from 3.45 V supply voltage, depending on the Q control. For 4-8 GhHz filter, the DC current is 17-21 mA from 3.3 V supply voltage. For 8-16 GHz filter, the DC current is 15-26 mA from 3.45 V supply voltage.

Filter center frequency with varactor control, 2:1 can be tuned continuously for all measured chips. Figure 2.16 (a), (b), and (c) show measured band-pass filter frequency tuning characteristics with 0.25 GHz and 0.5 GHz step for the S-band, C-band, and X-Ku bands design, respectively. In this case, the BPF gains are adjustable from 0-20 dB for all measured frequencies.

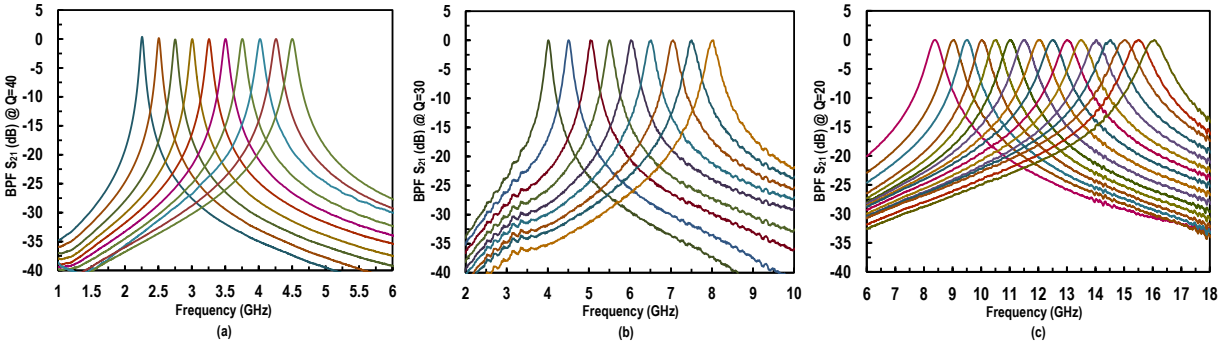

Figure 2.16: Measured frequency tuning characteristic for (a) 2.25-4.5 GHz, (b) 4-8 GHz, and (c) 8-16 GHz.

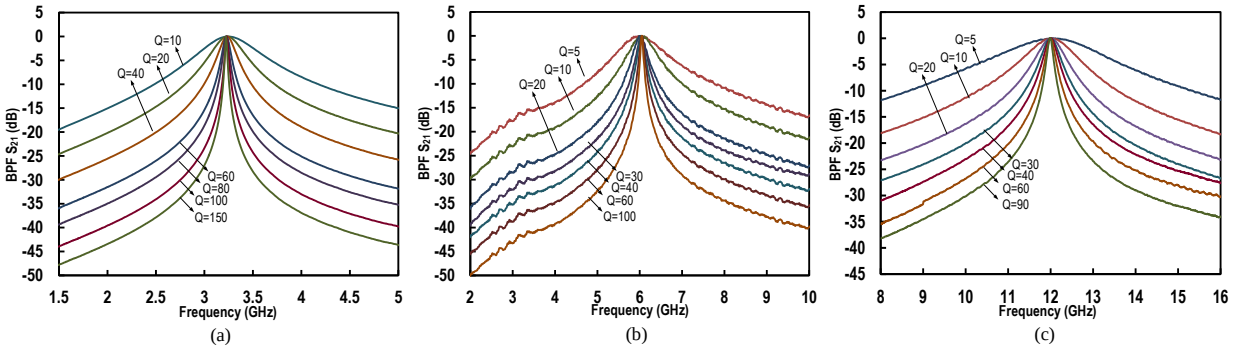

Figure 2.17: Measured bandwidth tuning characteristic for (a) 2.25-4.5 GHz, (b) 4-8 GHz, and (c) 8-16 GHz.

Figure 2.16 shows the normalized S_{21} response. Note that in actual on-chip system integration, the input and output 50-Ω termination may not be necessary. Then without 50-Ω matching loss, filter voltage gain could be 12 dB higher than the measurement. Figure 2.17 displays measured BPF responses for different BPF Q settings, at 3.25 GHz in Fig 2.17 (a), at 6 GHz in Fig 2.17 (b) and at 12 GHz in Figure 2.17 (c). As mentioned, the resistive 50-Ω termination establishes wideband input and output matching: measured S_{11} and S_{22} is better than -10 dB for all measurement frequencies (Figure 2.18). Since the BPF section is isolated by emitter-followers from the input and output, the bandwidth control or frequency tuning in the BPF does not alter the impedance matching performance.

Figure 2.19 (a) shows more than 8 dB improvement of IP_{-1dB} by the DVI control together with the negative resistance gain peaking technique (0.4 dB peaking), compared with conventional single varactor control. Minimum gain ranges from 0 dB at Q=3 to ~20 dB at Q=150. As seen in Figure 2.19 (b) one can observe 0.4-0.6 dB gain peaking at high input power for virtually all high Q cases (Q>30), enhancing the power handling capability of the filter. (c) reveals typical filter tradeoffs amongst gain, linearity, and NF at Q=40 (fc=3.25 GHz): when gain increases from 8 to 20 dB, NF improves from 18 dB to 11 dB at the cost of IP_{-1dB} decreasing from 5 dBm to -7 dBm.

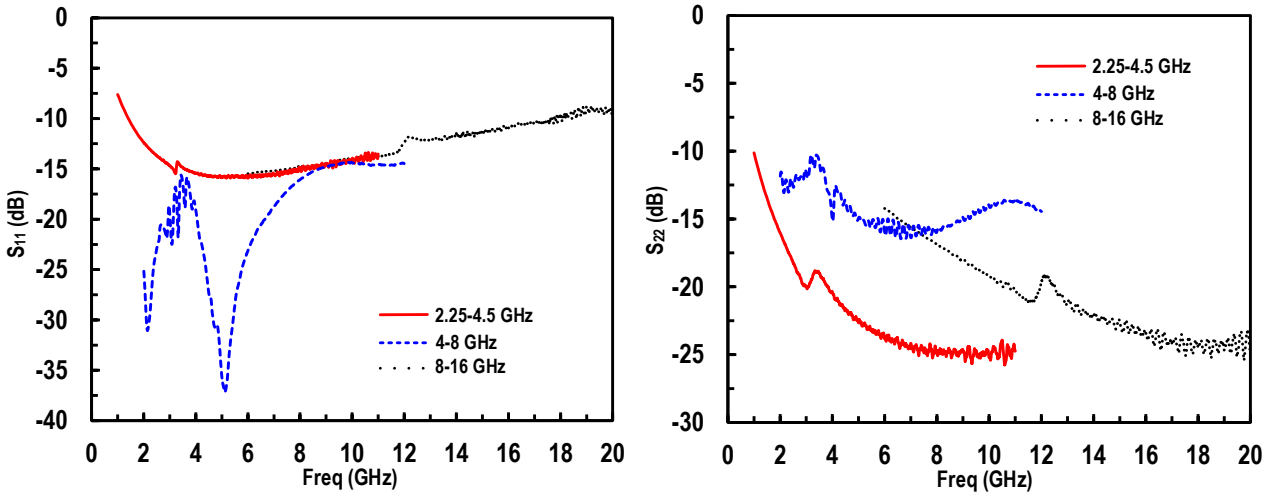

(a) (b)

Figure 2.18: (a) Measured S_{11} for 2.25-4.5GHz, 4-8 GHz, and 8-16 GHz. (b) Measured S_{22} for 2.25-4.5GHz, 4-8 GHz, and 8-16 GHz.

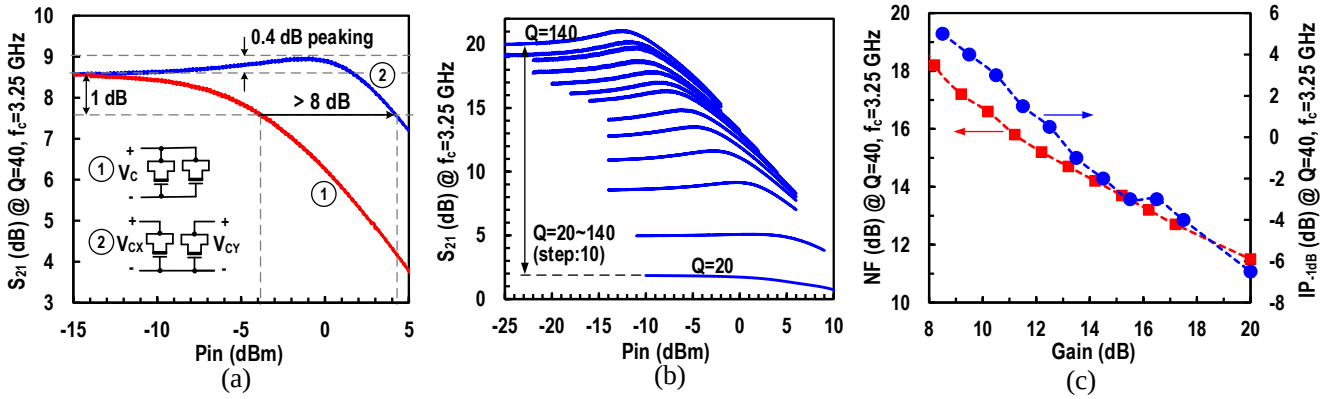

(a) (b) (c)

Figure 2.19: (a) IP_{-1dB} improvement enabled by DVI control combined with negative resistance peaking, (b) minimum gains and gain compression characteristics at different Q, and (c) gain, NF, and linearity tradeoffs at Q=40 (@fc=3.25 GHz).

Note that OP_{-1dB} is 13 dBm and fairly constant over the gain changes. Figure 2.20 shows the IP_{-1dB} improvement versus frequency with and without DVI control and gain peaking for the 2.25-4 GHz chip. At the beginning and the end of the frequency tuning range there is no difference in dynamic range since varactor is quite linear in these two regions (see Figure 2.11 for starting accumulation and deep saturation regions). However, as the frequency increases, the main and auxiliary varactors are placed in opposite regions in terms of the second order nonlinear coefficient, to cancel out the varactor nonlinearity until f > 3.75 GHz, in which there is no other choice than putting both varactors at saturation to get lower capacitance hence increasing frequency. When both varactors are placed in the same polarity region, the IP_{-1dB}

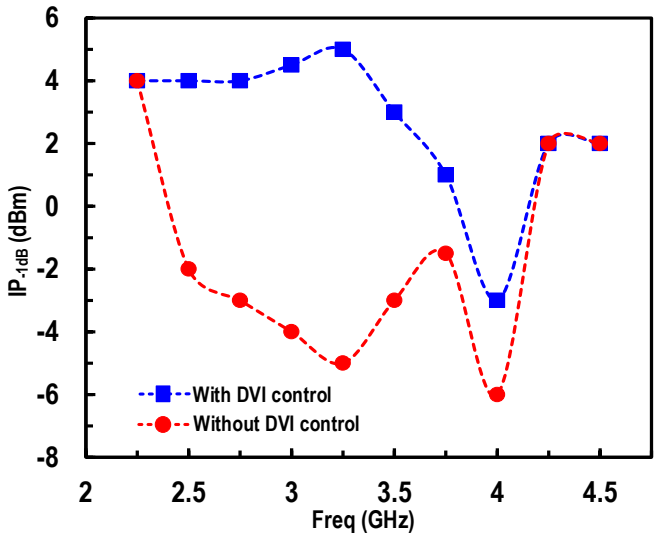

Figure 2.20: Measured IP_{-1dB} versus frequency with and without DVI control .

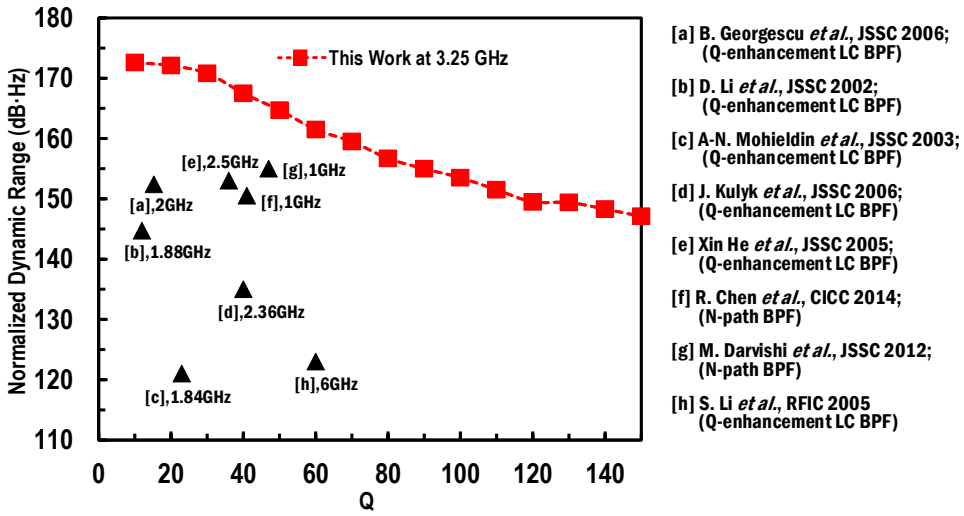

Figure 2.21: Measured normalized DR versus Q and comparison with state-of-the-art LC BPFs and N-path BPFs.

improvement is only due to the gain peaking. Figure 2.21 shows the normalized dynamic range versus Q for the 2.25-4 GHz chip in comparison with recent state of the arts. 2-4 GHz chip is chosen for dynamic range comparison because most of the recent works are below 4 GHz. As Figure 2.19 (a) and Figure 2.20, the proposed linearity improvement techniques, DVI control for varactors and gain peaking, are working properly regardless of the operation frequency. Figure 2.22 shows the NF and linearity versus Q for 4-8 GHz and 8-16 GHz chips.

A resilience to a strong in-band and out-of-band (OOB) blocker has been characterized by measuring the blocker power distancing Δf from the center frequency (fc=8GHz) that causes 1-dB gain compression of an in-band weak signal (Pin=-70 dBm). The minimum in-band blocker

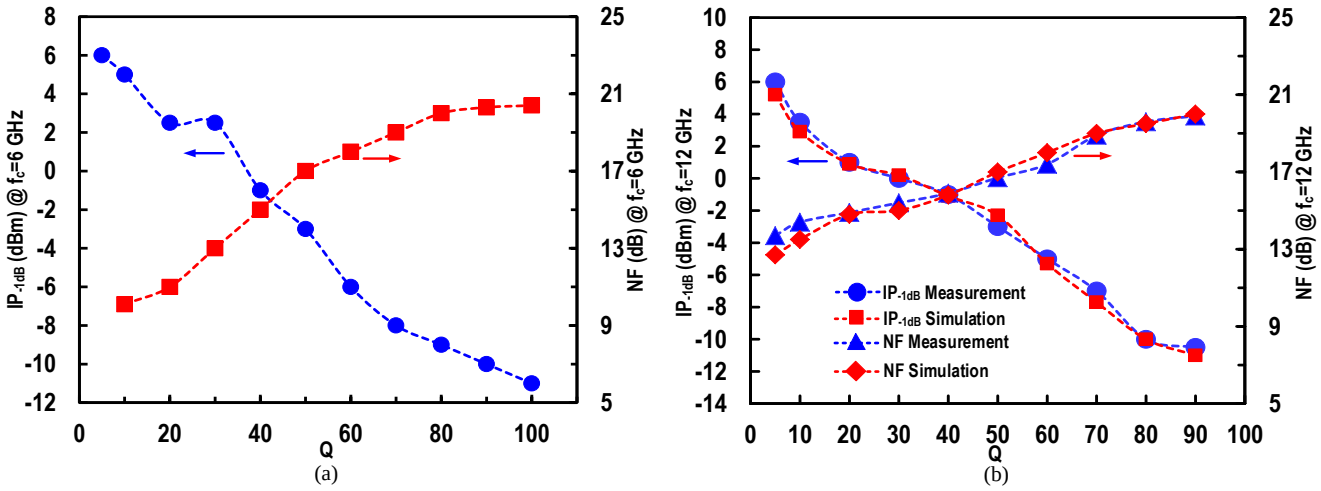

Figure 2.22: IP_{-1dB}, NF, and Q and tradeoffs at (a) 6GHz. (b) 12 GHz.

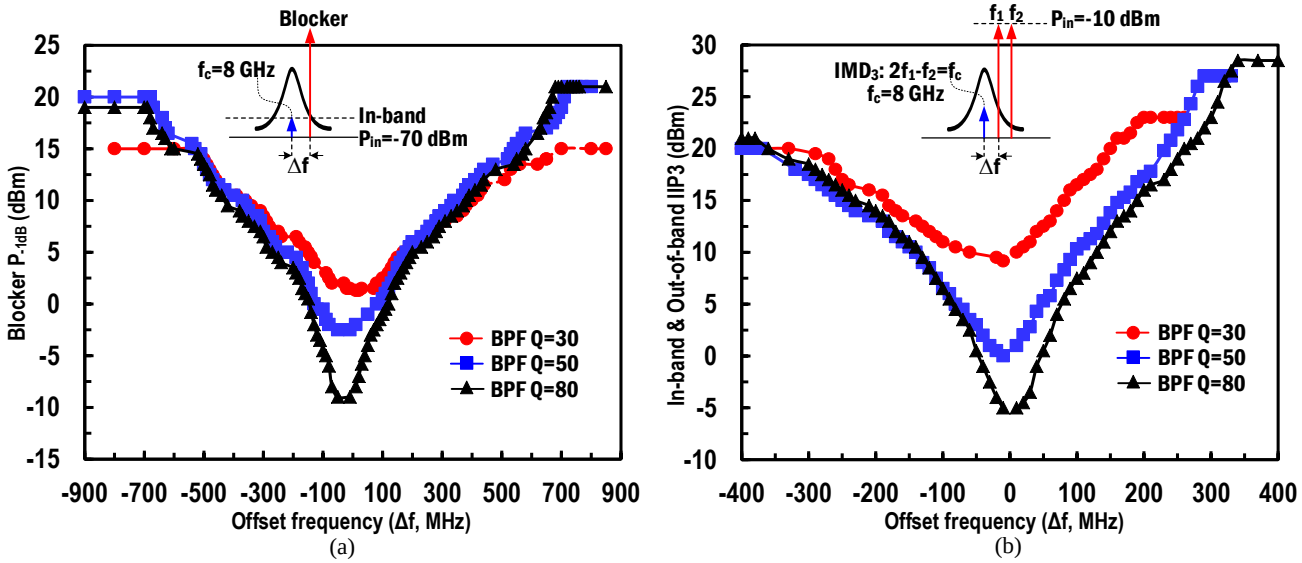

Figure 2.23: (a) Measured in-band and out-of-band (OOB) blocker power that compresses in-band small signal gain by 1-dB (Pin=-70 dBm) and (b) measured in-band and OOB IIP3. (Both measurements are at 8 GHz.)

P_{-1dB} at Δf near the f_c is +1.5dBm, -2dBm, and -8dBm when the BPF Q=30, 50, and 80, respectively. (Figure 2.23 (a)). The maximum OOB blocker P_{-1dB} is limited to ~15dBm at $\Delta f \geq 700$MHz when the BPF Q=30, which however increases further to 21dBm when $Q \geq 50$ (Figure 2.23 (a)). Similarly, in the two-tone test shown in Figure 2.23(b), when Δf is smaller than 3-dB bandwidth, the in-band IIP3 approaches to10dBm, 1dBm, and -5dBm, when the BPF Q=30, 50, and 80, respectively, while the OOB IIP3 increases up to 22dBm, 27dBm, and 28.5dBm at the each corresponding Q. In Figure 2.23, the measurement is done at 8 GHz while similar results are obtained at different frequency bands.

TABLE II: Measured Performance Summary & Comparison

	Darvishi JSSC'12 [x]	Chen CICC'14 [x]	Li JSSC'02 [x]	Mohieldin JSSC'03 [x]	Georgescu JSSC'06 [x]	This Work		
Type	N Path		Q-Enhanced LC					
Process	65 nm CMOS	65 nm LP CMOS	0.25 µm BiCMOS	0.5 µm HP CMOS	0.18 µm CMOS	0.13 µm SiGe BiCMOS		
Center Frequency (GHz)	0.4 ~ 1.2	0.1 ~ 1	1.77 ~ 1.96	1.8	1.98 ~ 2.02	2.25 ~ 4.5	4 ~ 8	8 ~ 16
Band Width (MHz)	21	24	150	80	130	15 ~ 450 @ 2.25 GHz	40 ~ 800 @ 4 GHz	80 ~ 1600 @ 8 GHz
Q tuning	NA	NA	12 ~ 13	22.5	15	5 ~ 150	5 ~ 100	5 ~ 100
Gain (dB) @ f_c	-2, -3.2[a]	23	-2	9	0	0 ~ 20	0 ~ 20	0 ~ 20
NF (dB)	10[b]	3.5 ~ 4.1	22.2	46	15	11.5 @ 3.25 GHz, Q=40	13.5 @ 6 GHz, Q=30	14.9 @ 12 GHz, Q=20
In-band IP_{-1dB} (dBm)	-4.4	-25	-7	-26	-6.6	+5	+2.5	+1
Normalized DR (dB· Hz)[c]	159.6	145	144.8	102	152.4	167.5	163.5	160.1
OOB P_{-1dB} (dBm)	NA	-21	NA	NA	NA	16	15	15
OOB IIP_3 (dBm)	+29	5.5 - 8.7	NA	NA	NA	20	23	23
Power Consumption (mW)	21.4	50	60	43.2	17	43 - 66	40 - 66	30 - 70
Die area (mm^2)	1	2.1	6.44	0.15[d]	0.81	0.47	0.39	0.35
FOM (dB)	287.7	267.2	263.9	224.7	277.9	294.4	291.8	289.9

a: Voltage gain, b: Buffer noise is not included, c: Calculated from 174+IP_{-1dB}-NF, d: Active area

For example, at fc=3.25 GHz, when Q=20, typical in-band blocker P_{-1dB} power ranges 1~5 dBm. OOB blocker P_{-1dB} power at Δf=100 MHz is ~6 dBm and increases linearly as Δf increases until it reaches to ~15 dBm of saturation beyond Δf=300 MHz. Similarly, for the two-tone test, when Δf is smaller than 3-dB bandwidth, the in-band IIP3 is 6-15 dBm and increases in a linear fashion as Δf increases until it saturates to 23.5 dBm OOB IIP3 at Δf=150 MHz [CICC].

Table II summarizes the measured filter performance at three different bands and compares proposed filter parameters with the state of the art prior works. A Figure of Merit (FOM) is defined based on the important performance characteristics of a filter.

$$FOM = \frac{N \cdot DR \cdot f_{center} \cdot Q_{filter}}{P_{dc}}$$

Where N is order of the filter, DR is the Dynamic range, f_{center} is the filter center frequency and P_{dc} is the dc power dissipation. As it is shown in Table II, this work has the highest tuning range with higher FOM among Si based filters.

2.7 Summary

This chapter presents Q-enhancement LC bandpass filter in 0.13 µm SiGe BiCMOS technology. Varactor is used to achieve 2:1 frequency tuning, and varactor nonlinearity is characterized and improved using proposed DVI control and gain peaking with dynamic negative resistance. Three

chips at 2.25-4.5 GHz, 4-8 GHz, and 8-16 GHz are fabricated to test the functionality of the proposed techniques. Measurement results show wide turning range with independent Q control over the overall frequency range is achieved. The proposed LC filter employs voltage-mode (low-gain) and current-mode (high-gain) drivers for more flexible operation in the noise and linearity tradeoff space. These result in exceptional level of 150~170 dB·Hz of normalized filter dynamic range when Q varies from 10 to 100, one of the best performances compared with previous state-of-the-art Q-enhanced LC filter designs. Chapter 3 utilizes the proposed Q-enhanced BPF to synthesize the notch filter.

Chapter 3 : Integrated Tunable Synthetic Active Band-Stop Filters for Blocker Rejection at RF and Microwave Frequency Bands

3.1 Introduction

Containing interference is ever challenging task in wideband or multiband wireless systems. The interference environment becomes more hostile and more dynamic as the coexistence, collocation, or cooperation of multiple wireless devices over wide or varying frequency bands becomes the norm in current heterogeneous wireless network operations [1]. The rejection of a strong out-of-band blocker at the earliest possible stage in a receiver chain is critical to prevent the wireless systems from being saturated by the blocker. However, as illustrated in Figure 1.1, in wideband or multiband systems the blocker rejection by the front-end off-chip band-pass filter (BPF) would be limited due to inherent complex tradeoffs amongst bandwidth, selectivity, loss, and distortion in typical passive filters [30][31]. Therefore, it will be highly desirable to integrate a frequency agile and bandwidth tunable band-stop filter (BSF) in the RF front-end receiver path to provide more blocker suppression adaptive to the dynamic interference environment in broadband system operations [32]-[39].

Traditionally, notch filters implemented with tunable passive resonators on printed circuit boards are often used to mitigate the interference issue [32], [33]. In pure passive notch filters, however, because of the limited Q of passive components multiple LC-resonance sections need to be cascaded progressively in accordance with the increase of selectivity. This often results in a large passband loss while claiming a bulky space, a suboptimal design for on-chip integration in integrated circuit (IC) technology. Recently, notch filters with Q-enhanced series LC resonators have been integrated in the low-noise amplifiers (LNAs) signal paths in [3],[35]-[37].

In the Q-enhancement band-stop filters, a negative resistance based on active positive feedback is often used to compensate for the finite resistive loss of the passive LC resonators, hence to achieve a high degree of notch selectivity. By centering the resonance frequency to the interference band, the blocker can be rejected effectively. However, the notch attenuation will be strongly traded with the filtering bandwidth: larger stop-band rejection needs higher filter Q which in turn sacrifices the operational bandwidth. In order to combat with the blocker more effectively under dynamic blocker environments, it needs to be able to control the notch rejection and bandwidth independently.

In this chapter, we propose an active notch filter system comprised of a Q-enhancement band-pass filter (BPF) and an all-pass amplifier [2]. The notch response will be synthesized by subtracting the BPF output from the all-pass output. In the proposed synthetic notch filters, the BPF is responsible for defining selectivity while stop-band attenuation is primarily dependent on the gain matching between the BPF and the all-pass amplifier. Therefore, notch attenuation will be controllable independently from bandwidth tuning, providing more operational flexibility. Further, the filter dynamic range can be optimized in the all-pass amplifier independently from the selectivity control in the BPF, resolving entrenched tradeoff between selectivity and dynamic range in active filters. For proof of concept designs, three synthetic notch filters are implemented for S-band (2-4 GHz), C-band (4-8 GHz), and X-Ku bands (8-16 GHz) operations with 2:1 frequency tuning range in 0.13-μm SiGe BiCMOS technology. More details on the synthetic notch filter system are described in section 3.2. Section 3.3 discusses circuit designs of the filter building blocks and experiment results are shown in section 3.4.

3.2 Synthetic Band-Stop Filter System

Figure 3.1 shows the block diagram of the proposed band-stop filter, synthesizing a notch response at ③ by subtracting a 2nd–order BPF output (①) and a wideband amplifier output (②) acting as an all-pass filter (APF) at the operational band of interest. After the synthesis, pass-band signal quality, noise figure (NF), and linearity, are dictated by the all-pass amplifier that determines the filter dynamic range.

3.2.1 Phase Matching & Notch Frequency

In the synthetic notch filter, the gain mismatch between the BPF and APF paths can be nullified by controlling the variable gain amplifier (VGA) gain. Suppose the phase responses between the AP and BP paths are matched, then the notch frequency (ω_N) will be the same as the BPF LC resonance frequency (ω_o). However, typically there would exist a phase mismatch ($\Delta\varphi$) between the VGA and AP amplifier. The LC resonator translates the phase mismatch into a notch frequency drift and the notch frequency shift ($\Delta\omega_N$) from ω_o is a function of $\Delta\varphi$ and LC resonator quality factor (Q). To investigate the notch frequency error, frequency responses of the BP and AP paths are modeled as (1) and (2), respectively.

$$T_{BP}(s) = \frac{G_{BP} \cdot \frac{\omega_o}{Q} s}{\left(1 + \frac{s}{\omega_{p,VGA}}\right)\left(s^2 + \frac{\omega_o}{Q} s + {\omega_o}^2\right)}. \quad (1)$$

$$T_{AP}(s) = \frac{G_{AP}}{1 + s/\omega_{p,AP}}. \quad (2)$$

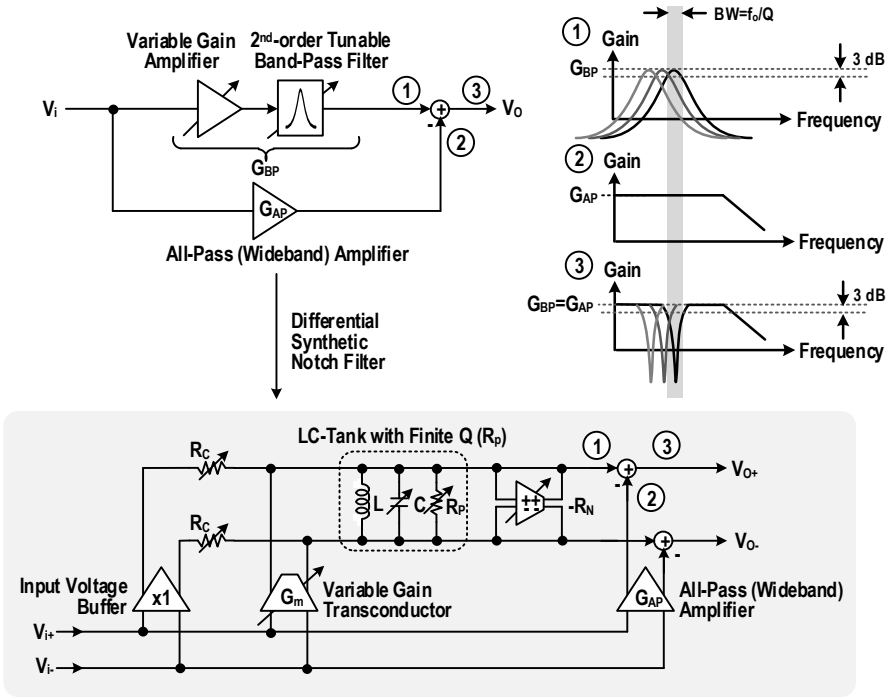

Figure 3.1: Integrated active band-stop filter system to synthesize tunable frequency and tunable bandwidth notch filtering based on the all-pass (wideband) buffer amplifier and 2nd-order Q-enhanced band-pass filter.

The amplifiers are modeled as an one-pole system, and $\omega_{p,VGA}$ and $\omega_{p,AP}$ represent the bandwidth (BW) of the VGA and AP amplifier, respectively. The phase responses of the transfer functions are

$$\angle T_{BP}(j\omega) = \frac{\pi}{2} - \tan^{-1}\left(\frac{\omega}{\omega_{p,VGA}}\right) - \tan^{-1}\left(\frac{\omega_o}{Q}\frac{\omega}{{\omega_o}^2-\omega^2}\right) \quad (3)$$

and

$$\angle T_{AP}(j\omega) = -\tan^{-1}\left(\frac{\omega}{\omega_{p,AP}}\right). \quad (4)$$

Assuming the gain mismatch between the AP and BP paths is negligible, the maximum stopband attenuation will occur when the phases are exactly matched, i.e.$\angle T_{BP}(j\omega) = \angle T_{AP}(j\omega)$ at $\omega = \omega_N$. Therefore, from (3) and (4)

$$\Delta\varphi = \tan^{-1}\left(\frac{\omega_N}{\omega_{p,VGA}}\right) - \tan^{-1}\left(\frac{\omega_N}{\omega_{p,AP}}\right) = \frac{\pi}{2} - \tan^{-1}\left(\frac{\omega_o}{Q}\frac{\omega_N}{{\omega_o}^2-{\omega_N}^2}\right). \quad (5)$$

By setting $\omega_N = \omega_o + \Delta\omega_N$,

$$\Delta\varphi = \frac{\pi}{2} - \tan^{-1}\left(\frac{1}{Q}\frac{1+\frac{\Delta\omega_N}{\omega_o}}{1-\left(1+\frac{\Delta\omega_N}{\omega_o}\right)^2}\right). \quad (6)$$

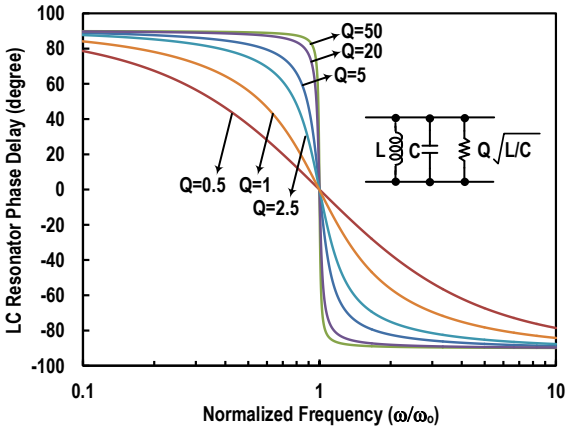

Figure 3.2: Phase response in 2nd-order LC resonator.

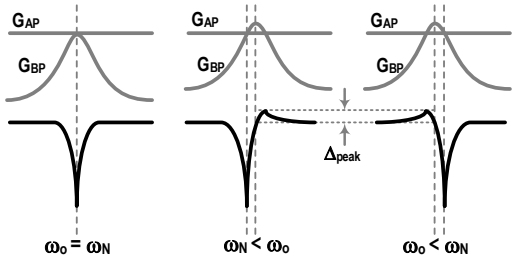

(a) (b) (c)

Figure 3.3. Notch frequency shift accompanying amplitude peaking Δ_{peak}: (a) ideal notch response when $\Delta\varphi = 0$, (b) when $\Delta\varphi > 0$, and (c) when $\Delta\varphi < 0$.

Suppose $\Delta\varphi$ would be a small mismatch allowing the premise of $\Delta\omega_N/\omega_o \ll 1$, then (6) can be approximated as

$$\Delta\varphi = \tan^{-1}\left(Q\frac{1-\left(1+\frac{\Delta\omega_N}{\omega_o}\right)^2}{1+\frac{\Delta\omega_N}{\omega_o}}\right) \cong -\frac{2Q}{\omega_o}\Delta\omega_N. \quad (7)$$

Consequently, the notch frequency is

$$\omega_N = \omega_o + \Delta\omega_N \cong \omega_o\left(1-\frac{\Delta\varphi}{2Q}\right). \quad (8)$$

Exemplarily, if Q=30 and $\Delta\varphi$=5° then $|\Delta\omega_N/\omega_o|$=5°/360°×2π/60=1.45×10^{-3} ($\Delta\omega_N$~0.15% ω_o). The frequency error $\Delta\omega_N$ is inversely proportional to the filter selectivity (Q). This is because higher Q in LC-resonator causes steeper phase change around the resonance frequency as illustrated in Figure 3.2, which requires a smaller frequency offset from ω_o to compensate for the phase error caused by the mismatch between the VGA and all-pass amplifier. In principle, the extreme phase mismatch between the 1st-order amplifiers would be ±90°. Since the maximum amount of phase deviation in the 2nd-order LC resonator is ±90° across resonance, the LC tank is

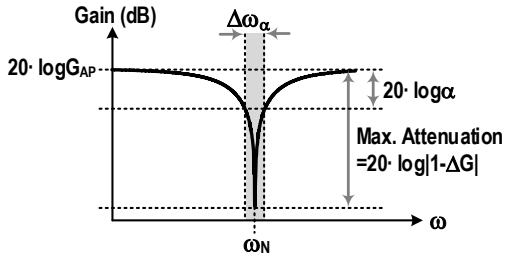

Figure 3.4: Characterization of notch response: notch frequency (ω_N), maximum notch attenuation ($20\cdot\log|1-\Delta G|$), and attenuation bandwidth resulting in α dB rejection from the passband ($\Delta\omega_\alpha$).

capable of accommodating the phase mismatch and converting it to a notch frequency error.

When the phases are heavily mismatched, $\Delta\varphi$ would not only cause the notch frequency shift but also induce an amplitude peaking, Δ_{peak}, in the vicinity of the passband edge, as illustrated in Figure 3.3. The peaking is an implication of the pole of the LC resonator. In practical implementations, the VGA and all-pass amplifier can be designed such that the phase delay can be matched by configuring them with the same topology having a large bandwidth. Thus, the impact of the phase mismatch on the notch frequency shift in (8) could be minimized, resulting in $\omega_N \approx \omega_o$ and no discernible peaking is observed in this work.

3.2.2 Gain Matching & Notch Attenuation

In the differential implementation in Figure 3.1, the passband 3-dB bandwidth can be set independently by changing the LCR filter Q, whereas notch attenuation can be controlled by adjusting the VGA gain, free from the tradeoff between bandwidth and notch attenuation. The VGA function is realized by a variable gain transconductor (g_m) that drives the LCR BPF in current mode. R_p represents a finite frequency-dependent LC-tank loss. A higher BPF Q than the intrinsic LC tank Q ($= R_P/\sqrt{L/C}$) is achievable with compensating the tank loss by a negative resistance ($-R_N$) realized with the active positive feedback circuit. Also the filter Q can be lower than the native LC-tank Q by disabling the negative resistance and by decreasing R_C. In the differential notch filter, the BPF is also driven by a voltage buffer to minimize signal loss when R_C approaches to its minimum, assisting the VGA in driving the BPF when load becomes heavier.

By neglecting the buffer and transconductor output impedances, overall BPF gain can be expressed as

$$G_{BP} = \underbrace{\frac{R_P R_N}{R_C(R_N - R_P) + R_P R_N}}_{\text{Voltage-mode gain}} + \underbrace{G_m \frac{R_P R_N R_C}{R_C(R_N - R_P) + R_P R_N}}_{\text{Current-mode gain}}$$

$$= \frac{R_P R_N (G_m R_C + 1)}{R_C (R_N - R_P) + R_P R_N} . \quad (9)$$

In (9), the minimum gain is 0 dB when R_C=0 Ω because the input buffer still delivers RF input to the LC tank. In reality, $R_C > 0$ Ω due to a finite output resistance of the buffer and gain is always greater than 0 dB. Thus, the complementary driving by the VGA in current mode and by the input buffer in voltage mode enables a wide range of Q control with no signal loss.

Once the phase is matched at ω_N and applying a small phase mismatch approximation (i.e. $\omega_N \approx \omega_o$), then the maximum notch attenuation from the all-pass gain will be mainly limited by the gain mismatch ($\Delta G = G_{BP}/G_{AP}$) between the BP and AP paths. The maximum notch attenuation will be given as

$$\begin{aligned} \text{Max. Attenuation} &= 20 \cdot \log \left| 1 - \frac{T_{BP}(\omega_N)}{T_{AP}(\omega_N)} \right| \\ &\approx 20 \cdot \log \left| 1 - \frac{G_{BP}}{G_{AP}} \left(1 + jQ \left(\frac{\omega_N}{\omega_o} - \frac{\omega_o}{\omega_N} \right) \right)^{-1} \right| \\ &\approx 20 \cdot \log \left| 1 - \frac{G_{BP}}{G_{AP}} \right| . \end{aligned} \quad (10)$$

Less than 10% gain mismatch leads to better than 20 dB rejection. In actual implementations, the band-stop system can achieve a high level of notch rejection (> 50 dB) with a fine adjustment of the VGA gain, as can be seen in section 3.4.

The maximum attenuation is attainable only at a single frequency while the blocker could be a band-limited signal. Thus, of more practical interest is the frequency band around the notch center that gives a particular attenuation level. In a well matched design ($\omega_N \approx \omega_o$), the α-dB attenuation bandwidth where signal is attenuated by α dB from the passband gain, $\Delta\omega_a$ as illustrated in Figure 3.4, will be determined by

$$\begin{aligned} 20 \cdot \log \left| \frac{s^2 + \frac{\omega_o}{Q} s(1 - \Delta G) + {\omega_o}^2}{s^2 + \frac{\omega_o}{Q} s + {\omega_o}^2} \right|_{s = j(\omega_o + \Delta\omega_a/2)} \\ = -\alpha \text{ (dB)} \end{aligned} \quad (11)$$

, resulting in

$$\Delta\omega_\alpha \cong \frac{\omega_o}{Q} \sqrt{\frac{10^{-\frac{\alpha}{10}} - (1 - \Delta G)^2}{1 - 10^{-\frac{\alpha}{10}}}} . \quad (12)$$

where ω_o/Q is 3-dB attenuation bandwidth and the square root term represents a fractional bandwidth. The 3-dB rejection bandwidth, $\Delta\omega_{3dB}$, is the same as the BPF BW (ω_o/Q) as

expected, and 20-dB rejection bandwidth ($\Delta\omega_{20dB}$) is 10% $\Delta\omega_{3dB}$ ($0.1\cdot \omega_o/Q$).

3. 3 Circuit Design

Schematic details of the band-stop filter are shown in Figure 3.5 where conceptual diagrams of out-of-band blocker rejection are also illustrated.

3.3.1 Q-Enhanced Tunable 2nd-order Band-Pass Filter

In the BPF path, the emitter-follower (EF) $Q_{1,2}$ buffers input signal and drives main LCR BPF section in voltage mode while the emitter-degenerated transconductor consisted of $Q_{3,4}$ and variable R_G drives the passive network in current mode, incorporating gain controllability into the BPF. R_C, L, C, and the cross-coupled negative resistance cell composed of $Q_{5\text{-}8}$, R_X (200 Ω) and R_Y (10-400 Ω), comprise a tunable Q-enhanced 2nd-order BPF. The design values of the BPF passive components at each frequency band are summarized in TABLE I. The varactor tuning ratio is greater than 4:1 to ensure 2:1 frequency coverage with a margin under the existence of static parasitic layout capacitance that narrows frequency tuning range. In this work, 250~300 fF of layout parasitic is characterized with post-layout parasitic extraction including electromagnetic wave simulation using Sonnet Software, version 13.54.

In TABLE I, it is noteworthy that the inductances and capacitances are chosen so as for the characteristic impedance of the LC tank, $Z_o=\sqrt{(L/C)}$, to be a small impedance. A lower Z_o requires relatively smaller resistance to achieve a high filter Q (Q_F); for instance, if Z_o=10 Ω then 500 Ω would be necessary to achieve Q_F=50 , whereas 5 kΩ would be needed to attain the same Q if Z_o=100 Ω. The lower resistance demands smaller negative resistance, which in turn generates less noise with lower nonlinear harmonic distortion from the negative resistance cell, increasing the BPF dynamic range (DR). However, too small Z_o makes the LC tank vulnerable to a high loss due to smaller inductor Q for a given frequency, necessitating larger negative resistance and degrading the BPF DR. Therefore, for a given frequency and process technology, there should be optimum Z_o for a high dynamic range in the BPF.

In the proposed notch system the BPF is utilized to pass out-of-band interference, not signal, which will be nullified at the final output; thus in first order, the noise and nonlinearity from the negative resistance cell will not cause performance degradation to the final notch filter passband output. However, the edge of the passband is still vulnerable to the noise and nonlinearity of the BPF. Thus, a high dynamic range from the BPF is still desirable to prevent signal quality degradation when the blocker approaches adjacent to the signal band.

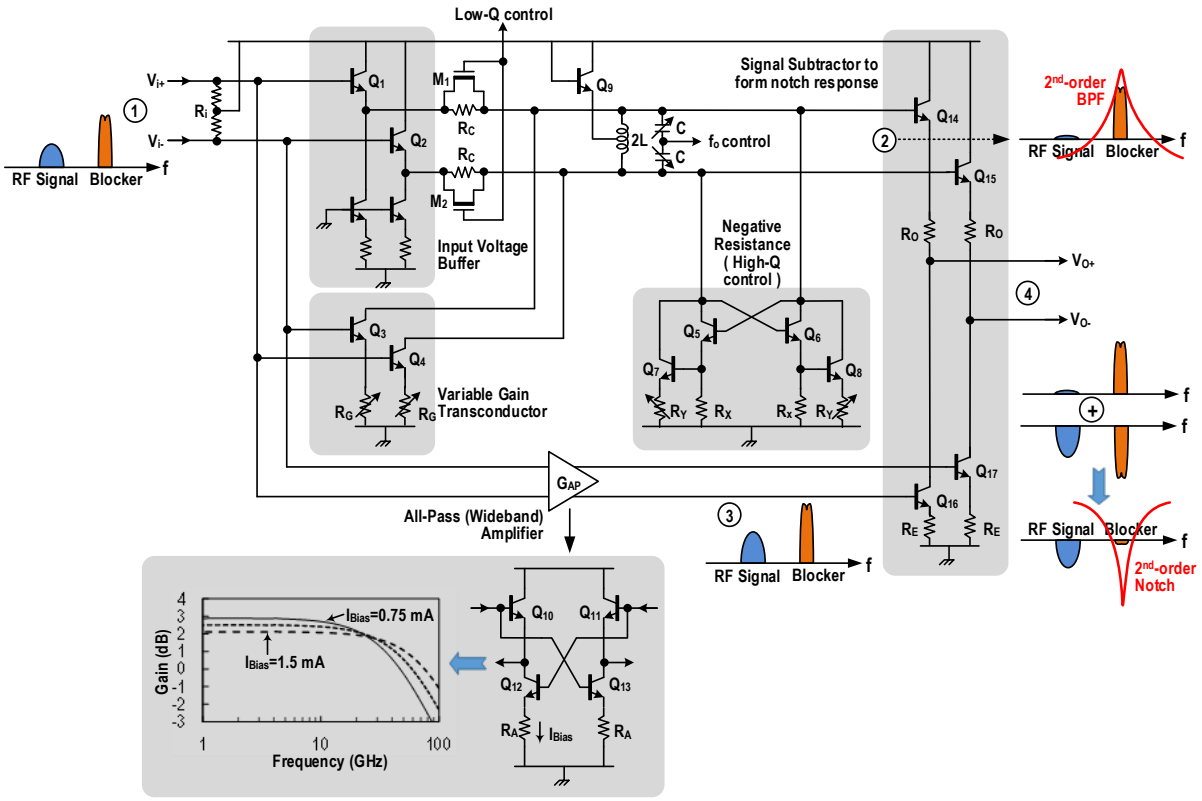

Figure 3.5: Schematic of the band-stop filter composed of paralleled 2nd-order BPF and an all-pass wideband buffer amplifier (simulated gain response of the wideband amplifier and conceptual diagrams for out-of-band blocker rejection are also shown together).

TABLE I. LCR BPF component design values

Frequency (GHz)	L (pH)	C (pF)	R_C (Ω)	$Z_o=\sqrt{(L/C)}$ (Ω)
2.25 ~ 4.5	832	1.3 ~ 6.1	10 ~ 350	12 ~ 25
4 ~ 8	325	1 ~ 4.2	10 ~ 350	9 ~ 18
8 ~ 16	125	0.7 ~ 3	10 ~ 350	6.5 ~ 13

The variable R_C is implemented with a parallel of linear R and NMOS ($M_{1,2}$). The NMOS operates always in deep-triode mode since Q_1 and Q_9 regulate supply voltage and set an equal bias voltage ($=V_{CC}-V_{BE,on}$) across R_C. The diode Q_9 also establishes bias voltage for the varactors (C) to be controlled at the common-mode node. The varactors are implemented using accumulation-mode NMOS, NMOS in n-well structure, to have a wide varactance tuning range (> 4x) with a high varactor Q compared with inversion-mode varactors [15]. The negative resistance can be expressed as

$$-R_N = -R_X \parallel \left(\frac{1}{g_{m7,8}} + R_Y\right) \qquad (13)$$

of which range is roughly -360 ~ -60 Ω. Then, overall filter Q (Q_F) can be given as

$$Q_F = \frac{\left(R_C + \frac{1}{g_{m1,2}}\right) \parallel R_P \parallel (-R_N)}{Z_O}$$

,where $$R_P = Q_T Z_O = Q_T \sqrt{L/C}. \quad (14)$$

Q_T is the intrinsic LC tank Q that ranges 12~29 depending on operation frequency. By controlling R_C, Q_F can be controlled from smaller than 5 to ~50; the smallest Q_F is set by the lowest R_C in series with $1/g_{m1,2}$ (~15 Ω) of $Q_{1,2}$. By utilizing the negative resistance and controlling R_Y, the filter Q can be increased further to 100 over 2-16 GHz with maintaining circuit stability (stability factor K>1) in simulations.

Note that the direct control of R_X will cause a different Miller effect of C_{be} from $Q_{5,6}$ to the LC tank, causing a frequency error depending on the Q control. In the negative resistance cell, $Q_{5,6}$ provides a fixed $-R_x$ and isolates the variable transconductor consisted of $Q_{7,8}$ and R_Y from the LC tank. So, changing R_Y, hence changing filter Q, will cause minimal center frequency shift. The negative resistance cell consumes 3-5 mA depending on the Q control. Input emitter-follower consumes 3 mA and the variable gain stage takes 0.6-9 mA from 3.3 V supply voltage depending on the gain settings.

3.3.2 All-Pass (Wideband) Amplifier

The wideband amplifier is designed with an NPN-based push-pull driver composed of $Q_{10\text{-}13}$ and R_A to get 2~3 dB signal gain. The gain is relatively small to increase signal bandwidth. The complementary driving by the common-emitter (CE) stage reduces the EF output impedance below 50 Ω differentially with a relatively small dc current of ~0.75 mA per differential path, achieving 45-50 GHz bandwidth in the presence of ~80 fF of output parasitic node capacitance. The bandwidth can be increased to ~100 GHz by increasing the bias current to ~1.5 mA. The transistor sizing and biasing of the amplifier are matched with those of the input BPF buffer for a phase matching. The large bandwidth is also beneficial to minimally delay the phase hence to minimize phase mismatch between the band-pass and all-pass paths. Input impedance matching is set by the resistor termination, R_i=50 Ω, mainly for interface with measurement equipment. The noise factor (F) of the filter with the input resistor termination is

$$F = 1 + \frac{R_s}{R_i} + \left(1 + \frac{R_s}{R_i}\right)^2 \frac{\overline{v_n^2}}{4kTR_s}$$

$$= \begin{cases} 2 + \dfrac{\overline{v_n^2}}{kTR_s}, if\ R_s = R_i \\ 1 + \dfrac{\overline{v_n^2}}{4kTR_s}, if\ R_s \ll R_i \end{cases} . (15)$$

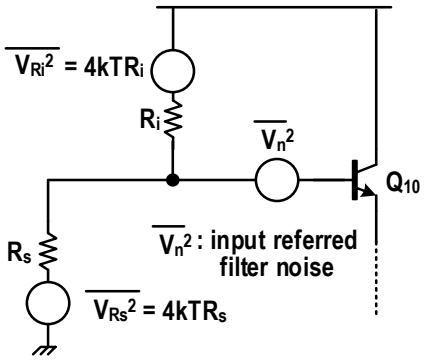

Figure 3.6: Equivalent noises at the input of the band-stop filter.

,where $\overline{v_n}$ is equivalent input referred noise voltage, which is dominated by the noise of the all-pass amplifier and signal subtractor (Figure 3.6). The simulated $\overline{v_n}$ of the amplifier is ~1.5 nV/$\sqrt{Hz}$, resulting in 11-11.5 dB NF with 50-Ω matching at 4-8 GHz. For on-chip system integration, the 50-Ω matching is not necessary, and R_i can be set to an arbitrary large value much greater than the source resistance, only for biasing. In such condition, the NF will be dropped to 5-6 dB which can easily be suppressed by a proceeding LNA gain.

3.3.3 Notch Synthesis

As sketched in Figure 3.5, if a strong out-of-band blocker coexists nearby RF signal band (①), then the blocker will be band-passed through the BPF branch (②) and buffered to the final output by $Q_{14,15}$. R_o (15 Ω) in series with the EF output impedance forms a wideband output matching impedance. Meanwhile, the signal and blocker will also be passed through the all-pass section (③) and subsequently inverted by $Q_{16,17}$. Finally by adding the two outcome signal sets, the interference can be rejected effectively, shaping a 2nd-order notch filtering in the interference band at the final output (④). The CE stage is degenerated with R_E (10 Ω) for better linearity with less loading capacitance to the proceeding amplifier stage, which improves bandwidth as well. The output stage consumes 5 mA per each differential path. Overall simulated pass-band gain at the final output with 50-Ω loading is 0~1 dB.

Since the BPF section is isolated by emitter-followers from the input and output, the bandwidth control or frequency tuning in the BPF does not alter the impedance matching performance. The simulated NF is 11.7~13.4 dB and IP_{-1dB} is -3~-4 dBm at the expense of 69-103 mW at 2-4 GHz. At 4-8 GHz, the simulated NF is 11.2~12.5 dB and IP_{-1dB} is -1~0 dBm with 60-91 mW power dissipation. At 8-16 GHz, NF=14~15 dB and IP_{-1dB}=0~3 dBm with 70-90 mW dc power consumption under the input matched to 50 Ω.

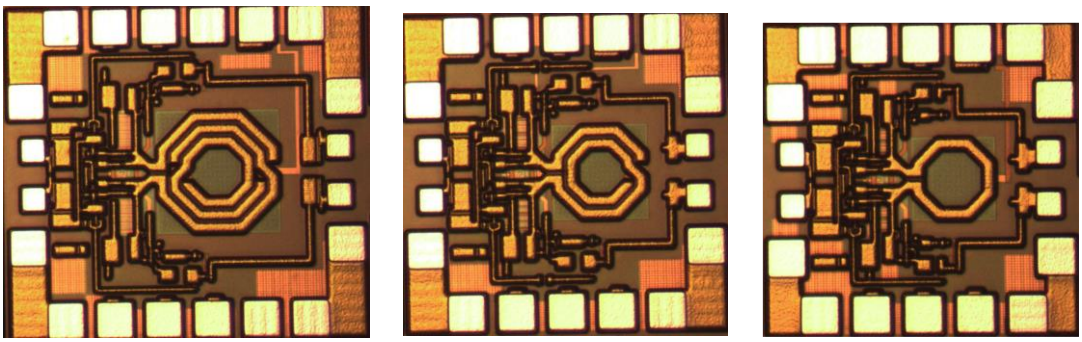

Figure 3.7: Band-stop filter chip photographs: (a) 2-4 GHz (size: 0.68×0.72 mm^2), (b) 4-8GHz (size: 0.63×0.63 mm^2), and (c) 8-16 GHz (size: 0.62×0.57 mm^2).

3.4 Experimental Results

Three notch filters with each filter covering an octave bandwidth from 2 GHz to 16 GHz are implemented in 0.13 μm SiGe BiCMOS process (1P7M, f_T/f_{max}=180/220 GHz). The chip photographs are shown in Figure 3.7. Since the filters are pseudo-differential, highly symmetric layouts are striven for differential matching. The band-pass filter sections of the notch filters are also implemented to characterize Q of the filter separately.

The silicon chips are measured after differential SOLT calibration with GSSG probes (calibration step: ~3 MHz). 180-degree hybrid couplers are used at the input and output, respectively, for single-ended interface with measurement equipment. The BPF measurements confirm that the filter Q can be increased from less than 5 up to 100 over the entire frequency band by controlling the R_C and R_Y in Figure 3.5 with stable circuit operation (K-factor > 1). However, when Q increases over 60 the BPF gain becomes too large to be matched with the all-pass gain. Thus, in the measurement BPF Q is limited to 60 for all frequencies. For 2-4 GHz design, the measured DC current ranges 20-30 mA from 3.45 V supply voltage, depending on the Q control. For 4-8 GHz filter, the DC current is 20-27.6 mA from 3.3 V supply voltage. For 8-16 GHz filter, the DC current is 21-30mA from 3.3 V supply voltage.

With varactor control, 2:1 continuous frequency tuning is achieved for all S-band, C-band, and X-Ku band BSFs. Figure 3.8 (a), (b), and (c) show measured notch frequency tuning characteristics with 0.25 GHz and 0.5 GHz step for the S-band, C-band, and X-Ku-band designs, respectively, and corresponding BPF responses are also superimposed with dot lines. In this case, the BPF gains are adjusted to obtain -50 dB of attenuation with 0~1 dB of pass-band gain for all measured frequencies. Note that actual on-chip system integration, the input and output 50-Ω

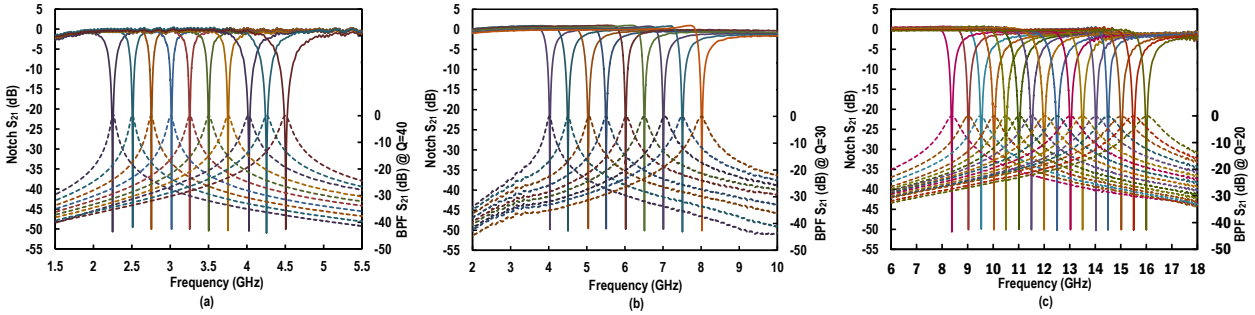

Figure 3.8: Measured band-stop filter responses (solid lines): (a) 2.25-4.5 GHz (step: 0.25 GHz), (b) 4-8 GHz (step: 0.5 GHz), (c) 8-16 GHz (step: 0.5 GHz). For all cases, corresponding measured band-pass filter responses are superimposed (dot lines).

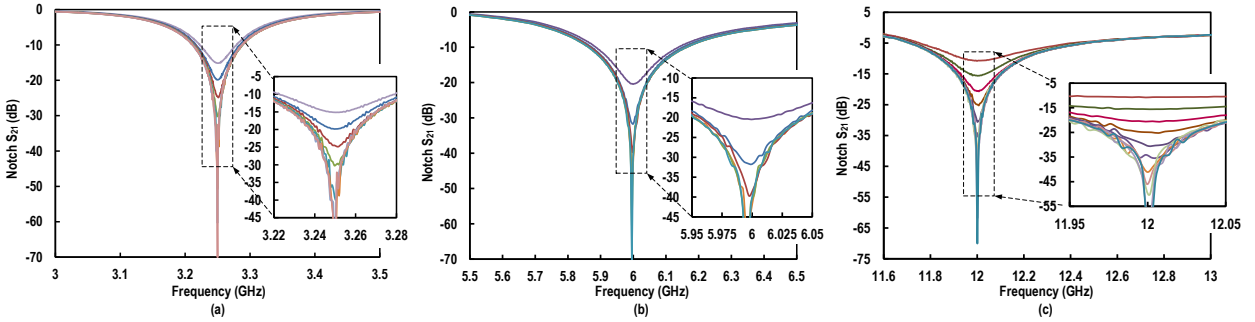

Figure 3.9: Measured notch depth tuning characteristics: (a) at 3.25 GHz of notch frequency (BPF Q=15, subplot: zoomed-in view 3.25 GHz ± 30 MHz window), (b) at 6 GHz of notch frequency (BPF Q=10, subplot: zoomed-in view within 6 GHz ± 50 MHz window), and (c) at 12 GHz of notch frequency (BPF Q=10, subplot: zoomed-in view within 12 GHz ± 50 MHz window).

termination may not be necessary. Then without 50-Ω matching loss, filter voltage gain could be 12 dB higher than the measurement. By tuning the BPF gain control voltage with finer resolution (~ 1's mV order) maximum 70 dB of stop-band attenuation can be achievable for all notch filters (Figure 3.9).

By changing BPF Q, the bandwidth of the notch output can be controlled. Figure 3.10 displays measured notch responses with different BPF Q settings. For all cases the filters can maintain -50 dB attenuation, corresponding to < 0.5% gain mismatch and demonstrating that the bandwidth can be adjustable without compromising the notch attenuation. Also, the notch center frequency shift during the Q control is trivial, mainly because of the isolation of Q tuning element from the resonator in the Darlington-pair negative g_m-cell, as discussed in the design section. In Figure 3.10, when Q=30 the -20 dB rejection bandwidth, $\Delta\omega_{20dB}$, is 7.4 MHz at f_N=2.25 GHz, 22 MHz at f_N=6 GHz, and 40 MHz at f_N=12 GHz, which is 10% of BPF 3-dB BW for each case and well

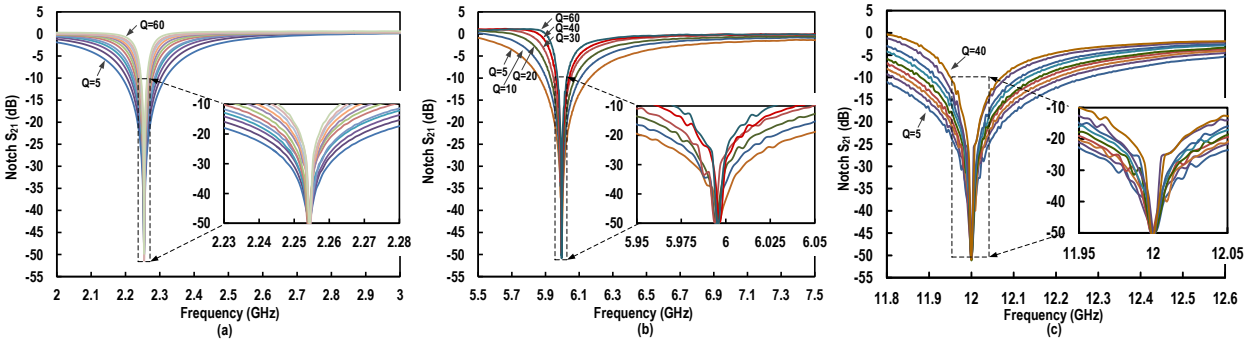

Figure 3.10: Measured bandwidth (Q) tuning characteristics for several cases of BPF Q: (a) at 2.25 GHz of notch frequency (subplot: zoomed-in view 2.25 GHz ± 25 MHz window), (b) at 6 GHz of notch frequency (subplot: zoomed-in view within 6 GHz ± 50 MHz window), and (b) at 12 GHz of notch frequency (subplot: zoomed-in view within 12 GHz ± 50 MHz window).

matched with the theoretical estimation based on (12).

The measured typical NF and IP_{-1dB} performances for 4-8 GHz filter are shown in Figure 3.11. The notch center frequency is tuned to 8 GHz (BPF Q=30) and passband NF and IP_{-1dB} are measured. The measured NF is 8~10.8 dB and IP_{-1dB} is -8~-6 dBm, resulting in 155-160 dB·Hz of normalized dynamic range at the expense of 66 mW P_{diss}, which is in good agreement with simulation results. In the notch band the IP_{-1dB} decreases rapidly because of the nonlinearity of the Q-enhanced LC tanks [17]. The all-pass amplifier takes in charge of the overall filter dynamic range and thereby due to the active nature of the filter, the filter in-band linearity is a strong function of the dc power dissipation. This is illustrated in Figure 3.12 which displays passband IP_{-1dB} improvement as increasing dc power dissipation. The IP_{-1dB} is measured at 6 GHz as increasing supply voltage while the stopband center frequency is tuned at 8 GHz (BPF Q=30) with retaining 50 dB rejection for all cases. As can be seen, the IP_{-1dB} is -10 dBm with P_{dc}=60 mW (V_{CC}=3.25 V) and increases significantly up to around +6 dBm at the expense of P_{dc}=132 mW (V_{CC}=3.65 V). During the measurement, gain increases from 0 dB to ~2 dB as V_{CC} increases and is normalized to 0 dB for the sake of comparison in Figure 3.12.

An example of typical measured group delay response is shown in Figure 3.13 where f_N=4 GHz and BPF Q=30. Because of finite ~3MHz measurement frequency step, the differentiation of measured S_{21} phase creates noise-like delay response in the passband. However, average group delay is well matched with the simulation result. The measured average group delay variation is less than 20 ps from 5 GHz to 8 GHz and less than 4 ps for any given 1 GHz of instantaneous bandwidth within the passband from 6 GHz to 8 GHz. In the synthetic filters, the all-pass amplifier and bandpass filter will be compressed by different levels of input power. Generally

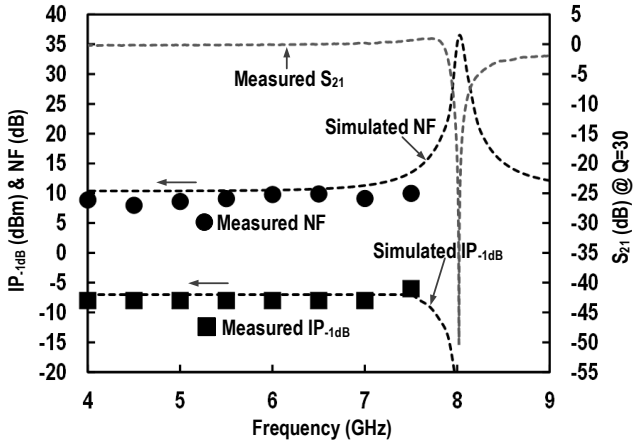

Figure 3.11: Typical measured pass-band NF and linearity performance of the 4-8 GHz notch filter (P_{diss}=66 mW). The notch frequency is set to 8 GHz.

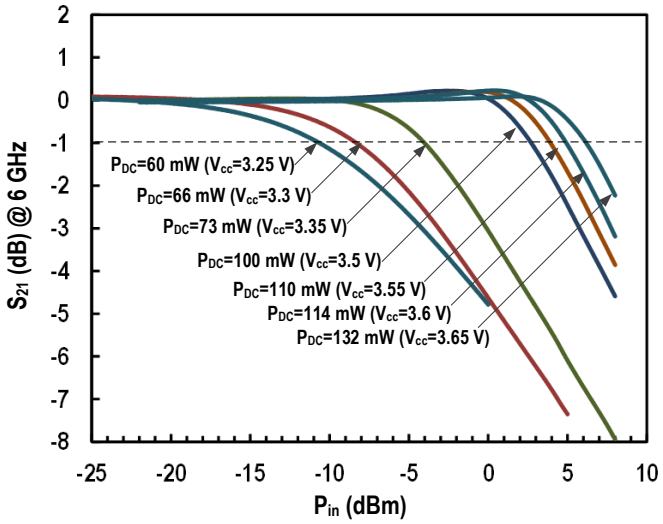

Figure 3.12: Measured gain compression behaviors at 6 GHz with different supply voltages under the 50 Ω loading, when notch center frequency is at 8 GHz (Q=30). Gain is normalized to 0 dB.

speaking, the BPF experiences more nonlinearity because it contains more nonlinear components such as active negative resistance and nonlinear varactor.

Thus, as illustrated in Figure 3.14 the gain of BPF will start to be compressed earlier than that of all-pass filter, causing a gain mismatch (ΔG_x) as the input blocker power (P_b) approaches the BPF gain compression point ($P_{-1dB,BP}$). This essentially degrades stopband attenuation. Figure 3.15 shows the measured degradation of notch rejection versus blocker input power at three different notch frequencies.

When f_N=f_b=8 GHz, the maximum notch rejection starts to decrease from 50 dB when P_b=-15

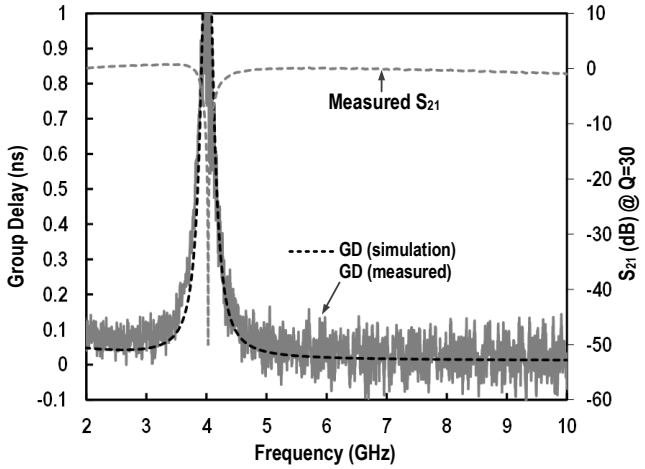

Figure 3.13: Measured group delay response of the C-band band-stop filter. Measured result is superimposed on the simulation result (notch frequency: 4 GHz, BPF Q=30).

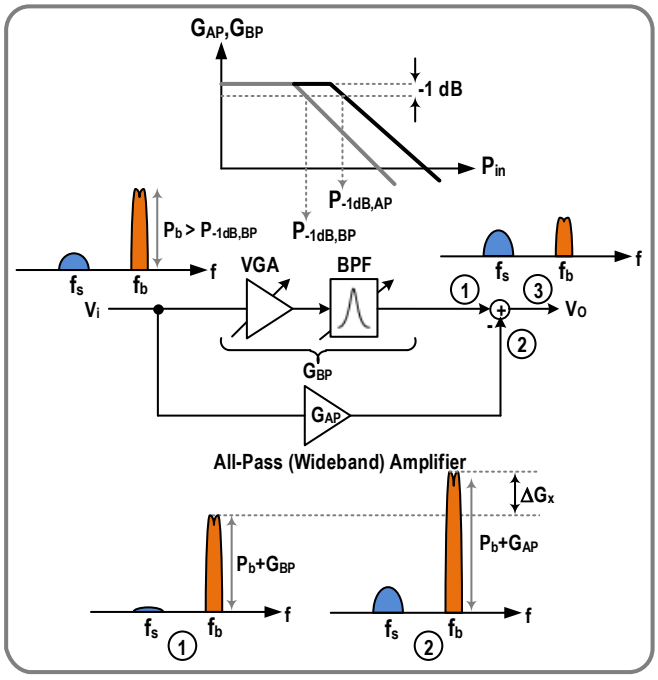

Figure 3.14: Illustration of degradation of notch rejection due to mismatch of gain compression points between the band-pass and all-pass paths.

dBm and tends to saturate to ~25 dB when the blocker power exceeds 0 dBm because the all-pass amplifier also becomes compressed and gain difference becomes constant. The trend is almost same for $f_N=f_b=4$ GHz and $f_N=f_b=6$ GHz. However, by increasing the BPF VGA gain, the gain mismatch led by the different gain compression characteristics can be compensated; for all cases in Figure 3.15, after recalibrating the BPF gain, the maximum notch rejection is restored to

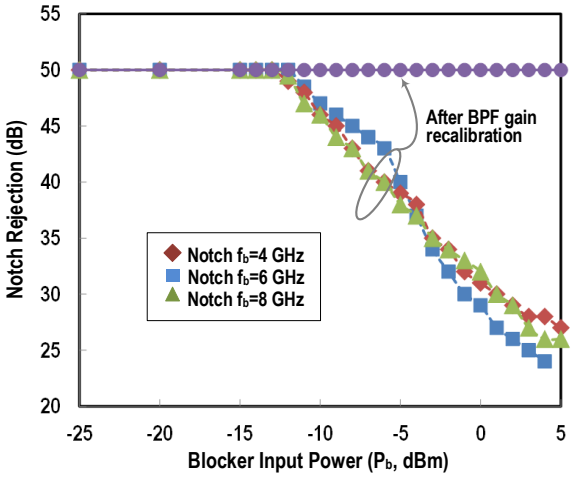

Figure 3.15: Degradation of notch rejection under large blocker input due to a nonlinearity mismatch between the BP and AP paths. For all cases, it can maintain ~50 dB notch rejection after the BPF gain recalibration (f_b and P_b are blocker frequency and blocker power in Figure 3.14).

TABLE II. PERFORMANCE SUMMARY AND COMPARISON

	[11]	[10]	[9]	[16]	This Work		
Type	N-Path Notch	Q-Enhanced LC Notch			Q-Enhanced LC + Synthetic Notch		
Process	65 nm CMOS	0.13 µm CMOS	0.13 µm CMOS	0.13 µm SiGe BiCMOS	0.13 µm SiGe BiCMOS		
Center Frequency (GHz)	0.1 ~ 1.2	4.7 ~ 5.4	5 ~ 6	11	2.25 ~ 4.5	4 ~ 8	8 ~ 16
20-dB Rejection Bandwidth, $\Delta\omega_{20dB}$, (MHz)	NA	NA	NA	NA	4 ~ 40 @ 2.25 GHz	10 ~ 100 @ 6 GHz	30 ~ 200 @ 12 GHz
Q Tuning	NO	NO	NO	NO	5 ~ 60	5 ~ 60	5 ~ 40
Pass-Band Gain (dB)	-1.4 ~ -2.8	19.4[b]	-0.8 ~ -2	22.5[b]	0 ~ 1	0 ~ 1	0 ~ 1
NF (dB)	1.6 ~ 2.5	3.5[b]	5[b]	5.1[b]	12 ~13[e] (6.6~7)[f]	8 ~10.8[e] (4.4~5)[f]	14 ~ 17[e] (8.2~11.1)[f]
Pass-Band IP_{-1dB} (dBm)	+6	-9.4[b]	-9[b]	-25	-2 ~ -1.5 @ 80 mW	-1 ~ +1 @ 85 mW	0 ~ +4 @ 84 mW
Normalized DR (dB·Hz)[a]	177.5	161.1[b]	160[b]	143.9[b]	160	162.2 ~ 167	157 ~ 164
Max Notch Rejection (dB)	21 ~ 24	44	44	70	70	70	70
Max Rejection with -5 dBm Blocker Power (dB)	24	3	15[c]	NA	33 / 50[d]	40 / 50[d]	38 / 50[d]
Power Consumption (mW)	3.5 ~ 30	7.5	32.5[b]	21	66 ~ 99	66 ~ 91	70 ~ 90
Die Area (mm^2)	0.87	1.6	1.6	1	0.48	0.39	0.35

a: calculated from 174+IP_{-1dB}-NF (dB), b: LNA + Filter, c: blocker power=-16 dBm, d: after BPF gain recalibration, e: with 50-Ω resistive input matching (without LNA), f: projected results without input 50 Ω matching.

50 dB, exhibiting resilience of the blocker rejection in the proposed synthetic filter to a strong interferer. In essence, the large signal handling capability of the filter is limited by the passband IP_{-1dB} of the all-pass amplifier.

The power dissipation in conventional Q-enhanced notch filters is low to moderate at microwave band but they severely suffer from limited tuning capability. In fact, power consumption, filter DR, and filter tuning (frequency and Q) range are strongly coupled by tradeoff relationship in the

Q-enhanced filters. The proposed synthetic notch filters trade dc power to achieve one of the most versatile filter re-configurability in center frequency and bandwidth tunings at microwave bands. Unlike the N-path filters or conventional Q-enhanced filters, the proposed notch filter has the pliancy of notch rejection to a strong blocker: the notch rejection at the input of -5 dBm blocker power is better than 33 dB for all measured frequency, which increases further to 50 dB by adjusting the VGA gain in the BPF in TABLE II.

3.4 Summary

This chapter presented synthetic notch filters comprised of a Q-enhanced band-pass filter and a wideband amplifier playing the role of an all-pass filter at the bands of interest. By subtracting the BPF output from the APF output, a notch response can be developed with stopband rejection primarily depending on the gain matching between the BPF and APF. The filter frequency selectivity will be set by the BPF and filter dynamic range will be determined by the all-pass amplifier independently, allowing a focused independent design optimization for dynamic range in the amplifier and selectivity in the BPF. Therefore, the synthetic filter can break the ingrained performance tradeoff between selectivity and dynamic range in the Q-enhancement LC filters. Also, the stop-band attenuation will no longer be traded with filter bandwidth. These tradeoff-free band-stop filters could allow tremendous operational versatility to suppress blockers more effectively under dynamically changing interference environments. Three notch filters with each filter covering an octave bandwidth from 2-to-16 GHz were implemented and characterized successfully in 0.13 μm SiGe BiCMOS technology, demonstrating a frequency scalability of the filters from RF to microwave frequencies.

Chapter 4 : CMOS Reconfigurable Band-Pass/ Band-Stop filters

4.1 Introduction

In this chapter, a reconfigurable band-pass/band-stop filter in 0.13 µm CMOS will be presented. To be more practical in receiver front-end an LNA is realized before a reconfigurable filter. Figure 4.1 shows the conceptual block diagram of the reconfigurable filter.

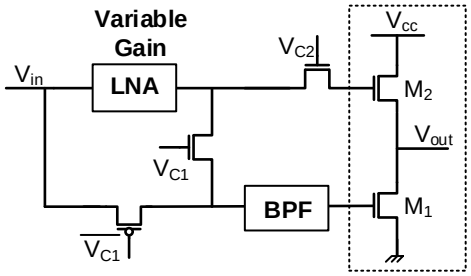

Figure 4.1: Block diagram of reconfigurable band-pass/ band-stop filter

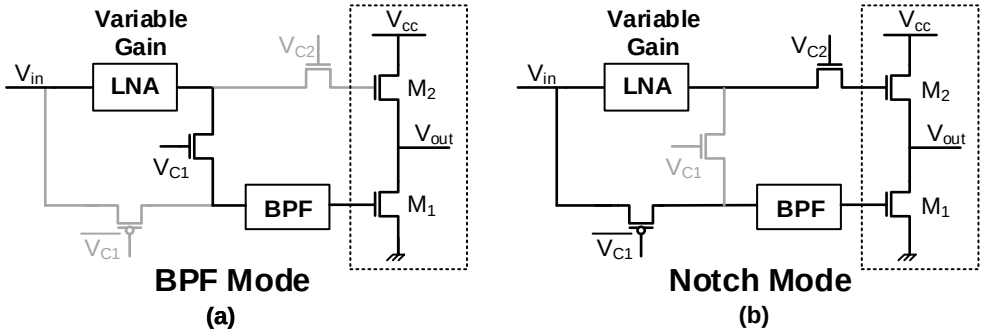

Figure 4.2: (a) Band-pass filter mode. (b) Band-stop filter mode.

In band-pass filter mode, Figure 4.2 (a), when V_{C1} is on, the complementary PMOS switch is off, therefore input signal transfers to the output through LNA, BPF, and M_1. It should be mentioned that when V_{C2} is off, M_2 only provides bias for M_1. In notch mode, in Figure 4.2 (b), V_{C1} is off, therefore complementary PMOS switch is on and V_{C2} is also on. So, two separate paths go through adder and notch is created at the output.

4.2 LNA Design

Since LNA comes after the antenna and off-chip preselect filter, in addition to high gain, it should have low noise characteristic. Therefore gm-boosted noise cancelling LNA is utilized for its high gain and low noise figure (NF). Figure 4.3 shows the schematic of gm-boosted, noise cancelling LNA. In g_m-boosted LNA, gate of M_1 is connected to –Vi and its source is connected

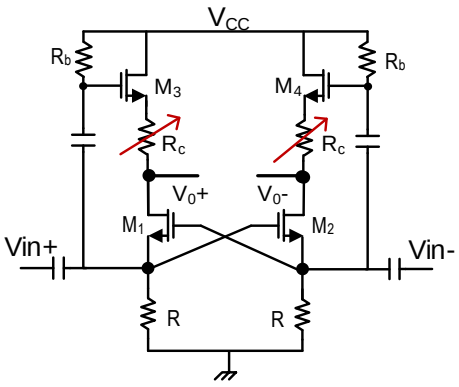

Figure 4.3: Schematic of gm-boosted noise cancelling LNA.

to $+V_i$, therefore $V_{gs}=2V_i$, and output current is $2g_m \cdot V_i$, so gm is doubled. However, the main problem with common gate LNA is noise. To reduce the noise, in Figure 4.3, M_3 is added to cancel the noise of M_1. If the channel thermal noise of M_1 is out of phase at the output and in phase at the input, the in phase noise passes through M_3 with the same phase, and is subtracted from the out of phase noise at the LNA output, and noise of M_1 is partially cancelled at the output.

LNA is matched to 50 Ω at the input to match with measurement instrument. However, matching is not needed at the output due to the high impedance driving with either BPF at band-pass mode or M_2 of adder in notch mode. Post layout simulation for LNA shows 2.9 dB NF and 16 dB of gain. The BPF in Figure 4.1 is the CMOS version of the BPF designed in chapter 2 (Figure 2.9) and optimized for this design.

4.3 Measurement Results

The mode reconfigurable Q-enhanced LC filter is implemented in 0.13μm CMOS process (f_T=90GHz) and measured through on-wafer testing after standard differential SOLT calibration. Chip micrograph is shown in Figure 4.4 (a). With the varactor tuning, the filter f_c can be controllable continuously from 2GHz to 4GHz as shown in Figure 4.4 (b) where the BPF and BSF gain responses at Q=30 are normalized and superimposed. Measured variable gain range is 10-25dB over the frequency tuning range. The BPF Q is variable from 5 to >100 at 2-4GHz with stable circuit operation (K-factor>1) (Figure 4.4 (c)).

In BSF mode, with a fine VGA gain control, up to 50dB of notch attenuation is attainable (Figure 4.4. (b)) and the BSF can hold 50dB of attenuation over 5-to-40 Q variation, manifesting that the BW can be adjustable without compromising the stopband attenuation (Figure 4.4 (d)). The passband NF and IP_{-1dB} in BSF mode are measured by setting the notch frequency at 2 and

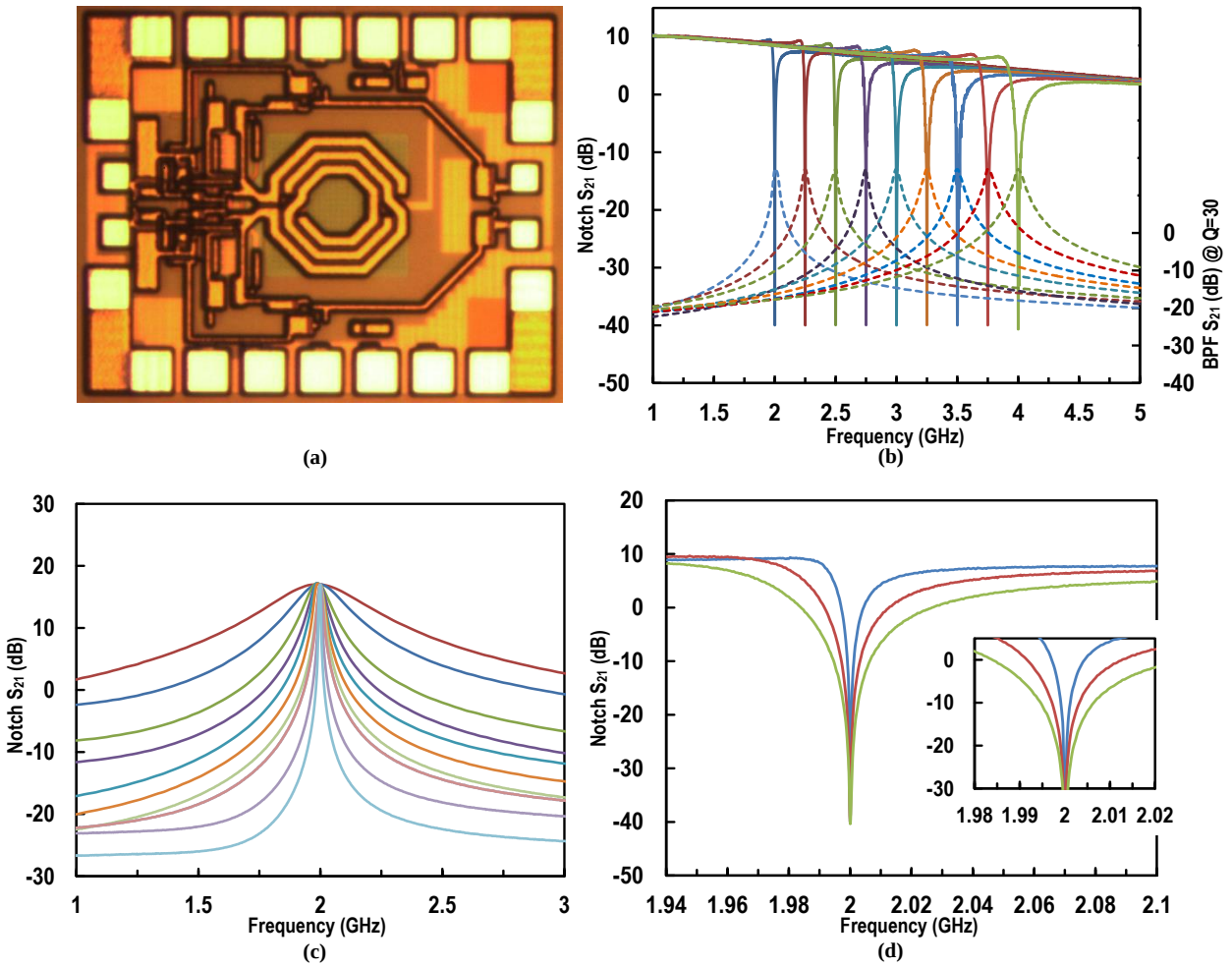

Figure 4.4: The reconfigurable BPF/BSF (a) chip photograph (chip size: 0.62x0.57mm^2), (b) Measured tuning characteristic: frequency tunings for BPF and BSF, (c) Q (BW) tuning in the BPF, (d) notch Q (BW) tuning in BSF.

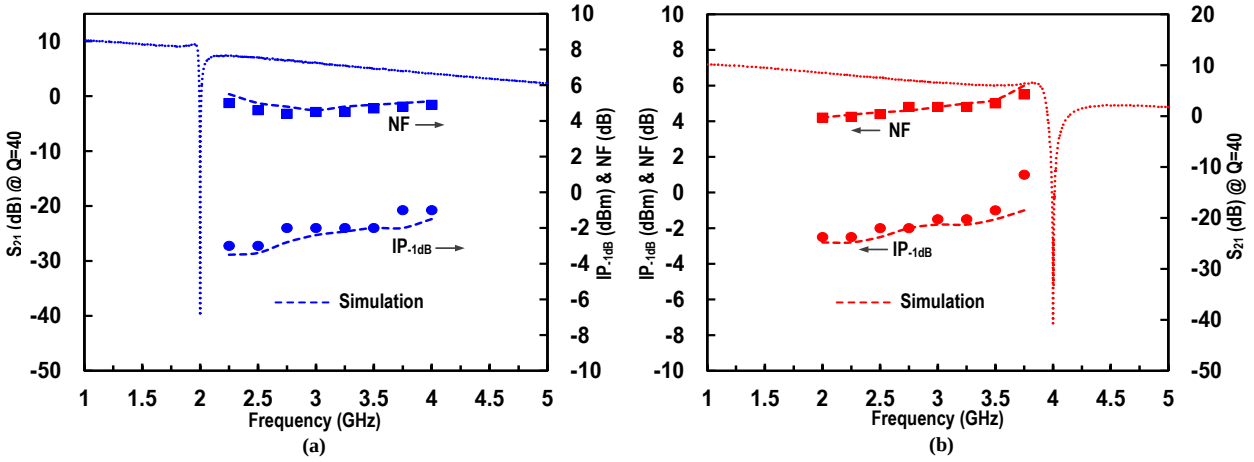

Figure 4.5: The band-stop mode measured NF and Linearity test, (a) Notch is at 2 GHz, (b) Notch at 4 GHz.

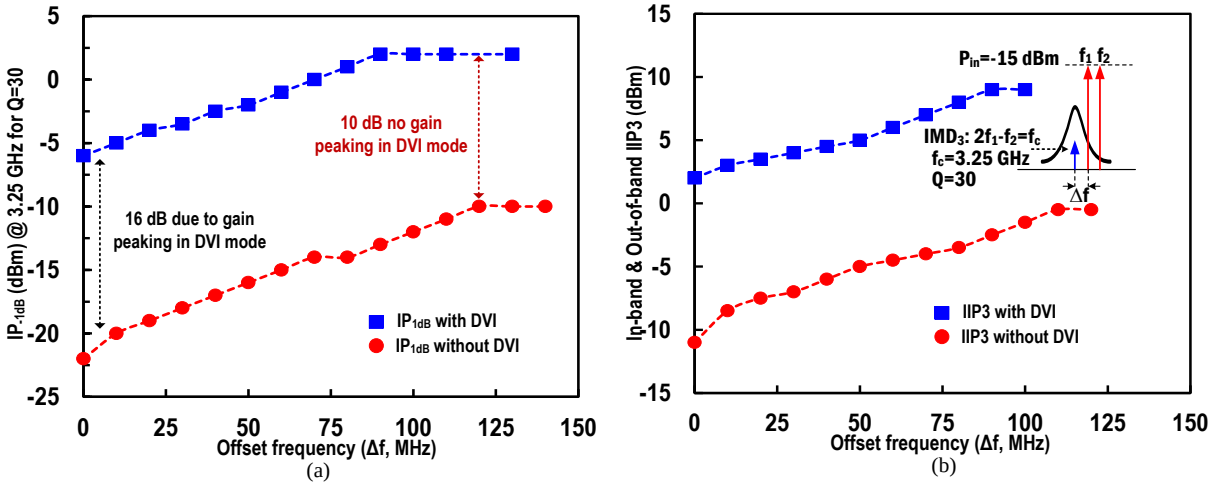

Figure 4.6: The band-pass mode measured Linearity test, (a) IP_{-1dB} with proposed DVI control, (b) IIP3 with proposed DVI control.

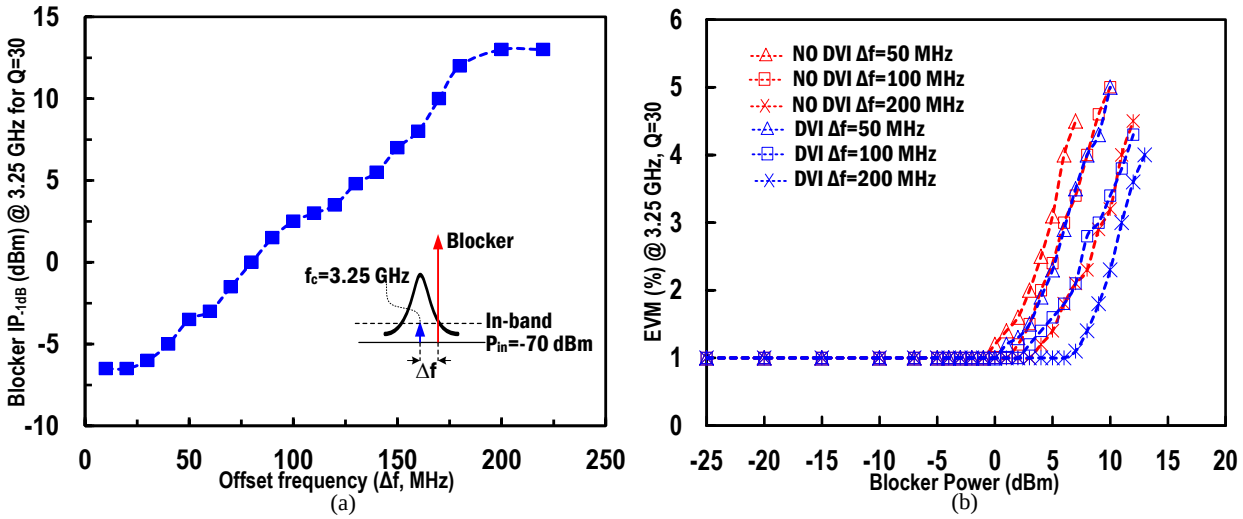

Figure 4.7: BPF-mode: OOB blocker (a) P_{-1dB} power compressing in-band signal gain by 1dB (Pin=-70dBm), and.(b) Error Vector Magnitude (EVM) test, when the modulated 65 QAM signal is centered at 3.25 GHz with 10 MHz bandwidth.

4GHz and the results are shown in Figure 4.5 (a) and (b). The IP_{-1dB} ranges from -3 to +1 dBm and NF varies from 4-5 dB in both cases result in the normalized DR of 166-169 dB·Hz in the passband in band stop mode (DR=174-NF+IP_{-1dB}). The wideband amplifier dictates the passband signal quality and the linearity increases in a proportional manner as the increase of the active circuit power dissipation as mentioned before.

In BPF mode, linearity of the filter is improved 16 dB for in-band and 10 dB for out of band using the proposed DVI control technique. The difference between the linearity improvement is because of gain peaking. The in-band signal experiences more gain peaking therefore higher IP-

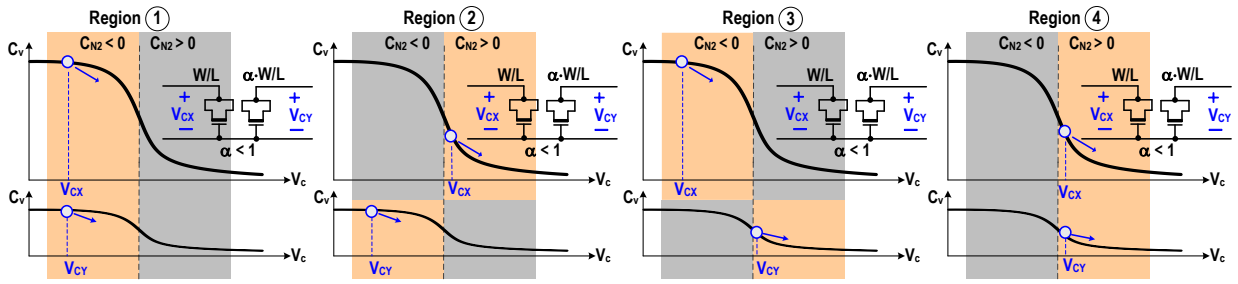

Figure 4.8: Dual Varactor Control scheme to improve the linearity.

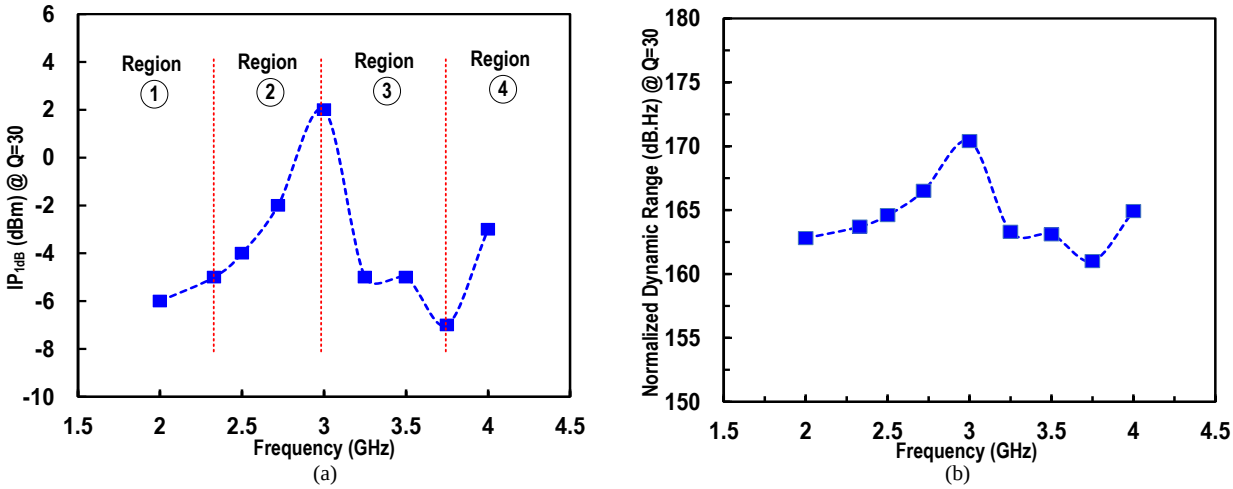

(a) (b)

Figure 4.9: (a) IP-1dB versus frequency which shows the effect of DVI control, (b) Normalized dynamic range.

$_{1dB}$. Fig 4.6 shows the in-band and out of band measured IP_{-1dB} and IIP3 test in which the power handling of the proposed filter has improved significantly. Figure 4.6 (b) shows 13 dB of IIP3 improvement with DVI control. The difference in IIP3 and IP_{-1dB} improvement comes from gain peaking as discussed in chapter 2. In the BPF mode, a resilience to a strong in-band and out-of-band (OOB) blocker has been characterized by measuring the blocker power distancing Δf from a center frequency (f_c=3.25GHz) that causes 1dB gain compression of the weak in-band signal at 3.25GHz (P_{in}=-70 dBm). The minimum in-band blocker P_{-1dB} at near the f_c is -6dBm, when the BPF Q=30. The maximum OOB blocker P_{-1dB} is limited to ~14dBm at Δf≥200MHz when the BPF Q=30 (Figure 4.7 (a)). Similarly, in the OOB two-tone test shown in Figure 4.6 (b), when the Δf is smaller than 3dB BW, the in-band IIP3 approaches to 2dBm, when the BPF Q=30, while the OOB IIP3 increases up to ~10dBm, thank to linearity improvement techniques. In Fig 4.7 (b) Error Vector Magnitude (EVM) test is shown, when the modulated 65 QAM signal is centered at 3.25 GHz with 10 MHz bandwidth and -20 dBm of the signal power. Measurement is performed when strong blocker is 50, 100, and 200 MHz away from the modulated signal center frequency. As it is clearly shown at Fig 4-6 and Figure 4.7 (b), DVI control improves both in-

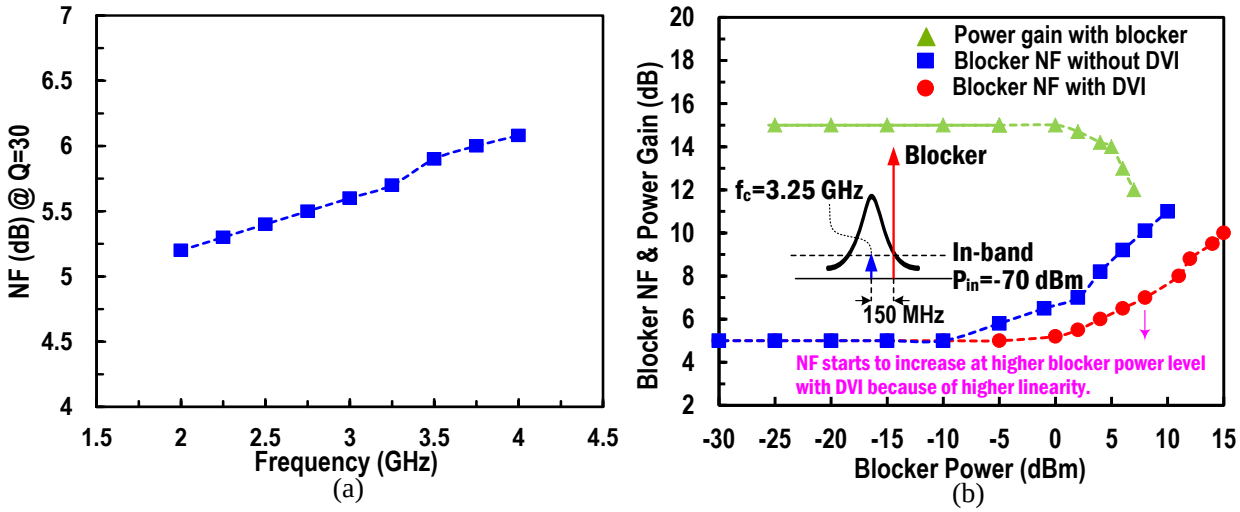

Figure 4.10: (a) NF versus frequency (by increasing frequency, filter gain increases, keeping the gain constant requires decreasing the g_m stage in filter which corresponds to less than 1 dB NF variation), (b) Blocker NF improvement using DVI control.

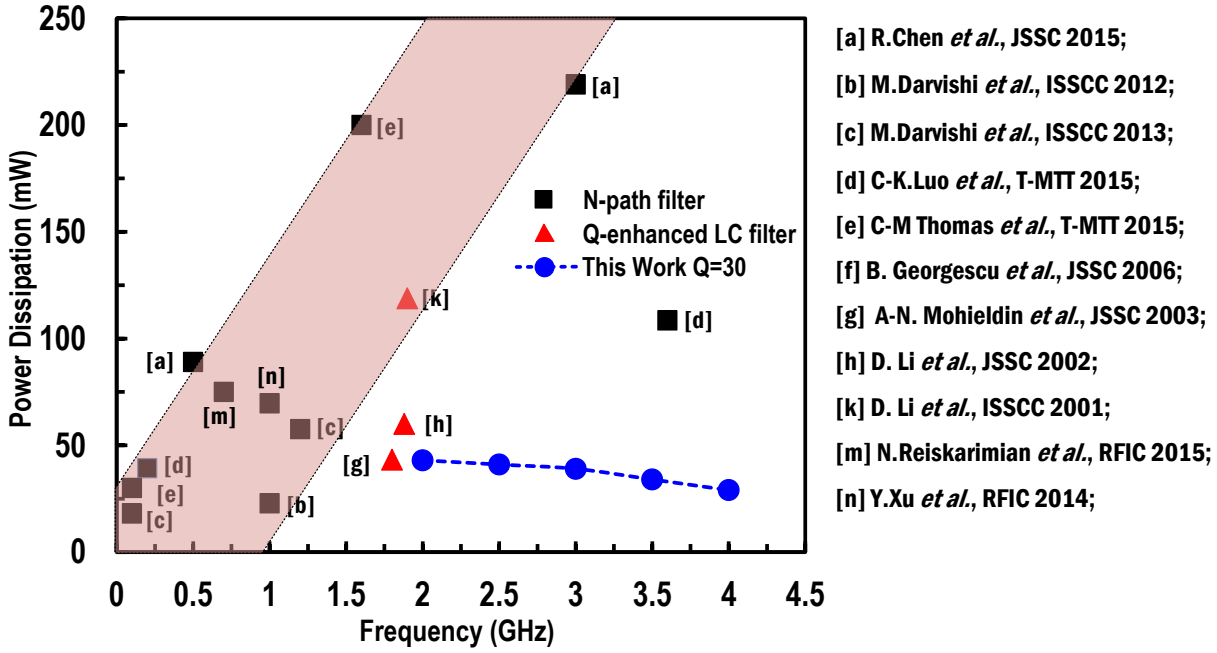

Figure 4.11: Power consumption of the propose mode reconfigurable filter with recent state of the arts.

band and out of band linearity performance. Figure 4.8 shows the DVI control scheme over the 2 to 4 GHz frequency range which corresponds to IP_{-1dB} shown in Figure 4.9 (a). Depending on the varactor control voltages the linearity improvement varies. Figure 4.9 (b) shows the normalized dynamic range calculated from 174-NF+IP_{-1dB} for the reconfigurable filter in band pass mode.

The peak DR of 170.4 dB.Hz is achieved for mid-band where the linearity improvement is maximum. Figure 4.10 (a) shows the measured NF over the 2-4GHz frequency range in band pass mode when the gain of the filter is set to 15 dB. Less than 1 dB variation in NF is due to decreasing g_m stage in the band pass filter to keep the overall gain constant for all measurements. Finally, Figure 4.11 compares the power consumption of the propose mode reconfigurable filter with recent state of the arts including Q-enhanced LC filters and N-path filters. Unlike N-path filter in which power consumption increases with increasing center frequency, in this work P_{dc} decreases in higher frequency. This comes with increasing tank Q as frequency increases and therefore less need for g_m stage in band-pass filter.

4.4 Summary

A mode reconfigurable filter in o.13 µm CMOS process has NF as low as 4 dB with the novel filter structure, and IP_{-1dB} as high as +2 dBm with proposed linearity technique. Power consumption is much less than other works with 2:1 frequency tuning and independent Q tuning of the filter.

Chapter 5 : 4th Order Active Notch Feedback Based Interference-Rejection System

5.1 Introduction

The proliferation of 4G Long-Term Evolution (LTE) wireless networks prompts that 4G communication signals ever get closer to S-band (2-4 GHz) radar frequencies, causing mutual interferences to each radio and radar systems [1]. It is highly desirable to filter out the 4G LTE interferers at the earliest possible stage in a receiver chain for radar sensors to prevent reception of false target signals or lost of synchronous target signals. For the interference filtering, because of dynamic switching clocks associated with driving mixer arrays and thereby because of a potential spur issue, the application of recent N-path filters [24] is limited for spur-sensitive radar front-ends. The prior feed-forward or feedback techniques in [6] or [42] involve a complicated dual-domain (RF and IF) reciprocal frequency up/down conversion process to locate and filter out blockers, either making the filtering systems sensitive to mismatch effects or claiming huge DC power penalty.

The proposed Q-enhanced LC filter, in chapter 3, relaxes the tradeoff between Q and linearity. Dual Varactor Inverse (DVI) control improves varactor nonlinearity substantially and further linearity improvement is achieved using dynamic negative resistance for gain peaking. However, at 3.25 GHz IP_{-1dB} decreases to -4 for Q of 150. If more linear system is required, feedback system is a good solution since negative feedback improves the linearity.

5.2 Feedback System Design

Figure 5.1 shows overall block diagrams of the S-band radar receiver employing a limiter that protects the following receiver chain from catastrophic failure by a high power jamming signal (typically > 100's W). The use of external narrowband GaN LNA having a high dynamic range capability (NF<1dB, OP-1dB>25dBm) opens opportunity for cost effective silicon integrations of following receiver blocks while meeting typical -120dBm of radar sensitivity requirement.

In the OOB filtering BPF subsystem present in Figure 5.1, a high frequency selectivity (Q) is obtained by a feedback cancellation of the OOB signals in the bandpass current domain. The in-band signal is band-passed with a 4th order response at node ② via the series of 2nd-order LC tanks afforded by the G_m's load (L1-C1-R1) and 2nd-order BPF. As illustrated, the OOB signals are first abated by the LCR load at node ①with a finite Q_1 {=R_1/Z_o, $Z_o=\sqrt{(L_1/C_1)}$} and then the in-band signal and residue of OOB signals are forwarded to node ③ by an all-pass filter (APF). With the gains are matched between the BPF and APF branches using a VGA (G_A), the

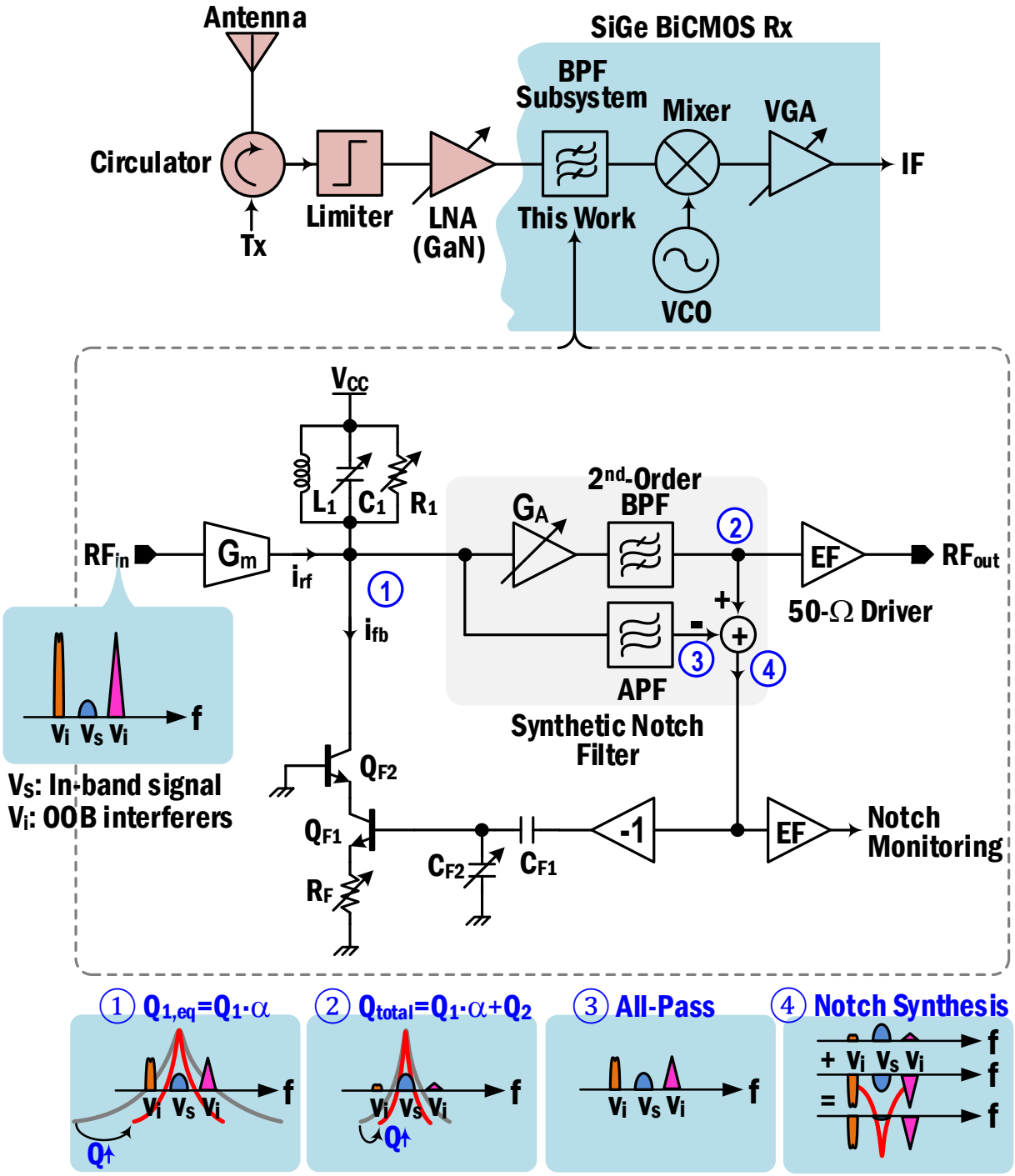

Figure 5.1: The block diagrams of the radar receiver employing external front-end III-V (GaN) LNA and integrated back-end receiver in SiGe BiCMOS process, and notch-feedback based out-of-band interference rejection bandpass filter (BPF) subsystem (this work).

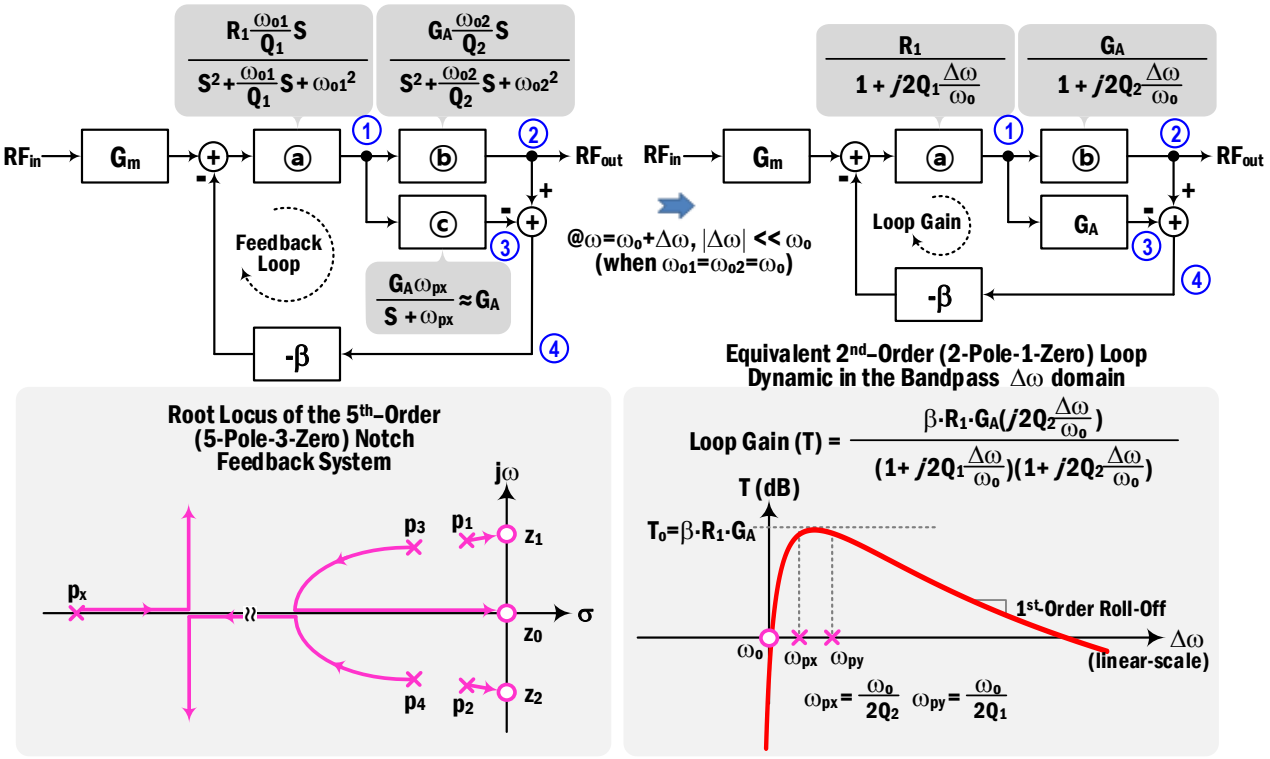

Figure 5.2: The 5th – order (5-pole-3-zero) notch feedback system block diagram and its root locus plot (left), and equivalent 2nd – order (2-pole-1-zero) loop dynamic in the band-passed offset frequency (Δω) domain (assume that $Q_2>Q_1$).

subtraction of the APF output from the BPF output synthesizes a 4th-order notch response at node ④, extracting the remnant OOB signals which are subsequently converted to a feedback current i_{fb} by the feedback network comprised of $C_{F1,2}$, $Q_{F1,2}$ and R_F. The deduction of i_{fb} at node ① closes the negative feedback loop, suppressing the OOB signals further and thus scaling up the LC tank Q_1 by the factor α which is associated with the feedback loop gain. The total filter Q becomes $Q_1 \cdot \alpha + Q_2$, where Q_2 is the selectivity of the 2nd-order BPF. Note that by establishing the feedback loop right after the G_m cell in the current domain, the OOB interferers can be rejected substantially at the earliest possible stage, relaxing the dynamic range issues of the following active circuits.

To investigate the Q scaling factor and loop stability, the notch feedback system is modeled in Figure 5.2 (right) where the LCR load and BPF are expressed as 2-pole-1-zero systems in the function blocks ⓐ and ⓑ, respectively. The APF is implemented using a wideband amplifier and modeled as a one-pole system creating a parasitic pole of p_x ($=-\omega_{px}$). The feedback factor β is $C_{F1}/(C_{F1}+C_{F2}) \cdot g_{mF1}/(1+g_{mF1}R_F)$ where g_{mF1} is the transconductance of Q_{F1} in Figure 5.2.

By setting $Q_2>Q_1$ and $\omega_{o1}=\omega_{o2}=\omega_o$ (ω_o: input signal frequency), the BPF generates the dominant open-loop complex pole pair of $p_{1,2}$ and the G_m load creates the adjacent pole pair of $p_{3,4}$, making overall 5^{th}-order control system. The feedforward subtraction in the notch synthesis at node ③ introduces two complex zeroes, z_1 and z_2, and stabilizes the feedback loop by preventing the dominant complex poles from trespassing on the RHP plane in the root locus plot in Figure 5.2. If the bandwidth (ω_{px}) of the wideband amplifier is large enough, e.g. x10 higher than ω_o, the impact of p_x on the feedback loop dynamic is negligible, virtually degenerating the feedback to a 4^{th}-order dynamic system which can be further simplified to a 2^{nd}-order feedback system in the band-passed offset frequency ($\Delta\omega$) domain. The feedback system is equivalently modeled in the $\Delta\omega$ domain in Figure 5.2 (left) where the 2^{nd}-order LCR load and BPF are approximated as first-order systems having poles of $-\omega_o/2Q_1$ ($-\omega_{py}$) and $-\omega_o/2Q_2$ ($-\omega_{px}$), respectively, under the assumption of $\Delta\omega<<\omega_o$. The notch filtering at node ④ is corresponding to inserting a zero at $\Delta\omega=0$, leading to a phase-lead compensation and phase margin (PM) greater than 90^o; in actual circuit implementations, due to parasitic high frequency poles the PM degrades by $5\text{-}10^o$, resulting in $>80^o$ PM. The closed loop response at node ① is $G_mR_1/(1+j2Q_1\Delta\omega/\omega_o)\times 1/(1+T)$ which can be simplified to $G_mR_1/\{1+j2Q_1(1+T_o\cdot Q_2/Q_1)\Delta\omega/\omega_o\}$, where T is the loop gain and $T_o=\beta R_1G_A$ as expressed in Figure 5.2. Therefore, the selectivity scaling factor $\alpha=1+T_o\cdot Q_2/Q_1=1+\beta R_1G_A\cdot Q_2/Q_1$ and the overall selectivity of the feedback system is $Q=Q_1(1+\beta R_1G_A\cdot Q_2/Q_1)+Q_2$.

Figure 5.3 shows the complete schematic of the synthetic notch filter composed of a 2nd-order BPF in parallel with a wideband amplifier playing the role of all-pass filter at the band of interest. A replica of the BPF LC tank is added to the G_m cell and therefore a 4^{th} order response is achieved. Figure 5.4 shows the comparison of the 2^{nd} order response, BPF in chapter 2, and the 4^{th} order response. The interference rejection system operating in either feedback mode or open loop has 30 dB more out of band rejection than the 2^{nd} order BPF.

For open loop operation, the bias of the $Q_{F2and\ F4}$ is disabled, so the system works as an open-loop cascaded 4^{th} order LNA with BPF. In open loop operation the total Q of the system is controlled by Q of LC tank. However, in closed loop operation, the feedback gain controls the total Q once the Q of the LC tanks is set to lower value for NF and Linearity consideration.

In schematic of Figure 5.3, G_m boosted structure is utilized to increase the gm of the first stage while keeping the input matching for measurement purposes. R_{E2} is added to all pass amplifier to increase the gain and reduce the NF. R_E and C_{F2} are controlling the feedback gain in which R_E is responsible for course tuning and C_{F2} is used for fine tuning.

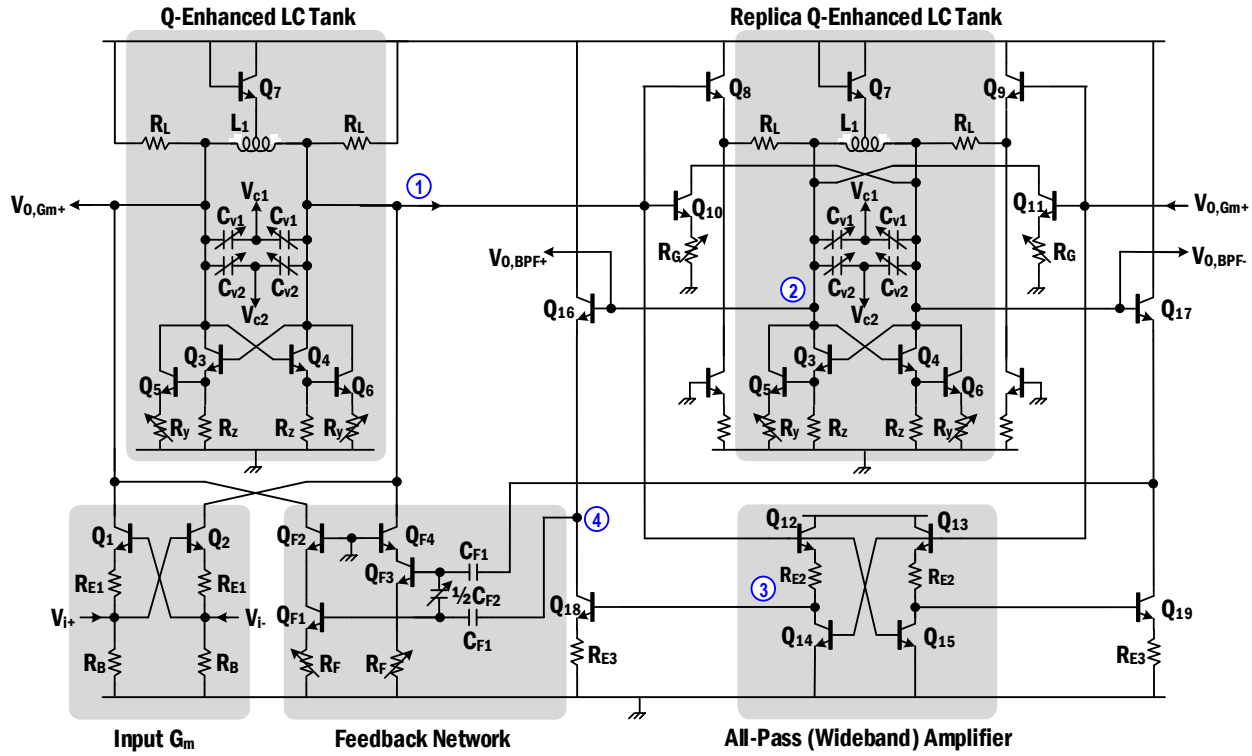

Figure 5.3: Schematic of the synthetic notch filter composed of a 2nd-order BPF in parallel with a wideband amplifier playing the role of all-pass filter at the band of interest (conceptual diagrams of filtering in of interference V_i are shown together).

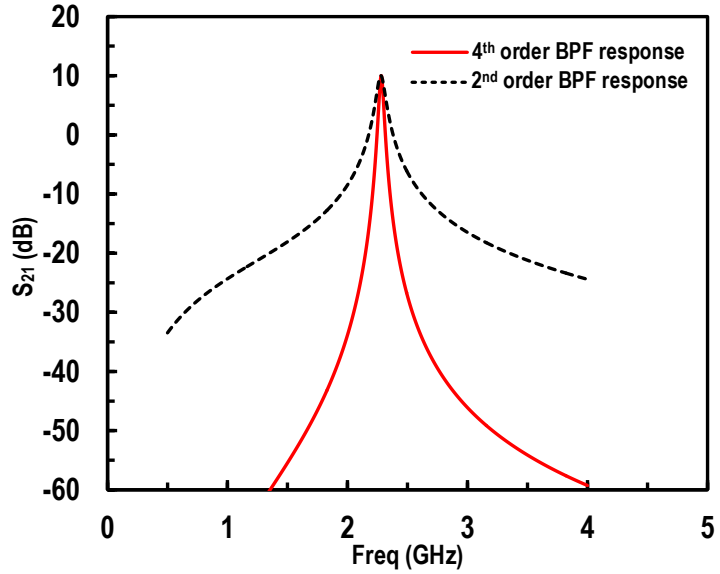

Figure 5.4: Simulated S_{21} for 4th order BPF (Q=60) and 2nd order BPF (Q=30) in chapter 3.

5.3 Measurement Results

The 4^{th} order feedback based interference rejection system is designed and fabricated in 0.13 µm BiCMOS process. The performance of system is measured after standard differential SOLT calibration. Chip photo is shown in Figure 5.5 (a) with active area: 0.8×0.9 mm^2. As can be seen the system has two outputs. One is the RF band pass output and the other is to monitor the notch response. With the varactor tuning, the filter f_c can be controllable continuously from 2GHz to 4GHz as shown in Figure 5.5 (b). The measured responses at 2, 3, and 4 GHz are shown for simplicity however continues tuning is possible over 2-4 GHz. For this measurement, first open loop Q is set to 20 (dashed line), the first tank Q ~5 and the BPF Q~15, then $Q_{17,18}$ subtract the band pass filter output from the all pass amplifier and a sharp notch is created. The notch attenuation is controlled through gain matching between band pass filter and all pass amplifier using the gain stage in BPF (R_G in Figure 5.3). Once the notch is created, it will place in the desired signal and all the interferer will subtract at the G_m output node using the negative feedback. Therefore in closed loop mode by increasing the loop gain, higher selectivity is achieved (Q>100). (The BPF gain responses are normalized and superimposed). Measured variable gain range is 10-25dB over the frequency tuning range. The BPF Q is variable from 5 to >100 at 2-4GHz with stable circuit operation (K-factor>1).

While the high Q response at Q-enhanced LC filter comes at the cost of degrading linearity, negative feedback improves the linearity of the system as shown in Figure 5.6 (a). For this measurement, the gain of the system slightly decreases due to negative feedback in closed loop operation, and gain of the system is kept constant in open loop mode using BPF gain control. For the same set up, NF is also measured and shown in Figure 5.6 (b). Both measurements are done at 3GHz and very well matched with simulation. Figure 6.5 (a) reveals the main advantage of the feedback system over the open loop structure, as the selectivity increases, the linearity not only does nit degrade, but also improves using the negative feedback. Therefore, the system handles the blocker as strong as +1 dBm with very high selectivity Q>100. To give an insight on the proposed linearization techniques, consider >12 dB improvement in IP_{-1dB} in chapter 2 using DVI control and dynamic negative resistance which results in -4 dBm of IP_{-1dB} for Q~100, in the feedback approach IP_{-1dB} of +1 dBm is obtained for the same selectivity which in total improves the power handling of the interference rejection system >16 dBm.

While feedback improves the linearity when high selectivity is required, in open loop mode bandwidths as high as 600 MHz is achievable.

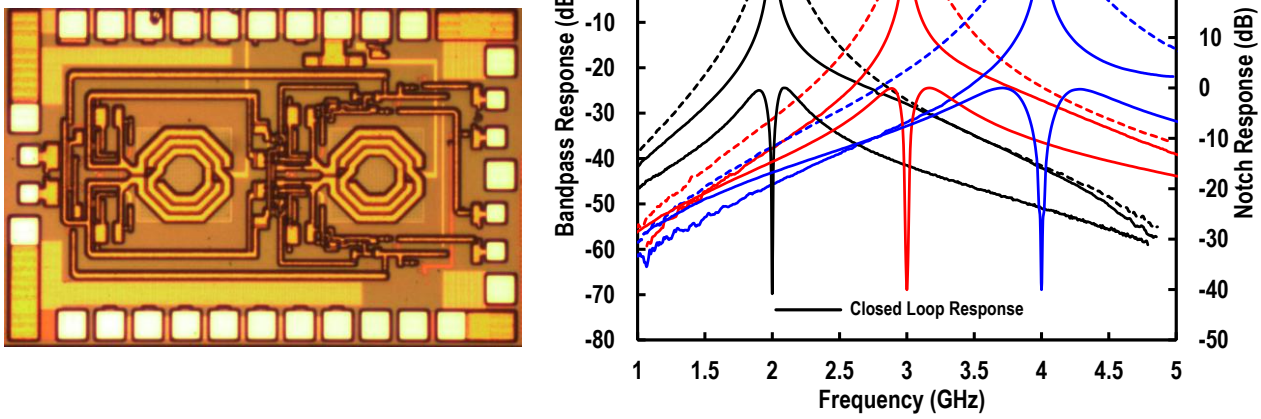

(a) (b)

Figure 5.5: (a) chip photo (active area: 0.8×0.9 mm^2), (b) Measured system S_{21} for band pass and notch outputs.

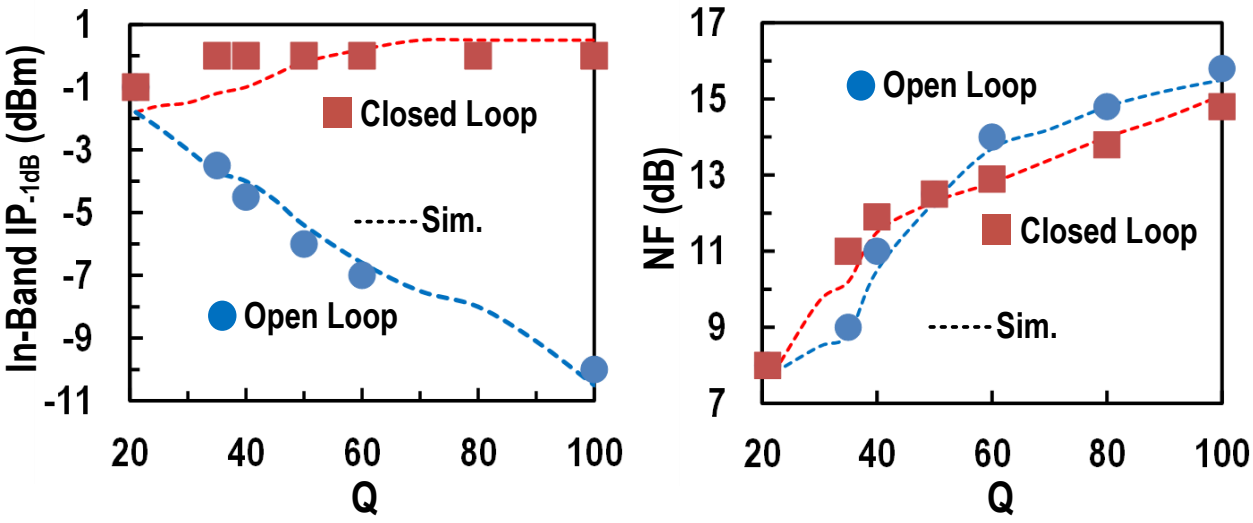

Figure 5.6: Measured and simulated (a) linearity performance of the feedback system versus open loop system, (b) NF of the proposed open loop and feedback system at 3 GHz.

Figure 5.7 shows the bandwidth tuning over 2-4 GHz range. The plots at each frequency correspond to 30 MHz, 200 MHz and 600 MHz respectively. Figure 5.8 (a) shows more detailed of high bandwidth tuning at 3.5 GHz. For high bandwidth mode it is important to have as constant group delay as possible to avoid distortion in desired signal, as shown in Figure 5.8 (b) group delay variation for maximum bandwidth is less than 300 ps.

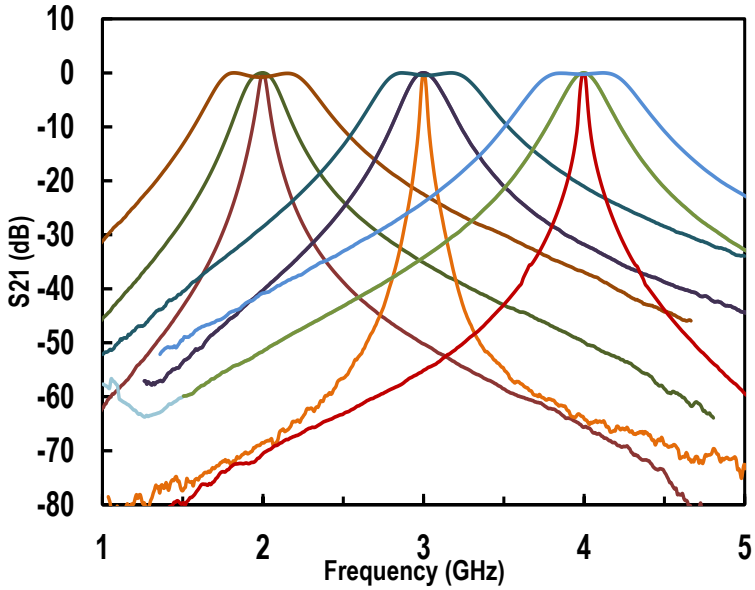

Figure 5.7: Measured S_{21} for frequency and bandwidth tuning in open loop mode.

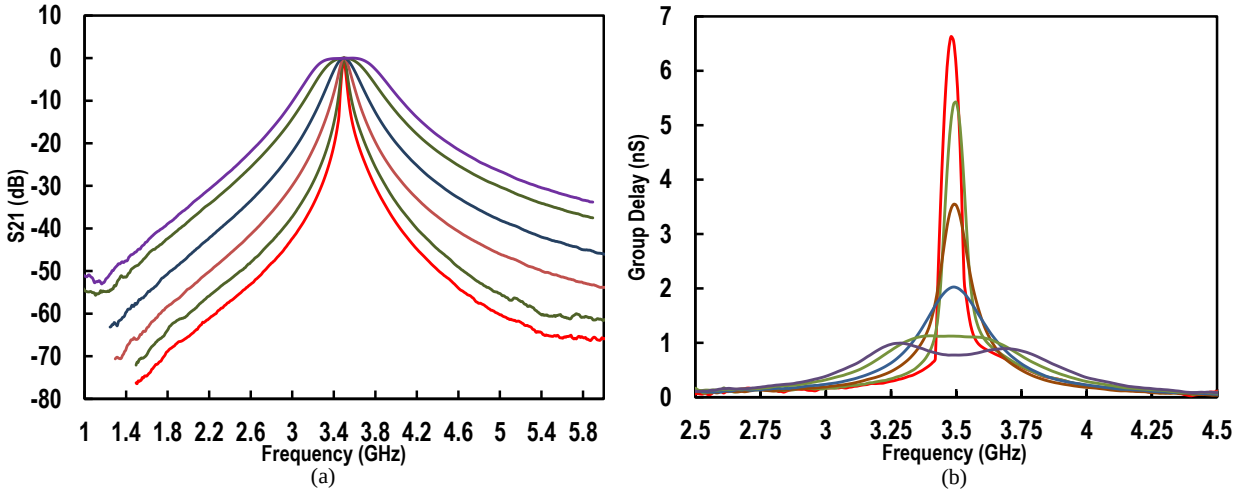

Figure 5.8: Measured (a) S_{21} at 3.5 GHz for BW up to 600MHz, (b) Group delay variation for different bandwidths.

Out of band blocker test is performed for both open loop and feedback system. In blocker IP-1dB a single tone is placed at filter center frequency while at EVM test a modulated signal is placed at center frequency. These two tests together show the performance of the filter at presence of the strong blocker. Figure 5.9 (a) displays negative feedback improves out of band linearity also as well as in-band linearity when a small signal tone is located at the filter center frequency, and the blocker power at each offset frequency increases till the small signal in-band signal degrades by 1 dB.

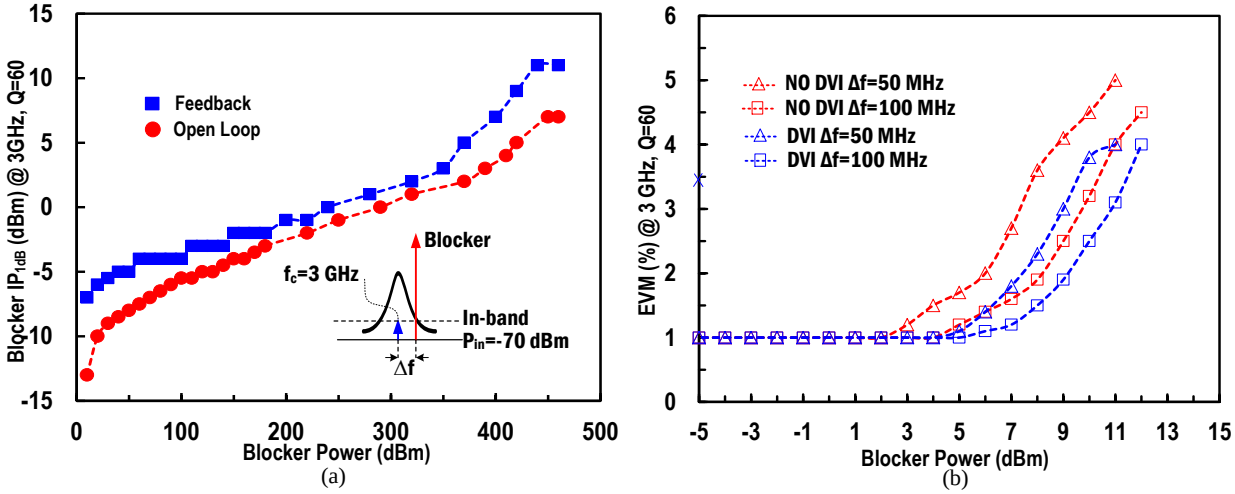

Figure 5.9: (a) Measured blocker IP_{-1dB} , (b) measured EVM for 64 QAM modulated signal with 10 MHz BW centered at filter center frequency (3GHz).

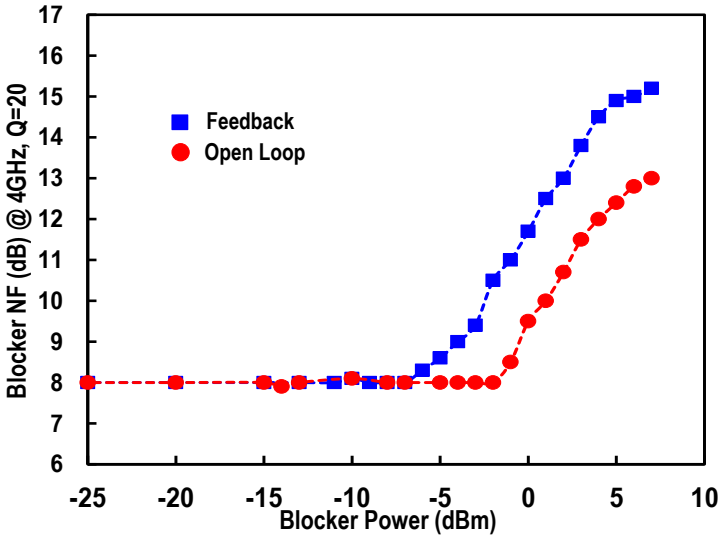

Figure 5.10: Measured Blocker NF when the blocker is 200 MHz away from filter center frequency.

Figure 5.9 (b) shows the EVM test for both open loop and feedback mode when a modulated 64 QAM signal with 10 MHz BW is placed at center frequency of the filter (3GHz) and filter Q=60, blocker located at two different offset of 50 and 100 MHz. Both Blocker IP_{-1dB} and EVM test show the feedback improves the out of band linearity as well as in band since the notch is placed on desired signal and blockers will be rejected in feedback node.

The measured NF is 8 dB for center frequency of 3GHz and Q=20 without a blocker, while the presence of the strong blocker increases NF. In Figure 5.10 filter center frequency is still at 3

Table I: The proposed feedback system comparison with recent state of the arts

	This Work	ISSCC 2012 M. Darvishi *et al.*	CICC 2015 L. Mohammadi *et al.*	JSSC 2007 H. Darabi	JSSC 2010 T.D. Werth *et al.*	ISSCC 2012 S. Youssef *et al.*
Type	Feedback (RF domain)	Open Loop N-Path	Open Loop Q-Enhanced LC	Feed Forward (RF-IF domain)	Feedback (RF-IF domain)	Feedback (RF-IF domain)
Process	0.13µm SiGe BiCMOS	65nm CMOS	0.13µm SiGe BiCMOS	65nm CMOS	65nm CMOS	65nm CMOS
Frequency (GHz)	2 – 4	0.3 – 1.2	2.25 – 4.5	1.96	1.9	1 – 2.5
Filter Order	4^{th}	4^{th}	2^{nd}	NA	2^{nd}	NA
Ultimate Rejection (dB)	> 60	55	45	> 21	30	48
Q Tuning	5 – 120	NO	3 – 150	NO	NO	NO
Pass-Band Gain (G, dB)	10 – 20	3.5	0 – 20	20.9	24.7	30
NF (dB)	8 – 14 @Q=20 – 100	9.5	16.5 @Q=100	6.8*	7*	7.25 – 8.9*
Pass-Band IP_{-1dB} (dBm)	-1 – 0 @Q=20 – 100	-4.4	-4 @Q=100	-12	NA	-30**
Normalized DR[a] (dB·Hz)	161.5 @Q=50 160 @Q=100	160.1 @Q=40	153.5 @Q=100	155.2	NA	136
OOB P_{-1dB} Blocker (dBm)	> 7	NA	> 6	NA	NA	-3
Blocker NF (dB) @Blocker Power	8 @-5dBm 9.5 @0dBm	NA	NA	NA	10 @-10dBm	NA
DC Power (mW)	60 @Q=20	17.6 @1GHz	42.9 @Q=10	35 – 72.5	225***	62
Active Area (mm^2)	0.72	0.13	0.48#	0.28	1.2	0.39

a: calculated from $174+IP_{-1dB}$-NF (dB), *: including LNA, **: estimated from IIP3 (measured)-10dB, ***: excluding IF buffer power dissipation, #: including pads.

GHz and the effect of blocker is investigated when the blocker is placed at 3.2GHz. Since the negative feedback is decreasing the effect of the blocker at the feedback node, the better NF performance is achieved using the feedback system. Table I shows the performance of the proposed feedback system and compares the result with recent state of the arts. The main advantage of this work over Q-enhanced LC filter is the linearity performance, which does not degrade as filter Q increases. The proposed active notch feedback approach has also better performance than the other feedback and feedforward approaches in terms of out of band rejection, less sensitivity to the tuning circuitry, linearity, and power frequency tradeoff.

Chapter 6 : Conclusion

6.1 Summary and conclusion

The radio frequency (RF) and low-end of microwave frequency bands, typically < 18 GHz, are heavily congested by the explosive growth of commercial wireless technologies. The coexistence of many wireless transceivers with different standards becomes the norm in the contemporary wireless network operations. This prompts that communication frequency bands become closer to existing radar frequencies and the spectral proximity causes mutual interference to the communication networks and radars. Consequently, the interference environment becomes more hostile and more complex in contemporary heterogeneous wireless network environments. The rejection of a strong out-of-band blocker at the earliest possible stage in a receiver chain is critical to prevent the wireless systems, radios and radars, from being saturated by the blocker.

In this research, a Q-enhanced LC bandpass filter in 0.13 μm SiGe BiCMOS technology which has a wide turning range of 2:1, 2~4 GHz, 4-8 GHz, and 8-16 GHz with independent Q control up to 150 over the overall frequency range is designed and measured. The proposed LC filter employs voltage-mode (low-gain) and current-mode (high-gain) drivers for more flexible operation in the noise-linearity tradeoff space. The proposed dual varactor inverse (DVI) control can suppress varactor nonlinearity substantially. The gain peaking technique enabled by a dynamic negative resistance circuit effectively increase the filter's power handling capability further. These result in exceptional level of 150~170 dB·Hz of normalized filter dynamic range when Q varies from 10 to 100, one of the best performances compared with previous state-of-the-art Q-enhanced LC and N-path filter designs.

In the second step of the research, synthetic notch filters comprised of a Q-enhanced band-pass filter and a wideband amplifier playing the role of an all-pass filter at the bands of interest are designed and measured. By subtracting the BPF output from the APF output, a notch response can be developed with rejection primarily depending on the gain matching between the BPF and APF. The filter frequency selectivity will be set by the BPF and filter dynamic range will be determined by the all-pass amplifier independently, allowing a focused independent design optimization for dynamic range in the amplifier and selectivity in the BPF. Therefore, the synthetic filter can break the ingrained performance tradeoff between selectivity and dynamic range in the Q-enhancement LC filters. Also, the stop-band attenuation will no longer be traded with filter bandwidth. These tradeoff-free band-stop filters could allow tremendous operational versatility to suppress blockers more effectively under dynamically changing interference environments. The notch filters were successfully designed, implemented, and demonstrated in

both 0.13 μm SiGe BiCMOS technology and 0.13 μm CMOS process.

In third step, a reconfigurable band-pass/band-stop filter in 0.13 μm CMOS is designed. To be more practical in receiver front-end an LNA is realized before a reconfigurable filter. Utilizing the proposed linearity improvement techniques, dynamic negative resistance and dual-varactor inverse (DVI) control, will significantly improve dynamic range of a Q-enhanced LC filter capable of mode switching between bandpass (BPF) and bandstop (BSF) for a flexible blocker filtering adaptive to the dynamic blocker environments.

In last step, an active notch feedback based out-of-band interference cancellation system is designed and measured. Unlike other work, the proposed feedback system is not sensitive to mismatches and power consumption is not frequency dependent. Simple structure with an outstanding performance makes it a great candidate for RF frontend.

6.2 Contributions

While many research efforts have been made to improve the frequency selectivity in integrated filters, the filter performance is strongly constrained by tightly coupled tradeoffs amongst filter selectivity, dynamic range, and power consumption. For instance, in the Q-enhanced LC filters due to a nonlinearity and noise of a negative transconductor, the filter dynamic range degrades significantly as the filter Q increases. Also, N-path filters have problems with system complexity and power penalty which likely limit their application below ~1's GHz range. Therefore, there is still compelling research needed to resolve the intrinsic problem of performance tradeoffs in active filters and interference rejection systems in order to provide more power-efficient, hardware-economic, and robust filtering solution in addition to filter-mode reconfigurability adaptive to blockers environment.

To improve the bandwidth, selectivity, configurability and interference rejection of the wireless systems, a variety of filter topologies are proposed and implemented with a frequency spectrum from 2 GHz to 20 GHz. Figure 6.1 shows an overview of my PhD research with the following three important topics:

6.2.1 Frequency and Bandwidth-Tunable RF and Microwave Filters for Multi-Radio Networks - In this study, design, and implementation of the band-pass (BPF) and band-stop (Notch) filter architectures from 2-16 GHz are shown in a cost-effective silicon process. More specifically: 1) a 2nd- order Q-enhanced BPF with a high dynamic range; and 2) a synthetic band-stop (notch) filter leveraging the proposed BPF are developed (See Figure 6.1 ① and ②). In conventional BPF design, as the filter Q increases for better selectivity, the dynamic

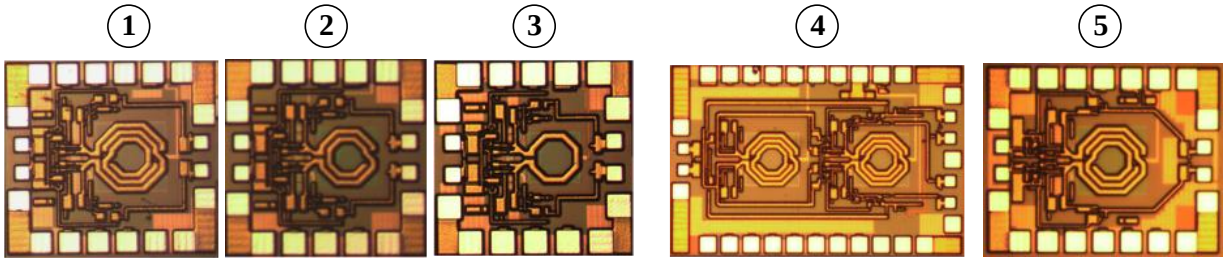

Figure 6.1: Filters chip photographs in 0.13-µm CMOS and BiCMOS technology: ① band-pass filter at 2-4 GHz, ② notch filter at 4-8 GHz, ③ reconfigurable filter at 8-16 GHz, ④ notch feedback based interference rejection system at 2-4 GHz, and ⑤ RF front-end with integrated filter at 2-4 GHz.

range decreases, and this presents the main challenge in BPF design. In BPF mode, utilizing two proposed techniques, 1) a dynamic negative resistance and 2) a dual-varactor with inverse (DVI) control, the large signal handling capability in the Q-tuning and frequency-tuning elements in the LC filter increases substantially. To prove the concept, BPFs at 2-16 GHz and a notch filters at 2-16 GHz are realized in IBM SiGe BiCMOS process.

6.2.2 High Selectivity Interference Rejection System - Figure 6.1 ④ shows the chip photo of the 4th order notch feedback-based interference rejection system. The system can also operate as an open loop cascaded 4th order LNA with BPF or feedback system. In closed loop operation, notch will be put on the desired signal and the negative feedback subtracts all unwanted signals from the input, therefore high Q band-pass characteristic is achieved at the RF output. In addition, 4th order response has better out of band rejection, more than 30 dB attenuation for blockers in comparison with a 2nd order response. The main advantage of the feedback is, improving linearity of the system.

6.2.3 All CMOS Reconfigurable Front-end for Interference Rejection - A Q-enhanced LC filter capable of mode switching between band-pass and band-stop modes for a flexible blocker filtering adaptive to the dynamic blocker environments is shown in Figure 6.1 ③ and ⑤. To be more practical in receiver front-end an LNA is realized before the reconfigurable filter and is fabricated in 0.13 µm CMOS process.

6.3 Future research directions

In the near future, interference issue will be more problematic as proliferation of wireless devices in the "Internet of Things" environment, especially at frequencies below 18 GHz. Digital filtering at the backend is not efficient due to a high power consumption and analog to digital

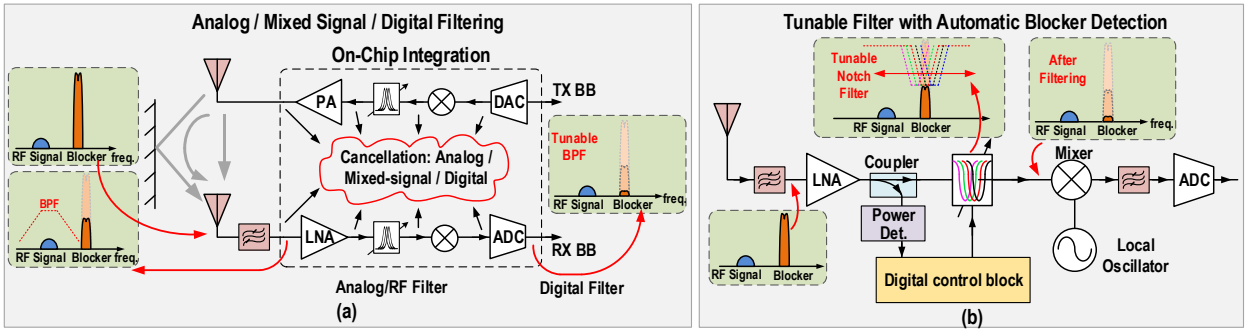

Figure 6.2: Block diagram of the SI rejection with wideband multi-node tapping, and (b) block diagram of the notch filter with automatic interference detection and rejection system.

interface problems at high frequencies and high bandwidth requirements. Therefore, developing innovative circuits and systems to alleviate the interference problem is a demanding research.

6.3.1 Self-interference Rejection/Cancellation Systems for Full-Duplex Wireless - In band full-duplex (FD) wireless communication has been a hot-topic allowing the transmission and reception to occur simultaneously at the same frequency and time. This emerging scheme promises up to 2 times spectral efficiency while introducing new challenges in the transmitter/receiver systems such as in-band self-interference (SI) and cross-talk. Many types of SI cancellation methods are introduced including high-isolation antenna design, multi-path filtering, TX chain replica, or duplexing LNAs. As a future research topic, providing new solutions like wideband tunable multi-node tapping from TX to RX chain, as shown in Figure 6.2 (a), offers promising route.

6.3.2 Automatic Interference/Blocker Detection and Rejection Systems for Multi-Radio Networks - The out-of-band blockers can be suppressed using RF band-pass filters (mostly off-chip) however in-band blockers can saturate the receiver chain if cannot be rejected especially before the mixer stage. In this research, the tuning is done manually to prove the proposed idea in the silicon die however automatic tuning mechanisms are required for multi-radio network and wireless systems. In addition to the tuning scheme, automatic blocker detection is another challenging task which needs to be explored. As shown in Figure 6.2. (b), a new architecture is proposed for automatic detection/tuning system that can control the center frequency of the notch filter or BPF to reject the in-band blockers. The automatic blocker detection will be added to the reconfigurable filter in the next step of the research. In this approach, an injection locked oscillator-based detector is utilized to find the blocker frequency. For the proposed system, an intensive study of automatic detection/tuning algorithms will be required.

APPENDIX A

As seen from Figure 2.5 (b), the output voltage to input current relation is as following:

$$\Delta V = \alpha_1 i_s + \alpha_2 {i_s}^2 + \alpha_3 {i_s}^2 \qquad (1)$$

By applying $v_s = R_p i_s$ to (1), the output-input voltage relationship can be obtained and 1dB compression point is then calculated. First, the error signal of the feedback system is:

$$i_e = i_s - \frac{j\omega_0 C_{N1}}{2}(\Delta V)^2 - \frac{j\omega_0 C_{N2}}{3}(\Delta V)^3 \qquad (2)$$

Using (1) and (2), the error signal in terms of input current is derived as:

$$i_e = i_s - \frac{j\omega_0 C_{N1}}{2}\left(\alpha_1 i_s + \alpha_2 {i_s}^2 + \alpha_3 {i_s}^2\right)^2 - \frac{j\omega_0 C_{N2}}{3}\left(\alpha_1 i_s + \alpha_2 {i_s}^2 + \alpha_3 {i_s}^2\right)^3 \quad (3)$$

Therefore, the output-input voltage relationship is :

$$\Delta V = i_e \cdot Z_T \qquad (4)$$

$Z_T(\omega)$ for a parallel RLC network can be approximated to (5).

$$Z_T(\omega) = \frac{j\omega \frac{\omega_o}{Q} \cdot R_p}{{\omega_o}^2 - \omega^2 + j\omega \frac{\omega_o}{Q}}$$

$$= \begin{cases} Z_T(\omega_o) = R_p, & for\ i_s\ at\ \omega = \omega_o \\ Z_T(2\omega_o) \cong -j\frac{2}{3}\frac{R_p}{Q}, & for\ i_{N1}\ at\ \omega = 2\omega_o. \\ Z_T(3\omega_o) \cong R_p, & for\ i_{N2}\ at\ \omega = 3\omega_o \end{cases} \qquad (5)$$

Where ω_0 is the center frequency of the LC tank and Q is the quality factor associated with it. There are higher order terms but we only interested in first, second, and third harmonics. The third harmonic generates ω_0 and $3\omega_0$ after expansion, but only the fundamental is desired for 1dB compression point calculation and the higher order terms are ignored.

It is noteworthy to mention when deriving the equation for 1dB compression point, double counting of frequency components should be avoided. If $i_{s(1st)} = e^{j\omega_0 t} + e^{-j\omega_0 t}$ is assumed, where ω_0 is the desired center frequency,

$$\left(e^{j\omega_0 t} + e^{-j\omega_0 t}\right)^3$$
$$= e^{j3\omega_0 t} + e^{-j3\omega_0 t} + 3e^{j\omega_0 t} + 3e^{-j\omega_0 t} = 6\cos\omega_0 t \qquad (6)$$

As it is shown, ${i_s}^3$ can produce an undesired in-band tone with the amplitude of $.6\cos\omega_0 t$. The interaction between second order nonlinearity and first order nonlinearity also creates in-band tone. Assuming $i_s(2nd) = e^{j2\omega_0 t} + e^{-j2\omega_0 t}$ created by feedback and interacted by fundamental which comes from the input, in-band tone for $i_s(1st)i_s(2nd) + i_s(2nd)i_s(1st)$ is calculated.

$$\begin{gathered}\left(e^{j\omega_0 t} + e^{-j\omega_0 t}\right)\cdot\left(e^{j2\omega_0 t} + e^{-j2\omega_0 t}\right) \\ + \left(e^{j2\omega_0 t} + e^{-j2\omega_0 t}\right)\cdot\left(e^{j\omega_0 t} + e^{-j\omega_0 t}\right) \\ = 2e^{j\omega_0 t} + 2e^{-j\omega_0 t} + 2e^{j3\omega_0 t} + 2e^{-j3\omega_0 t} \\ = 4\cos\omega_0 t \qquad (7)\end{gathered}$$

When nonlinearity is only feedforward, (7) will not be created. Therefore, (6) and (7) should be normalized by 6 which lead to multiplication of (7) by $^2/_3$ when it is added to (6) in the well-known 1-dB compression point equation. Using (3), (4), and (5) results in the following:

$$\Delta V = i_e(\omega_0)\cdot Z_T(\omega_0) + i_e(2\omega_0)\cdot Z_T(2\omega_0) + i_e(3\omega_0)\cdot Z_T(3\omega_0) \qquad (8)$$

$$i_e(\omega_0) = i_s \qquad (9)$$

$$i_e(2\omega_0) = \frac{-j\omega_0 C_{N1}}{2}{\alpha_1}^2{i_s}^2 \qquad (10)$$

$$i_e(3\omega_0) = -\frac{j\omega_0 C_{N2}}{3}{\alpha_1}^3{i_s}^3 - \frac{j2\omega_0 C_{N1}\alpha_1\alpha_2}{3}{i_s}^3 \qquad (11)$$

By substituting (9), (10), and (11) in (8):

$$\begin{gathered}\Delta V = R_p i_s - \left[\frac{1}{3}(\omega_0 C_{N1})\frac{{\alpha_1}^2 R_p}{Q}\right]{i_s}^2 \\ -j\left[\frac{2}{3}\left(\omega_0 C_{N1}\alpha_1\alpha_2 R_p\right) + \frac{1}{3}\left(\omega_0 C_{N2}{\alpha_1}^3 R_p\right)\right]{i_s}^3 \quad (12)\end{gathered}$$

By comparing (1) and (12), the coefficients are obtained as:

$$\alpha_1 = R_p \qquad (13)$$

$$\alpha_2 = \frac{-1}{3}\frac{{R_p}^3}{Q}(\omega_0 C_{N1}) \qquad (14)$$

$$\alpha_3 = j\left(\frac{2}{9}\frac{{R_p}^5}{Q}(\omega_0 C_{N1})^2 - \frac{1}{3}\left({R_p}^4\omega_0 C_{N2}\right)\right) \qquad (15)$$

As explained, by applying ohm's law ($v_s = R_p i_s$) for input voltage and current and assuming the following equation:

$$\Delta V = {\alpha_1}' v_s + {\alpha_2}' {v_s}^2 + {\alpha_3}' {v_s}^3 = \frac{\alpha_1}{R_p}v_s + \frac{\alpha_2}{{R_p}^2}{v_s}^2 + \frac{\alpha_3}{{R_p}^3}{v_s}^3 \quad (16)$$

1-dB compression point can then be derived and simplified using the followings:

$$\Delta V_{P,1dB}{}^2 = 0.145 \left|\frac{\alpha_1{}'}{\alpha_3{}'}\right| \qquad (17)$$

$$Q = \omega_0 R_p C_0 \qquad (18)$$

Where Q is the quality factor of the LC tank. After the simplifications, 1dB compression point is:

$$\Delta V_{P,1dB}{}^2 = \frac{0.435}{Q}\frac{C_0}{C_{N2}}\left|1 - \frac{2}{3}\frac{C_{N1}{}^2}{C_0 C_{N2}}\right|^{-1} \qquad (19)$$

Nonlinearity of Q-Enhanced LC tank

When the gm cell is also nonlinear, using Figure 2.6 and modifying (2) to the following:

$$i_e = i_s - \frac{j\omega_0 C_{N1}}{2}(\Delta V)^2 - \frac{j\omega_0 C_{N2}}{3}(\Delta V)^3 - g_{m3}(\Delta V)^3 \qquad (20)$$

And following the same procedure as what has also been derived for the linearity of the varactor, the following relationship can be achieved:

$$\Delta V_{P,1dB}{}^2 = \frac{0.435}{Q}\frac{C_0}{C_{N2}}\left[\left(1 - \frac{2}{3}\frac{C_{N1}{}^2}{C_0 C_{N2}}\right)^2 + \left(\frac{3g_{m3}}{\omega_0 C_{N2}}\right)^2\right]^{-0.5} \qquad (21)$$

APPENDIX B

Figure 2.8 (a) shows the main noise sources in the Q-enhanced LC filter. Output noise due to each noise source will be calculated and NF is obtained using total noise at the output and the total gain of the filter.

First, the total tank noise is:

$$\overline{V_{no}{}^2} = \frac{4KT}{R_p}\left(\frac{R_cR_{eq}}{R_c+R_{eq}}\right)^2 + \frac{4KT}{R_c}\left(\frac{R_cR_{eq}}{R_c+R_{eq}}\right)^2 + 4KT(\gamma(g_{m3}+g_{ds3}))\left(\frac{R_cR_{eq}}{R_c+R_{eq}}\right)^2 \quad (1)$$

In which $R_{eq} = R_p||R_{-gm}$ and $\gamma(g_{m3}+g_{ds3})$ is the triode nMOS which controls the total negative resistance. The second noise source is the current driver base resistance noise which is shown by r_{b2} in Figure 2.8 (b).

$$\overline{V_{no}{}^2} = \frac{4KTr_b}{\left(\frac{1}{g_{m2}}+R_E\right)^2}\left(\frac{R_cR_{eq}}{R_c+R_{eq}}\right)^2 \quad (2)$$

Third, voltage driver, Q_1 noise at the output is:

$$\overline{V_{no}{}^2} = \frac{4KT\left(1/2g_{m1}\right)}{R_c{}^2}\left(\frac{R_cR_{eq}}{R_c+R_{eq}}\right)^2 = \frac{4KT}{R_c}\left(\frac{R_cR_{eq}}{R_c+R_{eq}}\right)^2\left(\frac{1}{2R_cg_{m1}}\right) \quad (3)$$

In which $k = \frac{1}{2R_cg_{m1}}$. The second noise source is the current driver noise which is shown by Q_2 and R_E in Figure 2.8 (b).

$$\overline{V_{no}{}^2} = 4KT\cdot G_{m2}\left(\frac{R_cR_{eq}}{R_c+R_{eq}}\right)^2 \quad (4)$$

$4KT\cdot G_{m2}$ can be $2KT\cdot g_{m2}$ if the Q_2 noise is dominant or if $g_{m2}\cdot R_E \gg 1$, it would be $\frac{4KT}{R_E}$ which is the case for this design. Therefore, the total output noise is:

$$\overline{V_{no}{}^2} = 4KT\left(\frac{R_cR_{eq}}{R_c+R_{eq}}\right)^2\left(\frac{1}{R_p}+\frac{1+k}{R_c}+G_{m2} + \frac{r_b}{\left(1/g_{m2}+R_E\right)^2}+(\gamma(g_{m3}+g_{ds3}))\right) \quad (5)$$

To calculate Noise Figure (NF), the total gain of the filter is required:

$$A_v = (1+G_{m2}R_c)\,\frac{R_{eq}}{R_c+R_{eq}}\times\frac{1}{2} \quad (6)$$

½ is due to impedance matching.

Using (5) and (6) NF is:

$$NF = 1 + \frac{4KT \cdot 50}{4KT \cdot R_s} + \frac{\overline{V_{n,total}}^2 / A^2 v}{4KT \cdot R_s} \quad (7)$$

When R_s=50 Ω, it is:

$$NF = 1 + 1 + \frac{4KT\left(G_{m2} + \frac{r_b}{(1/g_{m2} + R_E)^2} + (\gamma(g_{m3} + g_{ds3}))\right)}{4KT \cdot R_s} + \frac{4 \times R_c^2}{(1+G_{m2}R_c)^2} \quad (8)$$

In which $\frac{1}{R_p}$and $\frac{1+k}{R_c}$ are negligible, and $G_{m2} \approx {}^1/_{R_E}$. To write the equation based on Gain and Q of the filter,

$$A_v = \frac{G_{m2}}{2} \cdot Q\sqrt{{}^L/_C} \quad (9)$$

$$\frac{1}{G_{m2}} = \frac{Q\sqrt{{}^L/_C}}{2A_v} \quad (10)$$

Subsitituting (9) and (10) intp (8) results in:

$$NF \approx 2 + (0.08) \cdot \left(\frac{Q\sqrt{{}^L/_C}}{2A_v} + r_b + \frac{\gamma(g_{m3} + g_{ds3})}{4A_v^2} \cdot Q^2 \cdot \frac{L}{C}\right) \quad (11)$$

References

[1] IEEE C802.16-10/0009, “Future wireless broadband networks: challenges and possibilities,” Jan. 2010.

[2] L. Mohammadi and K-J. Koh, "2-4 GHz Q-tunable LC bandpass filter with 172-dB.Hz peak dynamic range, resilient to +15-dBm out-of-band blocker," I*EEE Custom Integrated Circuit Conference. (CICC)*, Sep. 2015.

[3] L. Mohammadi and K-J. Koh, "Integrated C-band (4-8 GHz) frequency-tunable & bandwidth-tunable active band-stop filter in 0.13-µm SiGe BiCMOS," *IEEE International Microwave Symp. (IMS)*, May 2015.

[4] H. Xin, and W. B. Kuhn, "A 2.5-GHz low-power, high dynamic range, self-tuned Q-enhanced LC filter in SOI," *IEEE Journal of Solid-State Circuits*, vol.40, no.8, pp.1618-1628, Aug. 2005.

[5] F. Dulger, E. Sanchez-Sinencio, and J. Silva-Martinez, "A 1.3-V 5-mW fully integrated tunable bandpass filter at 2.1 GHz in 0.35-µm CMOS," *IEEE Journal of Solid-State Circuits*, vol.38, no.6, pp.918-928, June 2003.

[6] H. Darabi, "A Blocker Filtering Technique for SAW-Less Wireless Receivers," IEEE Journal of Solid-State Circuits, vol.42, no.12, pp.2766-2773, Dec. 2007.

[7] J.W.M. Rogers and C. Plett, "A 5-GHz radio front-end with automatically Q-tuned notch filter and VCO," *IEEE Journal of Solid-State Circuits*, vol.38, no.9, pp.1547-1554, Sept. 2003.

[8] D. Li, and Y. Tsividis, "Design techniques for automatically tuned integrated gigahertz-range active LC filters," *IEEE Journal of Solid-State Circuits*, vol.37, no.8, pp.967-977, Aug 2002.

[9] . A. N. Mohieldin, E. Sanchez-Sinencio, and J. Silva-Martinez, "A 2.7-V 1.8-GHz fourth-order tunable LC bandpass filter based on emulation of magnetically coupled resonators," *IEEE Journal of Solid-State Circuits*, vol.38, no.7, pp.1172-1181, July 2003.

[10] Z. Lin, P.-I. Mak, and R. P. Martins, "2.4 A 0.028mm^2 11mW single-mixing blocker-tolerant receiver with double-RF N-path filtering, S11 centering, +13dBm OB-IIP3 and 1.5-to-2.9dB NF," *IEEE International Solid-State Circuits Conference - (ISSCC)*, Feb,2015.

[11] R. Chen, and H. Hashemi, "Reconfigurable blocker-resilient receiver with concurrent dual-band carrier aggregation," *IEEE Custom Integrated Circuits Conference (CICC)*, vol., no., pp.1-4, 15-17 Sept. 2014.

[12] W.B. Kuhn; D. Nobbe; D. Kelly; A.W. Orsborn, "Dynamic range performance of on-chip RF bandpass filters," *IEEE Transactions on Circuits and Systems II*, vol.50, no.10, pp.685-694, Oct. 2003.

[13] Z. Gao, J. Ma, Y. Mingyan, and Y. Yizheng, "A Fully Integrated CMOS Active Bandpass Filter for Multiband RF Front-Ends," *IEEE Transactions on Circuits and Systems II*: Express Briefs, vol.55, no.8, pp.718-722, Aug. 2008.

[14] V. Stornelli; G. Leuzzi; L. Pantoli; S. Del Re, "High dynamic range bandpass filters design based on active inductor,*" IEEE European Microwave Integrated Circuits Conference (EuMIC)*, pp.168-171, 10-11 Oct. 2011.

[15] G. Leuzzi; V. Stornelli; S. Del Re, "A Tuneable Active Inductor With High Dynamic Range for Band-Pass Filter Applications," *IEEE Transactions on Circuits and Systems II*, vol.58, no.10, pp.647-651, Oct. 2011.

[16] W. B. Kuhn, F. W. Stephenson, and A. Elshabini-Riad, "A 200 MHz CMOS Q-enhanced LC bandpass filter," *IEEE Journal of Solid-State Circuits*, vol.31, no.8, pp.1112-1122, Aug 1996.

[17] W. B. Kuhn, N. K. Yanduru, and A. S. Wyszynski, "Q-enhanced LC bandpass filters for integrated wireless applications," *IEEE Trans. Microwave Theory Tech*., vol.46, no.12, pp.2577-2586, Dec 1998.

[18] T. Soorapanth, and S. S. Wong, "A 0-dB IL 2140±30 MHz bandpass filter utilizing Q-enhanced spiral inductors in standard CMOS," *IEEE Journal of Solid-State Circuits*, vol.37, no.5, pp.579-586, May 2002.

[19] Li. Shaorui, N. Stanic, K. Soumyanath, and Y. Tsividis, "An integrated 1.5 V 6 GHz Q-enhanced LC CMOS filter with automatic quality factor tuning using conductance reference," *IEEE Radio Frequency integrated Circuits (RFIC) Symposium*, vol., no., pp.621-624, 12-14 June 2005.

[20] J. Kulyk, and J. Haslett, "A monolithic CMOS 2368±30 MHz transformer based Q-enhanced series-C coupled resonator bandpass filter," *IEEE Journal of Solid-State Circuits,* vol.41, no.2, pp.362-374, Feb. 2006.

[21] B. Georgescu, I. G. Finvers, and F. Ghannouchi, "2 GHz Q-Enhanced Active Filter With Low Passband Distortion and High Dynamic Range," *IEEE Journal of Solid-State Circuits*, vol.41, no.9, pp.2029-2039, Sept. 2006.

[22] A. Ghaffari, E. A. M. Klumperink, and B. Nauta, "A differential 4-path highly linear widely tunable on-chip band-pass filter," *IEEE Radio Frequency Integrated Circuits Symposium (RFIC)*, vol., no., pp.299-302, 23-25 May 2010.

[23] A. Ghaffari, E. Klumperink, and B. Nauta, "8-Path tunable RF notch filters for blocker suppression," *IEEE International Solid-State Circuits Conference Digest of Technical Papers (ISSCC)*, vol., no., pp.76-78, 19-23 Feb. 2012.

[24] M. Darvishi, R. van der Zee, E. A. M. Klumperink, and B. Nauta, "Widely Tunable 4th Order Switched Gm-C Band-Pass Filter Based on N-Path Filters," *IEEE Journal of Solid-State Circuits*, vol.47, no.12, pp.3105-3119, Dec. 2012.

[25] M. Darvishi, R. van der Zee, and B. Nauta, "A 0.1-to-1.2GHz tunable 6th-order N-path channel-select filter with 0.6dB passband ripple and +7dBm blocker tolerance," *IEEE International Solid-State Circuits Conference Digest of Technical Papers (ISSCC),* vol., no., pp.172-173, 17-21 Feb. 2013.

[26] M. Darvishi, R. van der Zee, and B. Nauta, "Design of Active N-Path Filters," *IEEE Journal of Solid-State Circuits,* vol.48, no.12, pp.2962-2976, Dec. 2013.

[27] C. M. Thomas, and L. E. Larson, "A 65 nm CMOS tunable 0.1-to-1.6 GHz distributed transmission line N-path filter with +10 dBm blocker tolerance," *IEEE Custom Integrated Circuits Conference (CICC)*, vol., no., pp.1-4, 15-17 Sept. 2014.

[28] A. El Oualkadi, M. El Kaamouchi, J.-M. Paillot, D. Vanhoenacker-Janvier, and D. Flandre, "Fully Integrated High-Q Switched Capacitor Bandpass Filter with Center Frequency and Bandwidth Tuning," *IEEE Radio Frequency Integrated Circuits (RFIC) Symposium*, vol., no., pp.681-684, 3-5 June 2007.

[29] R. L. Bunch, and S. Raman, "Large-signal analysis of MOS varactors in CMOS -Gm LC VCOs," *IEEE Journal of Solid-State Circuits*, vol.38, no.8, pp.1325-1332, Aug. 2003.

[30] J. B. Ness, "A unified approach to the design, measurement, and tuning of coupled-resonator filters," *IEEE Trans. Microwave Theory Tech.*, vol.46, no.4, pp.343-351, Apr 1998.

[31] A. S. Sedra and F. O. Brackett, Filter Theory and Design: Active and Passive. Beaverton, OR: Matrix Publishers, Inc., 1978.

[32] T.-C. Lee, J. Lee, E.J. Naglich, and D. Peroulis, "Octave tunable lumped-element notch filter with resonator-Q-independent zero reflection coefficient," *IEEE MTT-S Int. Microwave Symp*., pp.1-6, June 2014.

[33] Y.-H. Cho and G. M. Rebeiz, "0.7-1.0-GHz Reconfigurable Bandpass-to-Bandstop Filter With Selectable 2- and 4-Pole Responses," *IEEE Trans. Microwave Theory Tech*., vol. 62, no. 11, pp.2626-2632, Nov. 2014.

[34] A. Vallese, A. Bevilacqua, C. Sandner, M. Tiebout, A. Gerosa, and A. Neviani, "Analysis and Design of an Integrated Notch Filter for the Rejection of Interference in UWB Systems," *IEEE Journal of Solid-State Circuits*, vol.44, no.2, pp.331-343, Feb. 2009.

[35] A. Bevilacqua, A. Vallese, C. Sandner, M. Tiebout, A. Gerosa, and A. Neviani, "A 0.13μm CMOS LNA with Integrated Balun and Notch Filter for 3-to-5GHz UWB Receivers," *IEEE International Solid-State Circuits Conference (ISSCC),* pp.420-612, Feb. 2007.

[36] A. Vallese, A. Bevilacqua, C. Sandner, M. Tiebout, A. Gerosa, and A. Neviani, "Analysis and Design of an Integrated Notch Filter for the Rejection of Interference in UWB Systems," *IEEE Journal of Solid-State Circuits*, vol.44, no.2, pp.331-343, Feb. 2009.

[37] Chuang Lu, M.K. Matters-Kammerer, R. Mahmoudi, and P.G.M. Baltus, "A 20 GHz 1.9 dB NF LNA with distributed notch filtering for VSAT applications," *2014 IEEE MTT-S Int. Microwave Symp*., pp.1-4, June 2014.

[38] C. Rauscher, "Varactor-tuned active notch filter with low passband noise and signal distortion," *IEEE Trans. Microwave Theory Tech*., vol. 49, no. 8, pp.1431-1437, Aug. 2001.

[39] M.H. Koroglu and P.E. Allen, "LC notch filter for image-reject applications using on-chip inductors," *Electronics Letters*, vol.37, no.5, pp.267-268, Mar. 2001.

[40] Sonnet, ver. 11.52, Sonnet Software Inc., Syracuse, NY, 1986-2005.

[41] P. Andreani and S. Mattisson, "On the Use of MOS Varactors in RF VCO's," *IEEE Journal of Solid-State Circuits*, vol.35, no.6, pp.905-910, June. 2000.

[42] T. D. Werth, C. Schmits, R. Wunderlich, and S. Heinen, "An Active Feedback Interference Cancellation Technique for Blocker Filtering in RF Receiver Front-Ends," in *IEEE Journal of Solid-State Circuits*, vol. 45, no. 5, pp. 989-997, May 2010.